



**An Alternative Pressure-Oscillation-Based Octane Rating Method, for Fuels below and beyond 100 RON, to Aid the Development of a Second-Generation Spark-Ignition Biofuel**

**Tom Robeyn**

Doctoral dissertation submitted to obtain the academic degree of  
Doctor of Electromechanical Engineering

**Supervisors**

Prof. Sebastian Verhelst, PhD - Tara Larsson, PhD  
Department of Electromechanical, Systems and Metal Engineering  
Faculty of Engineering and Architecture, Ghent University

July 2024





**An Alternative Pressure-Oscillation-Based Octane Rating Method, for  
Fuels below and beyond 100 RON, to Aid the Development of a Second-  
Generation Spark-Ignition Biofuel**

**Tom Robeyn**

Doctoral dissertation submitted to obtain the academic degree of  
Doctor of Electromechanical Engineering

**Supervisors**

Prof. Sebastian Verhelst, PhD - Tara Larsson, PhD

Department of Electromechanical, Systems and Metal Engineering  
Faculty of Engineering and Architecture, Ghent University

July 2024



ISBN 978-94-6355-858-7

NUR 961, 977

Wettelijk depot: D/2024/10.500/63

## **Members of the Examination Board**

### **Chair**

Prof. Sabine Wittevrongel, PhD, Ghent University

### **Other members entitled to vote**

Carlo Beatrice, PhD, Consiglio Nazionale delle Ricerche, Italy

Prof. Michel De Paepe, PhD, Ghent University

Prof. Marcus Lundgren, PhD, Lund University, Sweden

Honorary Prof. Roger Sierens, PhD, Ghent University

### **Supervisors**

Prof. Sebastian Verhelst, PhD, Ghent University

Tara Larsson, PhD, Ghent University



*You're never too old to set a new goal or dream a  
new dream.*

Clive Staples Lewis



# Acknowledgements

**I extend my heartfelt gratitude** to Prof. Dr. Sebastian Verhelst for graciously welcoming me into his team, more than two decades after my graduation from his faculty. It has been an honor and a pleasure to share four years under his guidance. Contrary to popular belief, an old fox can still learn new tricks, and it takes a masterful teacher to impart such knowledge. I can sincerely attest that Professor Verhelst is indeed a master teacher, coach, and manager.

I would like to express my sincere appreciation to Koen Chielens, the engine technician at STFES. Countless hours spent in the engine laboratory have shown me that there is no technical problem beyond Koen's expertise. Beyond his technical prowess, Koen has contributed to making my time at UGent filled with joy, humor, and friendship. He has become a cherished friend beyond the confines of our work.

My deepest thanks go to my fellow PhD student colleagues Yi-Hao, Ward, Victor, Quinten, Somayeh, and Jeroen. Despite the numerous challenges we encountered, it has always been a pleasure to spend time together, both inside and outside the office. With the wisdom of age, I can confidently say that an atmosphere as supportive and congenial as ours is rare and precious.

A special acknowledgment is reserved for Dr. Tara Larsson, my co-supervisor during my PhD journey. Thanks to her expertise and the countless hours we spent together, this book has become a reality.

Lastly, I would like to express my gratitude to my dear partner, Capucine, and my children, Victor and Lucie. Their unwavering presence, energy, and support have been a constant source of strength, reminding me of the importance of family throughout this journey.

*Ghent, april 2024*

*Tom Robeyn*



# Table of Contents

|   |             |
|---|-------------|
| <b>Acknowledgements</b>   | <b>i</b>    |
| <b>Table of Contents</b>  | <b>iii</b>  |
| <b>List of publications</b>   | <b>xi</b>   |
| <b>Nederlandse samenvatting</b>   | <b>xiii</b> |
| <b>English summary</b>  | <b>xvii</b> |
| <b>1 Biofuels for transportation</b>  | <b>1</b>    |
| 1.1 Introduction . . . . .  | 2           |
| 1.2 The role of transportation on GHG emissions . . . . .                                       | 4           |
| 1.3 Mitigating the impact of transport on global warming . . . . .                              | 7           |
| 1.3.1 European policies addressing climate change . . . . .                                     | 7           |
| 1.3.2 The role of sustainable fuels in road transport . . . . .                                 | 8           |
| 1.3.3 Biofuels and their current road transport use . . . . .                                   | 9           |
| 1.3.4 The biomass limit . . . . .   | 9           |
| 1.3.5 Matching sustainable fuels with advancements in<br>combustion engine technology . . . . . | 11          |
| 1.4 Research goals and objectives . . . . .   | 11          |
| 1.4.1 Structure of this book . . . . .  | 12          |
| <b>2 Fuel properties relevant to spark ignition engines</b>                                     | <b>15</b>   |
| 2.1 Operation of Spark Ignition Engines . . . . .   | 16          |
| 2.2 Typical gasoline composition . . . . .  | 18          |
| 2.3 Knock resistance . . . . .  | 20          |
| 2.3.1 Abnormal combustion - knock . . . . .   | 20          |
| 2.3.2 Knock resistance of spark ignition fuels . . . . .  | 22          |
| 2.3.3 RON and MON methodology . . . . .   | 23          |
| 2.3.4 Minimum RON and MON with European fuel standards . . . . .                                | 26          |
| 2.4 Volatility . . . . .  | 26          |
| 2.4.1 Reid Vapor Pressure (RVP) . . . . .   | 27          |
| 2.4.2 Reid Vapor Pressure methodology . . . . .   | 27          |
| 2.4.3 RVP limits with European fuel standards . . . . .   | 28          |
| 2.5 Other SI fuel properties . . . . .  | 29          |

---

|          |   |           |
|----------|---|-----------|
| 2.5.1    | Energy density . . . . .  | 29        |
| 2.5.2    | Chemical composition . . . . .  | 30        |
| 2.5.3    | Emissions . . . . .   | 30        |
| 2.6      | Chapter Conclusions . . . . .   | 31        |
| <b>3</b> | <b>Sustainable fuel development</b>   | <b>33</b> |
| 3.1      | Introduction . . . . .  | 34        |
| 3.2      | Lingocellulosic biofuel explained . . . . .                                     | 35        |
| 3.2.1    | The basic building blocks . . . . .   | 35        |
| 3.2.2    | A novel catalytic treatment . . . . .   | 38        |
| 3.3      | Fuel property investigation . . . . .   | 40        |
| 3.3.1    | Investigation of separate components with a fuel property database . . . . .    | 40        |
| 3.3.2    | Property calculations of blended components . . . . .                           | 43        |
| 3.3.3    | Improvements to the blend calculator . . . . .                                  | 46        |
| 3.3.4    | Initial EN228-compliance checks for RON . . . . .                               | 48        |
| 3.4      | Revised production process outcome . . . . .                                    | 49        |
| 3.4.1    | RON estimation of alternative blends . . . . .                                  | 49        |
| 3.4.2    | RVP estimation of the most promising fuel blend . . . . .                       | 51        |
| 3.5      | Chapter conclusions . . . . .   | 54        |
| <b>4</b> | <b>Development of a pressure-oscillation-based octane quantification method</b> | <b>55</b> |
| 4.1      | Insights into octane rating . . . . .   | 56        |
| 4.1.1    | Introduction . . . . .  | 56        |
| 4.1.2    | The history of RON and MON development . . . . .                                | 56        |
| 4.1.3    | Knock intensity measurement principles with RON and MON . . . . .               | 57        |
| 4.2      | The high-frequency character of knock . . . . .                                 | 60        |
| 4.3      | Oscillation-based knock intensity . . . . .                                     | 63        |
| 4.3.1    | Maximum amplitude of pressure oscillations - MAPO . . . . .                     | 63        |
| 4.3.2    | The stochastic nature of knock . . . . .  | 63        |
| 4.4      | Pressure-oscillation-based octane measurement . . . . .                         | 66        |
| 4.4.1    | Measurement setup . . . . .   | 66        |
| 4.4.2    | Engine parameters . . . . .   | 68        |
| 4.4.3    | A new knock intensity definition . . . . .                                      | 68        |
| 4.4.4    | Influence of knock intensity and sample size on reproducibility . . . . .       | 71        |
| 4.4.5    | The choice of MAMPO <sub>20</sub> test parameters . . . . .                     | 76        |
| 4.5      | System calibration with primary reference fuels . . . . .                       | 77        |
| 4.6      | Sensitivity analysis . . . . .  | 79        |
| 4.7      | MAMPO <sub>20</sub> verification measurements . . . . .                         | 81        |
| 4.8      | Chapter conclusion . . . . .  | 82        |
| <b>5</b> | <b>Pressure-oscillation-based octane quantification with toluene stan-</b>      |           |

|   |            |
|---|------------|
| <b>Standardization fuels</b>  | <b>83</b>  |
| 5.1 Octane Sensitivity and the need for toluene standardization fuels .                     | 84         |
| 5.2 MAMPO method with TSFs . . . . .  | 86         |
| 5.3 Accuracy verification through standard deviation measurements .                         | 88         |
| 5.4 Conclusions for RON up to 100 . . . . .   | 90         |
| 5.5 MAMPO <sub>20T</sub> method for fuels exceeding RON 100 . . . . .                       | 90         |
| 5.5.1 ASTM RON for fuels exceeding RON 100 . . . . .  | 90         |
| 5.5.2 Beyond RON 100 calibration . . . . .  | 91         |
| 5.5.3 Discussion . . . . .  | 93         |
| 5.5.4 MAMPO <sub>20T</sub> octane rating tolerance for fuels exceeding<br>RON 100 . . . . . | 95         |
| 5.6 Chapter conclusions . . . . .   | 96         |
| <b>6 Octane quantification with a knock sensor</b>  | <b>99</b>  |
| 6.1 The principle of knock detection . . . . .  | 100        |
| 6.2 Pressure oscillations versus knock sensor signal . . . . .                              | 101        |
| 6.3 Knock intensity definition based on knock sensor signal output . .                      | 103        |
| 6.4 Correlation between MAMPO <sub>20</sub> versus MAKO <sub>20</sub> knock intensity .     | 104        |
| 6.5 Constant MAMPO <sub>20</sub> curve of 40 kPa . . . . .                                  | 106        |
| 6.6 Obtaining MAKO <sub>20T</sub> RON of E5, E10 and PRF95 . . . . .                        | 108        |
| 6.7 Error analysis . . . . .  | 112        |
| 6.7.1 Confidence interval with E5 . . . . .   | 112        |
| 6.7.2 Confidence interval with TSF 107.6 . . . . .  | 114        |
| 6.7.3 Discussion of the results . . . . .   | 115        |
| 6.8 Chapter conclusions . . . . .   | 115        |
| <b>7 Conclusions and outlook</b>  | <b>119</b> |
| 7.1 Conclusions . . . . .   | 120        |
| 7.2 Outlook . . . . .   | 122        |
| <b>References</b>   | <b>123</b> |



---

## List of abbreviations

|                 |   |
|-----------------|---|
| 1G              | First-generation  |
| 2G              | Second-generation   |
| ATDC            | After Top Dead Center   |
| Ad-Libio        | Advanced Liquid Biofuels  |
| AE              | Absolute Error  |
| AFR             | Air-Fuel Ratio  |
| AKO             | Average Knock Oscillation                                       |
| $AKO_X$         | Average Knock Oscillation using X peak-to-peak amplitudes       |
| $AMPO_X$        | Average of Maximum Pressure Oscillations using X pressure peaks |
| ARV             | Accepted Reference Value  |
| ASTM            | American Society for Testing and Materials                      |
| BDC             | Bottom Dead Centre  |
| BEV             | Battery Electric Vehicle  |
| BTDC            | Before Top Dead Centre  |
| CA              | Crank Angle   |
| CA10            | Crank Angle at which 10% of heat is released                    |
| CA50            | Crank Angle at which 50% of heat is released                    |
| CA90            | Crank Angle at which 90% of heat is released                    |
| CFR             | Cooperative Fuel Research                                       |
| CH <sub>4</sub> | Methane   |
| CI              | Compression Ignition  |
| CI              | Confidence Interval   |
| CNG             | Compressed Natural Gas  |
| CO              | Carbon Monoxide   |
| CO <sub>2</sub> | Carbon Dioxide  |
| COP27           | Conference of the Parties of the UNFCCC                         |
| COV             | Coefficient of Variance   |
| CR              | Compression Ratio   |
| DAC             | Direct Air Capture  |
| DAQ             | Data acquisition  |
| DI              | Direct injection  |
| ECU             | Engine Control Unit   |
| EGR             | Exhaust Gas Recirculation                                       |
| EU              | European Union  |
| ETS             | European Trading System   |
| EV              | Electric Vehicle  |
| FAME            | Fatty Acid Methyl Esters  |
| GHG             | Greenhouse gas  |
| GMST            | Global Mean Surface Temperature                                 |
| HC              | Hydrocarbons  |

|                            |  |
|----------------------------|--|
| HCCI                       | Homogeneous Charge Compression Ignition  |
| HFO                        | Heavy Fuel Oil   |
| HoV                        | Heat of Vaporisation   |
| HVO                        | Hydrotreated Vegetable Oil   |
| H <sub>2</sub>             | Hydrogen   |
| IC                         | Intercooler  |
| ICE                        | Internal Combustion Engine   |
| ID                         | Ignition Delay   |
| IPCC                       | Intergovernmental Panel for Climate Change                                       |
| IT                         | Ignition Timing  |
| KI                         | Knock Intensity  |
| LBV                        | Laminar Burning Velocity   |
| LHV                        | Lower Heating Value  |
| LNG                        | Liquefied Natural Gas  |
| LPG                        | Liquefied Petroleum Gas  |
| MAKO                       | Mean Average Knock Oscillation   |
| <i>MAKO<sub>X</sub></i>    | Mean Average Knock Oscillation using X peak-to-peak amplitudes                   |
| MAMPO                      | Mean Average of Maximum Pressure Oscillations                                    |
| <i>MAMPO<sub>X</sub></i>   | Mean Average of Maximum Pressure Oscillations, using X pressure peaks            |
| <i>MAMPO<sub>20T</sub></i> | Mean Average of Maximum Pressure Oscillations with TSFs, using 20 pressure peaks |
| MAPO                       | Maximum Amplitude of Pressure Oscillations                                       |
| MAR                        | Maximum Amplitude Rating   |
| MGO                        | Marine Gas Oil   |
| MON                        | Motor Octane Number  |
| NG                         | Natural Gas  |
| N <sub>2</sub> O           | Nitrous Oxide  |
| NO                         | Nitric Oxide   |
| NO <sub>2</sub>            | Nitrogen Dioxide   |
| NO <sub>x</sub>            | Nitrogen Oxides  |
| NRMM                       | Non-Road Mobile Machinery  |
| NTC                        | Negative Temperature Coefficient   |
| OEM                        | Original Equipment Manufacturer  |
| OI                         | Octane Index   |
| ON                         | Octane Number  |
| OR                         | Octane Requirement   |
| PFI                        | Port Fuel Injection  |
| PRF                        | Primary Reference Fuel   |
| RCCI                       | Reactivity Controlled Compression Ignition                                       |
| RCF                        | Rapid Combustion Fraction  |
| RE                         | Relative Error   |
| RED II                     | Renewable Energy Directive   |
| RFNBO                      | Renewable Fuels of Non-Biological Origin   |

|        |   |
|--------|---|
| RON    | Research Octane Number                                |
| rpm    | Revolutions per minute                                |
| RVP    | Reid Vapor Pressure                                   |
| S      | Octane Sensitivity                                    |
| SAF    | Sustainable Aviation Fuel                             |
| SI     | Spark Ignition  |
| SOC    | Start of Combustion                                   |
| TDC    | Top Dead Centre                                       |
| TEL    | Tetraethyl Lead                                       |
| TSF    | Toluene Standardization Fuel                          |
| UHC    | Unburned Hydrocarbons                                 |
| UN     | United Nations  |
| UNFCCC | United Nations Framework Convention on Climate Change |
| VOC    | Volatile Organic Compounds                            |



# List of publications

## Publications in peer reviewed international journals

1. **Robeyn, T.**, Larsson, T., Verhelst, S.(2024). *Alternative RON estimation method by using pressure oscillation analysis, serving novel spark ignition fuel development*. Elsevier - FUEL. 364, Paper no. 131086. A1.
2. **Robeyn, T.**, Sileghem, V., Larsson, T., Verhelst, S. (2024). *A Pressure-Oscillation-Based RON Estimation Method for Spark Ignition Fuels beyond RON 100*. MDPI - Energies Volume 17 issue 6, Paper no. 1362. A1.

## Publications in proceedings of international conferences

1. **Robeyn, T.**, Verhelst, S., Vinke, I., Latine, H., Turner, J. (2022). *Investigation of Naphtha-Type Biofuel from a Novel Refinery Process*. SAE International, WCX SAE World Congress Experience, Paper no. 2022-01-0752. C1.
2. **Robeyn, T.**, Larsson, T., Demeersseman, J., Va Biesen, J., Verhelst, S. (2023). *Development of a Novel Drop-in Naphthenic Spark Ignition Bio-fuel by Means of a Fuel Blend Calculator and a Simplified Octane Number Verification Method*. SAE World Congress Experience, Paper no. 2023-01-0317. C1.
3. **Robeyn, T.**, Larsson, T., Verhelst, S. (2023). *Development of a second-generation naphthenic drop-in fuel for spark ignition applications*. 45th meeting of the Belgian and Italian sections of The Combustion Institute on Combustion for energy transition and sustainable mobility.

## Other publications not related to the PhD manuscript

1. Pu, Y., Larsson, T., **Robeyn, T.**, De Paepe, M., Verhelst, S. (2023). *Methanol Evaporation in an Engine Intake Runner under Various Conditions*. SAE 16th International Conference on Engines & Vehicles. Paper no. 2023-24-0018. C1.



# Nederlandse samenvatting

## –Summary in Dutch–

De relevantie van dit werk ligt binnen de bredere context van duurzame transportoplossingen. De ophoping van gasen zoals koolstofdioxide ( $CO_2$ ), methaan ( $CH_4$ ) en stikstofmonoxide ( $N_2O$ ) in de atmosfeer van de aarde leidt tot een opwarmend effect dat bekend staat als het broeikas-effect. Menselijke activiteiten, zoals het verbranden van fossiele brandstoffen, ontbossing en industriële processen, hebben de concentratie van deze gasen aanzienlijk verhoogd, waardoor het broeikas-effect wordt versterkt en de opwarming van de aarde in de hand wordt gewerkt. De belangrijkste bijdragers zijn de verbranding van fossiele brandstoffen voor energieproductie en transport, ontbossing, industriële processen zoals cementproductie, landbouw (met name vee- en pluimveeteelt) en afvalbeheer. Het aanpakken van deze bronnen is cruciaal voor het tegengaan van klimaatverandering. Momenteel draagt de transportsector bij aan ongeveer 16% van de wereldwijde uitstoot van broeikasgasen, een percentage dat voor Europa zelfs 25% ligt. Opmerkelijk is dat het merendeel van de uitstoot binnen deze sector afkomstig is van wegtransport. Met prognoses die wijzen op een piek van rond de 1,6 miljard auto's met verbrandingsmotoren tegen 2038 wereldwijd, is het noodzakelijk om de uitstoot van deze omvangrijke vloot aan te pakken. Hoewel elektrificatie vaak wordt geprezen als een oplossing, blijft een aanzienlijk aantal voertuigen met verbrandingsmotor nog vele jaren in gebruik. Voor deze voertuigen is een groene alternatieve brandstof noodzakelijk.

Als reactie op deze uitdaging introduceert het Ad-Libio-project, geleid door KU Leuven, een katalytisch proces dat in staat is om houtachtige biomassa om te zetten in een lichte naftische biobrandstof. Deze unieke brandstof, verschillend van zowel benzine als diesel, moest worden onderzocht op zijn potentieel als mengcomponent of als volledige vervanging van traditionele brandstoffen. Mocht deze biobrandstof zich bewijzen als een haalbare vervanging voor benzine of diesel zonder dat er wijzigingen nodig zijn aan bestaande motoren, dan zou het kunnen worden geclassificeerd als een 'drop-in' brandstof. Dergelijke brandstoffen kunnen, zoals hun naam laat vermoeden, zonder meer als vervangers van bestaande brandstoffen fungeren. Een dergelijke ontwikkeling zou een aanzienlijke stap voorwaarts betekenen op het gebied van duurzaamheid, aangezien de uitstoot

van deze biobrandstof bij verbranding niet zou bijdragen aan de toename van broeikasgassen in de atmosfeer, gezien de oorsprong van de biomassa als grondstof. Bovendien omzeilt het Ad-Libio-project de ethische dilemma's die gepaard gaan met biobrandstoffen van de eerste generatie door houtachtige biomassa te gebruiken als grondstof, waardoor concurrentie met eetbare gewassen wordt vermeden en er geen extra landbouwgrond nodig is.

Het Ad-Libio-project biedt daarmee een beloftevolle duurzame oplossing voor het verminderen van emissies uit de transportsector, en biedt een pad naar een vermindering van de afhankelijkheid van fossiele brandstoffen, terwijl de nadelen van traditionele biobrandstofproductiemethoden worden omzeild.

Dit doctoraatsonderzoek richtte zich primair op het onderzoeken en ontwikkelen van het Ad-Libio brandstofmengsel. In eerste instantie omvatte de studie het aanpassen van een bestaande rekenblad-gebaseerde brandstofmengcalculator en het integreren ervan met een uitgebreide database van brandstofcomponenten. De aangepaste calculator werd vervolgens gebruikt om de eigenschappen van Ad-Libio-brandstof te voorspellen en te vergelijken met Europese benzinebrandstofnormen. De analyse onthulde dat het originele Ad-Libio mengsel, zelfs als mengcomponent, niet geschikt was voor het vervangen van diesel of benzine. Het voornaamste probleem lag in het lage octaangetal (research octane number, RON) van de brandstof, dat aanzienlijk onder het minimumvereiste van 95 lag. Het octaangetal is een belangrijke brandstofeigenschap voor vonkonthekingsmotoren, aangezien dit weergeeft in welke mate de brandstof resistent is tegen klopp, een abnormale verbrandingsmodus die een negatieve invloed heeft op het rendement van de motor en zelfs kan leiden tot motorschade. Desalniettemin, door iteratieve aanpassingen aan het productieproces van Ad-Libio, mogelijk gemaakt door de brandstofcalculator, werden veelbelovende mengsels geïdentificeerd met voldoende hoge berekende RON-waarden. Het meestbelovende mengsel werd geselecteerd en onderworpen aan testen voor RON, Motor Octane Number (MON) en Reid Vapor Pressure (RVP). De resultaten toonden aan dat de blend voldeed aan de Europese normen voor benzinebrandstof, waardoor Ad-Libio werd bevestigd als een potentiële 'drop-in' brandstofkandidaat voor benzine.

Parallel met het aanpassen van de brandstofcalculator en het verfijnen van het productieproces van Ad-Libio, werd een alternatieve methode ontwikkeld om het Research Octane Number (RON) van verschillende Ad-Libio-brandstofkandidaten te beoordelen. Deze methode wijkt af van de conventionele RON- en MON-testprotocollen zoals beschreven in de ASTM-standaarden D2699 en D2700, respectievelijk. De reden voor deze afwijking was tweeledig: ten eerste voldeed de beschikbare testapparatuur bij UGent niet aan de ASTM-standaarden, en ten tweede worden deze standaarden al lange tijd bekritiseerd omdat ze niet langer de moderne motortechnologieën nauwkeurig vertegenwoordigen.

De ontwikkelde methode beruiste op het meten van de typische drukfluctuaties

die gepaard gaan met klop. Genaamd MAMPO (Mean Average of Maximum Pressure Oscillations), legde het algoritme een robuuste lineaire correlatie tussen de octaanwaarde van een brandstof en de intensiteit van het kloppen vast, waarmee een gekend probleem in de literatuur werd aangepakt. Onderzoek van de RON-resultaten benadrukte dat traditionele primaire referentiebrandstoffen niet adequaat de oscillatiegedragingen van moderne benzines vertegenwoordigen. Door ze te vervangen door tolueenstandaardbrandstoffen, vielen RON-schattingen voor E10- en E05-benzine binnen acceptabele onzekerheidsgrenzen.

Bovendien maakte het gebruik van tolueenstandaardbrandstoffen de evaluatie van brandstoffen boven RON 100 mogelijk, een prestatie die traditioneel moeilijk nauwkeurig te bereiken is met de ASTM-methode. De MAMPO-methode toonde een verbeterde capaciteit om brandstoffen te evalueren die RON 100 overschrijden, aanzienlijk verbeterend ten opzichte van de beperkingen van de traditionele ASTM-aanpak.

De MAMPO-methode sluit nauwer aan bij hoe klop wordt gedetecteerd door moderne klopsensoren in hedendaagse motoren. In de laatste fase van het onderzoek werd geprobeerd de kloof tussen octaan-kwantificatie en klopmeting te overbruggen. De MAMPO-methode werd uitgebreid om octaan-kwantificatie te omvatten met behulp van een klopsensor in plaats van een druksensor. Deze aanpassing onthulde een robuuste, zij het niet-lineaire correlatie tussen op accelerometer gebaseerde klopmintensiteit en octaangetal, waarbij volledig wordt afgestapt van drukmetingen in de verbrandingskamer en een nauwkeurige octaan-kwantificatiemethode wordt geboden die gebruik maakt van technologie vergelijkbaar met die welke wordt gebruikt in productiemotoren.

De verkregen resultaten markeren een belangrijke stap naar modernisering van octaan-kwantificatie, een proces dat bijna een eeuw oud is. Dit proof of concept baant de weg voor het gebruik van productiemotoren om zowel traditionele als nieuwe brandstoffen te evalueren onder echte verbrandingsomstandigheden, waardoor een nauwkeuriger beeld wordt verkregen van het gedrag van een brandstof in wegtoepassingen.



# English summary

The significance of this work lies within the broader context of sustainable transportation solutions. The greenhouse gas problem refers to the accumulation of gases, such as carbon dioxide ( $CO_2$ ), methane ( $CH_4$ ), and nitrous oxide ( $N_2O$ ), in the Earth's atmosphere. These gases create a blanket around the planet that traps heat, leading to a warming effect known as the greenhouse effect. While the greenhouse effect occurs naturally and is essential for sustaining life on Earth, human activities such as burning fossil fuels, deforestation, and industrial processes have significantly increased the concentration of these gases, amplifying the greenhouse effect and accelerating global warming. The main contributors are fossil fuel combustion for energy production and transportation, deforestation, industrial processes like cement production, agriculture (particularly livestock farming), and waste management. Addressing these sources is crucial for mitigating climate change. Currently, the transport sector contributes to approximately 16% of global greenhouse gas emissions. In Europe, the contribution of this sector even escalates to 25%. Notably, the majority of emissions within this sector stems from road transport. With projections indicating a peak of around 1.6 billion combustion-engine-powered cars worldwide by 2038, addressing the emissions from this extensive legacy fleet is imperative. While electrification is often touted as a solution, the reality is that a significant number of combustion engine vehicles will remain in operation for many years to come, given their considerable average lifespan. For these vehicles, a sustainable solution must be found.

In response to this challenge, the Ad-Libio project, led by KU Leuven, introduces a catalytic process capable of converting woody biomass into a light naphthenic biofuel. This unique fuel, distinct from both gasoline and diesel, required investigation for its potential as a blend component or as a complete substitute for traditional fuels. Should this biofuel prove to be a viable replacement for gasoline or diesel without necessitating any modifications to existing engines, it could be classified as a drop-in fuel. Drop-in fuels can, as the name suggests, fully replace existing fuels or can be used interchangeably. Such a development would represent a substantial stride towards sustainability, as emissions from the combustion of this biofuel would not contribute to the increase in greenhouse gas content in the atmosphere, given its biomass feedstock origin. Moreover, the Ad-Libio project

sidesteps the ethical dilemmas associated with first-generation biofuels by utilizing woody biomass as its feedstock, thus avoiding competition with edible crops or the need for additional agricultural land.

The Ad-Libio project therefore holds promise as a sustainable solution for mitigating emissions from the transport sector, offering a pathway towards reducing reliance on fossil fuels while circumventing the drawbacks of traditional biofuel production methods.

This doctoral research primarily focused on investigating and developing the Ad-Libio fuel blend. Initially, the study involved modifying an existing spreadsheet-based fuel blend calculator and integrating it with an extensive spark ignition fuel database. The modified calculator was then utilized to predict the properties of Ad-Libio fuel and compare them against European gasoline fuel standards. The analysis revealed that original Ad-Libio mix, even as a blend component, was not suitable for replacing diesel or gasoline. The primary concern stemmed from the fuel's Research Octane Number (RON), which fell significantly below the minimum requirement of 95. The octane number provides information on the fuel's ability to resist knock, an abnormal combustion mode that inversely affects engine efficiency and can even lead to engine damage. Nevertheless, through iterative adjustments to the Ad-Libio production process that were made possible with fuel calculator checks, promising blends with adequate calculated RON values were identified. The most promising blend was selected and subjected to testing for RON, Motor Octane Number (MON), and Reid Vapor Pressure (RVP). The results indicated that the blend met European gasoline fuel standards, thus establishing Ad-Libio as a potential drop-in fuel candidate for gasoline.

In tandem with modifying the fuel calculator and refining the Ad-Libio production process, an alternative method was developed to assess the Research Octane Number (RON) of various Ad-Libio fuel candidates. This method diverged from the conventional RON and MON testing protocols outlined in ASTM standards D2699 and D2700, respectively. The rationale behind this departure was twofold: firstly, the testing equipment available at UGent did not adhere to ASTM standards, and secondly, longstanding debates criticized these standards for no longer accurately reflecting modern engine conditions.

The devised method relied on measuring the typical pressure oscillations associated with engine knock. Named MAMPO (Mean Average of Maximum Pressure Oscillations), the algorithm established a robust linear correlation between a fuel's octane rating and knock intensity, addressing the historical lack of correlation found in existing literature. Examination of RON results highlighted that traditional primary reference fuels (PRFs) did not adequately represent the oscillation behavior of contemporary gasolines. By substituting them with toluene standardization fuels, which are known to better represent the behavior of gasoline fuels compared to their PRF counterparts, RON estimates for E10 and E05 gasoline fell within acceptable uncertainty limits.

Moreover, the utilization of toluene standardization fuels enabled the evaluation of fuels beyond RON 100, a feat traditionally challenging to achieve accurately using the ASTM method. The MAMPO method demonstrated an enhanced capability to evaluate fuels exceeding RON, significantly improving upon the limitations of the traditional ASTM approach.

Notably, the MAMPO method aligned more closely with how knock is detected by modern knock sensors in contemporary engines. In the final phase of the research, efforts were made to bridge the gap between octane quantification and knock measurement. The MAMPO method was expanded to incorporate knock quantification using a knock sensor instead of a pressure transducer. This adaptation revealed a robust albeit non-linear correlation between accelerometer-based knock intensity and octane number, effectively moving away from combustion pressure measurements and offering an accurate octane quantification method utilizing technology akin to that used in production engines.

The results obtained mark a significant step towards modernizing octane quantification, a process nearly a century old. This proof of concept paves the way for utilizing production engines to evaluate both traditional and novel fuels under real-life combustion conditions, providing a more precise depiction of a fuel's behavior in on-road applications.



# 1

## Biofuels for transportation

This chapter explores the topic of global warming and emphasizes the urgency of mitigation measures. Various human activities contribute to climate change, among which the transportation sector plays a significant role. Whether in aviation, shipping, or road transportation, the internal combustion engine (ICE) continues to be the primary source of propulsion. An analysis of the effects of various transportation sectors is presented, along with potential methods for their mitigation. As this study explores the potential of a new sustainable biofuel, it will primarily focus on solutions involving various types of biofuels and their benefits.

## 1.1 Introduction

During COP 21 in Paris, on December 12, 2015, the parties to the United Nations Framework Convention on Climate Change (UNFCCC) achieved a significant milestone by reaching an agreement to combat climate change and enhance efforts for a sustainable, low-carbon future. It rallied all nations to join forces in ambitious endeavours to address climate change and adapt to its impacts. Under this agreement, the 196 participating parties set 1.5 degrees Celsius as the aspirational limit for global mean surface temperature (GMST) rise, with 2 degrees Celsius as the maximum threshold [1]. According to certain accounts, the 1.5 degree limit has already been surpassed as of the present moment [2], stressing the urgency with which the problem should be addressed. Global warming contributes to climate change, exerting an undeniable impact on the entire planet [3]. Global warming is primarily caused by human activities that increase the concentration of greenhouse gases (GHGs) in the Earth's atmosphere. These activities include the burning of fossil fuels (such as coal, oil, and natural gas) for energy, deforestation, industrial processes, and agricultural practices. The main greenhouse gases responsible for global warming are carbon dioxide (CO<sub>2</sub>), methane (CH<sub>4</sub>), nitrous oxide (N<sub>2</sub>O), and fluorinated gases. These gases trap heat in the atmosphere, leading to a warming effect known as the greenhouse effect. Additionally, other factors such as changes in land use, urbanization, and certain industrial processes also contribute to global warming [4]. Anthropogenic carbon emissions, occurring on top of the world's active natural carbon cycle, were projected to reach a record 11.1±0.8 GtC (40.7±3.2 Gt CO<sub>2</sub>) in 2023 [5]. The overall perturbation of the global carbon cycle, caused by anthropogenic activities and averaged over the decade 2013-2022, is visualised in Figure 1.1

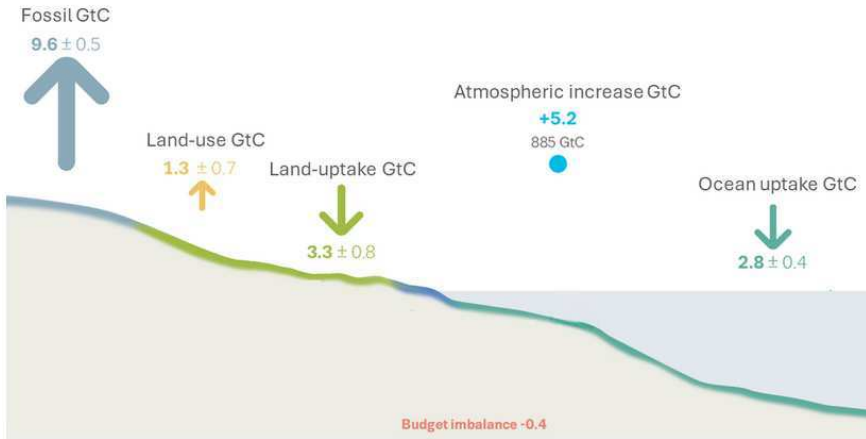


Figure 1.1: Averaged yearly CO<sub>2</sub> flux, in GtC, for the decade 2013-2022, modified from [5].

About 16% of the world’s GHG emissions can be associated with the transport sector. The major part of it is claimed to be caused by road transport [6], representing 12% of the world’s GHG emissions. Each sector’s contribution to greenhouse gas emissions can be observed in Fig 1.2, with the road transport sector’s contribution highlighted.

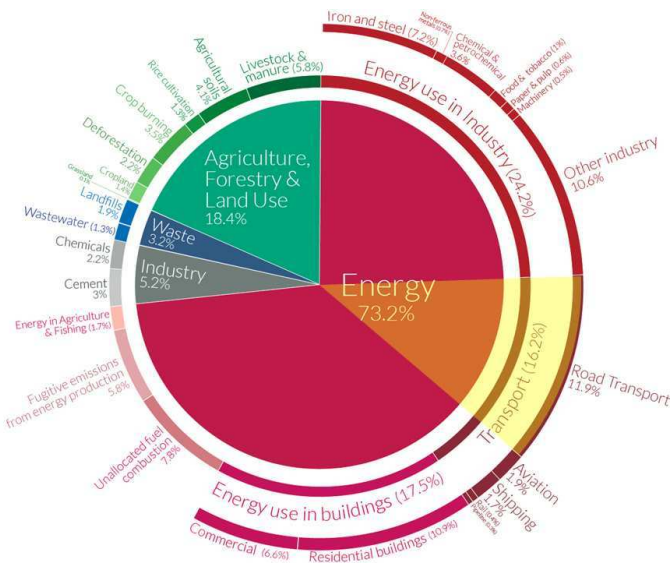


Figure 1.2: Global greenhouse gas emission by sector, shown for the year 2016.

In the European Union, the transport sector even accounts for a quarter of its GHG emissions, with three quarters stemming from road transport [7].

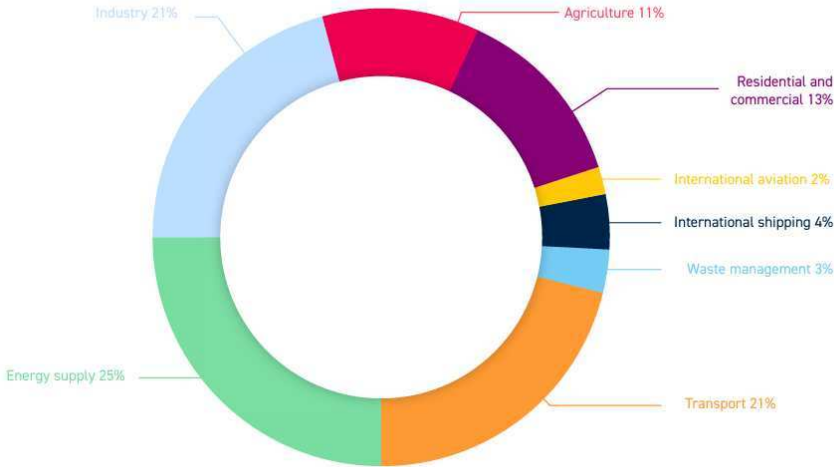


Figure 1.3: Greenhouse gas contributions per sector in Europe in 2020.

According to the FuelsEurope statistical report of 2023 [8], the road fuel demand in the 27 EU member states amounted to 185.000 million tonnes of diesel and 67.500 million tonnes of gasoline in 2022.

Achieving the Paris Agreement objective will necessitate global efforts from governments and corporations to invest in eco-friendly solutions and foster collaboration, aiming to significantly decrease greenhouse GHG emissions released into the atmosphere. The next paragraph offers an overview of potential mitigations across different transportation sectors, while also placing road transport's role within the wider context of transportation.

## 1.2 The role of transportation on GHG emissions

The transportation sector can be broadly categorized into three significant sectors: aviation, shipping, and road transport.

Each sector deals with its own particular problems with regards to propulsion.

The aviation industry operates at the forefront of technological advancement, necessitating lightweight materials and high energy density to efficiently propel aircraft. Turbofan jet engines, renowned for their power and reliability, are the predominant choice for both commercial and military aircraft propulsion. These engines heavily rely on Jet-A1 fuel, a type of kerosene, which serves as the industry standard. Despite persistent efforts to mitigate environmental impact, reducing emissions in aviation poses significant challenges. Unlike other transportation modes, electrification is not a straightforward solution due to aviation's unique requirements. Electrifying aircraft encounters substantial hurdles, primarily due to the energy density limitations of current battery technology [9]. The energy density of traditional fossil fuels significantly surpasses that of batteries, complicating the achievement of comparable performance with electric propulsion systems. Consequently, the aviation industry is exploring alternative strategies to diminish its carbon footprint. These strategies encompass enhancing engine efficiency, optimizing flight paths, and investing in sustainable aviation fuels (SAF) [10]. Despite technological advancements and sustainability initiatives, comprehensive mitigation in the aviation sector remains a complex and ongoing pursuit.

The shipping industry operates within a unique realm of challenges and demands. Characterized by typically large-bore engines, maritime vessels rely on robust propulsion systems to efficiently transport cargo and passengers over long distances. These engines predominantly utilize heavy fuel oils (HFO) or marine gas oil (MGO), leveraging the high energy density of fossil fuels to propel ships forward. However, the efficiency of these engines comes at a notable environmental cost. Alongside greenhouse gas emissions, the shipping sector contends with the emission of soot, also known as black carbon, during combustion. Soot particles have been identified as contributors to global warming, particularly when deposited on polar ice caps, where they accelerate ice melt and exacerbate the impacts of climate change [11]. Similar to aviation, the energy density requirements inherent in maritime operations present a barrier to the widespread adoption of electric propulsion systems. Consequently, the industry is actively exploring alternative solutions, including the development of low-emission fuels, enhancement of engine efficiencies, and implementation of emissions-reducing technologies. While strides are being made, addressing the environmental footprint of shipping remains a multifaceted and dynamic journey [12].

The road transport sector relies predominantly on internal combustion engines (ICEs) to propel vehicles of all shapes and sizes. Historically, the industry has

been fuelled by a steady diet of diesel or gasoline, powering cars, trucks, and buses across continents and through cityscapes. In recent years, there has been a notable shift towards improving the efficiency of internal combustion engines. This trend is characterized by strategies such as downsizing and boosting, which aim to extract more power from smaller engine configurations while consuming less fuel. These advancements not only enhance fuel economy but also contribute to the reduction of greenhouse gas emissions, aligning with global efforts to combat climate change [13]. While improvements to ICE technology continue to play a vital role in reducing emissions, electrification has emerged as a promising avenue for further mitigation within the road transport sector. Electric vehicles (EVs) could offer a clean alternative to traditional gasoline and diesel-powered vehicles, leveraging electricity as a power source [14]. As governments and industries worldwide commit to decarbonization targets, electrification is increasingly recognized as a crucial component of the solution to reduce GHG emissions in transportation, although this is certainly not a universal viewpoint [15, 16] and hybrid solutions could be a better answer in many cases [17].

A significant hurdle lies in addressing the world’s legacy fleet of internal combustion vehicles, which continue to populate roads and highways across the globe for many years to come. In fact, according to the US energy information administration [18], the peak of low-duty ICE-powered vehicles alone is expected to occur around 2038, at a number of about 1.6 billion units on the road.

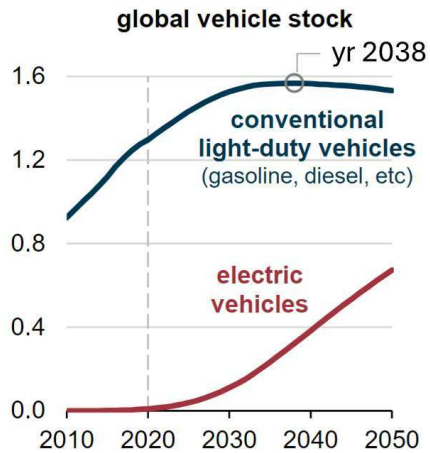


Figure 1.4: Global light duty vehicle stock projection, adapted from [18]

Finding effective solutions to manage and eventually replace these vehicles

represents a critical step towards achieving sustainable mobility for future generations.

## **1.3 Mitigating the impact of transport on global warming**

### **1.3.1 European policies addressing climate change**

Over the past years, Europe has formulated a series of legislations and directives aimed at fulfilling its commitment. All these regulations are interconnected or consolidated under the overarching framework of the European Green Deal [19], which is a comprehensive set of policy initiatives launched by the European Commission in December 2019. Its primary objective is to make the European Union (EU) climate-neutral by 2050 while also stimulating economic growth and creating jobs. The Green Deal encompasses various sectors, including energy, industry, agriculture, transportation, and biodiversity, with the aim of transforming the EU into a sustainable and competitive economy.

The Renewable Energy Directive (RED) [20] and its successor, the Renewable Energy Directive II (REDII) [21], are key components of the European Green Deal. These directives set binding renewable energy targets for EU member states and establish a framework for promoting the use of renewable energy sources in the EU. The RED and REDII directives mandate that EU countries must achieve a certain percentage of their energy consumption from renewable sources by specific deadlines.

The RED, adopted in 2009, aimed to increase the share of renewable energy in the EU's energy mix to 20% by 2020. It introduced measures to support the development and deployment of renewable energy technologies, such as wind, solar, biomass, and hydroelectric power.

Building on the RED's success, the REDII directive, adopted in 2018, established more ambitious renewable energy targets for the EU. It requires EU member states to achieve a renewable energy share of at least 32% of their final energy consumption by 2030. Additionally, REDII introduces sustainability criteria for biofuels and bioliquids to ensure that their production does not harm the environment or compete with food production.

Specifically for road transport applications, the EU aims to cut emissions from cars and vans by respectively 55 and 50% by 2030 compared to 2021. Furthermore, the

EU targets zero emissions from new cars and vans by 2035 [22]. The EU does not exclude the use of carbon-neutral fuels in internal combustion engines (ICEs) in the upcoming decades [23][24]. Despite the push towards electrification and other alternative propulsion technologies, sustainable fuels may still play a valuable role in reducing emissions and achieving sustainability goals in the transportation sector, which places this work within its context.

The share of renewables in powering transport in the EU reached 10.2% in 2020, meeting the 10% target set for that same year [7]. Part of this energy came from biofuels that are linked to another EU target, which is to reduce the greenhouse gas intensity of fuels sold for road transport. Biofuels can play a key role in decarbonising transport. However, it is important to ensure that rising demand for biofuels does not compromise the production of food and feed or convert land that is a carbon sink or stock — such as forests and wetlands — to a source of emissions.

### **1.3.2 The role of sustainable fuels in road transport**

Sustainable fuels for road applications encompass a range of alternatives aimed at reducing greenhouse gas emissions and dependence on fossil fuels in the transportation sector. These include hydrogen, e-fuels (synthetic fuels produced from renewable energy sources), synthetic fuels like HVO (Hydrotreated Vegetable Oil), biofuels like FAME (Fatty Acid Methyl Esters), and biofuels like ethanol.

Hydrogen is a versatile fuel that can be produced from renewable sources through electrolysis, offering near zero-emission transportation when used in fuel cell vehicles. E-fuels, also known as synthetic fuels, are produced by combining renewable energy sources such as wind or solar with  $CO_2$  to create synthetic hydrocarbons. They can be used in existing combustion engines without significant modifications, making them a promising option for decarbonizing existing fleets.

Synthetic fuels like HVO are produced through the hydroprocessing of vegetable oils or animal fats, resulting in a high-quality, low-emission diesel alternative. Biofuels like FAME, commonly derived from vegetable oils or animal fats, are renewable and can be blended, albeit in limited amounts, with conventional diesel fuel. Ethanol, typically produced from crops like corn or sugarcane, is commonly blended with gasoline to reduce emissions.

### 1.3.3 Biofuels and their current road transport use

First-generation (1G) biofuels are produced from food crops and compete with agricultural land, raising concerns about food security and land use change. Second-generation biofuels, derived from non-food biomass such as agricultural residues, offer improved sustainability but still face challenges related to land use and resource availability. Third-generation biofuels, often based on algae or waste materials, show promise for sustainability and reduced environmental impact.

Drop-in fuels are compatible with existing infrastructure and vehicles, requiring no modifications to the engine or fueling system. Examples include renewable diesel and gasoline alternatives like HVO and low level ethanol blends. Fuels that require engine modifications, such as flex-fuel technology or dedicated engines for specific biofuels like FAME, may offer greater efficiency and emissions reductions but require changes to vehicle technology.

In the European Union, regulations limit the amount of biofuels blended with fossil fuels to 7% in diesel [25] and 10% in gasoline [26]. These limits aim to maintain compatibility with existing engine technology while promoting the use of renewable fuels. However, this approach may limit the potential for significant reductions in carbon emissions from the legacy internal combustion engine-powered fleet.

### 1.3.4 The biomass limit

Concerns regarding biomass feedstock availability have often been cited as a rationale for limiting the role of biofuels in decarbonizing the transportation sector. Several critical inquiries arise concerning biomass availability: what quantity of sustainable biomass will be accessible in 2030 and 2050? Does the production of advanced and waste-based biofuels comply with the current sustainability criteria outlined in the Renewable Energy Directive (RED)? Will there be competition with alternative uses for biomass, and how can the impact on biodiversity be minimized? The study conducted by Imperial College London Consultants for Concawe, titled "Sustainable biomass availability in the EU towards 2050 (RED II Annex IX Part A/B)," [27] addresses these inquiries.

The findings of the report indicate that the potential total domestic availability of sustainable biomass in the EU by 2050, derived from agriculture, forestry, and biowastes feedstocks as listed in RED II Annex IX Part A/B, exceeds the requirements for supplying sustainable advanced biofuels to meet half of the renewable fuels demand. This assessment is based on the estimated demand

of 30-80 Mtoe/y of advanced biofuels and 30-80 Mtoe of e-fuels for aviation, maritime, and a portion of road transport, as outlined in the demand scenarios developed by Concawe in its study report titled "Transition towards Low Carbon Fuels by 2050: Scenario analysis for the European refining sector. The experts from Imperial College London Consultants conducted an assessment of sustainable feedstock availability across three distinct scenarios: low, medium, and high. In the high-case scenario, improvements in feedstock mobilization and management practices are assumed across all EU countries, alongside enhanced yields and efficiency in harvesting equipment. Their analysis revealed that even after allocating biomass feedstock to bio-based products and other non-transport energy sectors such as power, industry, and residential sectors in line with the European Commission's estimates, there remains a substantial portion of sustainable biomass available for transportation purposes by 2050. This availability is estimated to be adequate to facilitate the production of 70 to 175 Mtoe of advanced biofuels in the low and high scenarios, respectively, while considering limited biomass imports to the EU (10% of global availability).

The research highlights the existing potential, which could potentially be greater, given that the estimated biomass availability in this study is based on notably conservative assumptions, as outlined in the report. Furthermore, biodiversity has been meticulously taken into account in the study, guided by two fundamental principles: the preservation of land with notable biodiversity significance and land management practices aimed at minimizing impacts on biodiversity.

To delve deeper into the implications for biodiversity, Concawe commissioned a study from the Fraunhofer Gesellschaft Institute in collaboration with Imperial College London Consultants. Titled "Biodiversity Impact Assessment of future biomass provision for biofuel production – Phase 1" [28], the study aims to evaluate the environmental impacts on biodiversity resulting from biomass production for bioenergy purposes. A detailed analysis was conducted to ascertain whether the sustainable biomass availability harvested from unused, abandoned, and degraded lands (as estimated by Imperial College in the previous study) has any adverse effects on biodiversity. Germany and Bulgaria were chosen as case studies due to their high biomass availability, with *Miscanthus* serving as an energy crop example. The findings of the study indicate that there are particular instances where biodiversity would not be negatively impacted but might actually be enhanced when degraded lands in certain European regions are utilized for advanced biofuel production. However, assessing the state of land necessitates meticulous examination and evaluation of areas, along with precise definitions for terms such as unused, abandoned, or degraded land.

Despite positive reports from different sources, there seems to be no consensus in

literature regarding the sustainability of biofuels. The matter remains a subject for debate, since the sustainability evaluations of biofuels yield varying conclusions based on the methodology applied, the specific type of biofuel, the raw materials and technologies utilized, cultural considerations, and the conditions within each country, among other factors [29].

In any case, studies like the FVV Future Fuels Study IV [30] underscore the urgent need for a rapid ramp-down of fossil fuels in favor of alternative, renewable energy sources, highlighting the critical role of governments, industries, and individuals in driving this transition and calling for decisive action to address the pressing challenges of climate change and environmental sustainability.

### **1.3.5 Matching sustainable fuels with advancements in combustion engine technology**

Parallel to the development of sustainable fuels for combustion engines, it is crucial that advancements in these fuels are synchronized with the ongoing innovations in engine technology. This synchronization ensures that novel (bio)fuels are evaluated thoroughly with respect to their combustion properties, thereby optimizing performance in modern engines. Accurate octane measurement is therefore essential, as it influences engine efficiency, knocking resistance, and overall performance. In this work, current octane evaluation methods are reviewed, and an alternative method was devised to provide octane quantification that aligns more closely with current and future engine technology.

## **1.4 Research goals and objectives**

An initiative to address the global warming challenge is described in a study conducted by Op de Beeck et al. [31], a novel catalytic process was developed, enabling the direct conversion of cellulose (woody biomass) into liquid straight-chain alkanes. Subsequently, a project named Ad-Libio (Advanced Liquid Biofuels), supported by the Belgian Energy Transition Fund, aimed to evaluate whether the resulting product could serve as a second-generation biofuel suitable for road-use combustion engines. This PhD was part of this project, investigating different properties of the Ad-Libio fuel.

The first goal of this PhD project sought to determine the viability of using the fuel in spark ignition or compression ignition engines, either as a blend component or, ideally, as a drop-in replacement for diesel or gasoline.

The second goal was to provide engine performance-related feedback so that the Ad-Libio production process could be adapted to achieve the ideal fuel composition. This adaptation would ultimately result in a sustainable drop-in fuel blend suitable for gasoline or diesel engines.

In a third and more extensive phase, an alternative octane measurement method needed to be devised. This innovative approach, based on pressure oscillations during knock, would be more aligned with how knock is detected in modern engines and should provide equal or better accuracy than traditional methods. It should also be applicable to fuels exceeding RON 100, thereby addressing a historical lack of accuracy in existing octane quantification methods.

In summary, the research conducted in this PhD work aimed to optimize the production and assessment of woody biomass-based spark ignition biofuels, with a particular focus on their compatibility with existing combustion engine technology and their potential to mitigate the carbon footprint of the transportation sector. In the process, a new octane quantification method has been developed that potentially provides a pathway towards octane assessment of novel sustainable fuels, that is more in line with the advancements in combustion engine technology.

### **1.4.1 Structure of this book**

The structure of the book is organized in seven chapters.

Chapter 2 furnishes the reader with essential background information on the operation of a spark ignition engine. It begins by elucidating the phenomenon of abnormal combustion known as knock. Furthermore, it delves into the properties of spark ignition fuels and their significance in the context of spark ignition engine operation. Finally, it offers a detailed exploration of the fundamental structure of gasoline to enhance understanding of the fuel development process discussed in the subsequent chapter.

Chapter 3 outlines the methodologies employed to aid in the development of Ad-Libio, a pioneering sustainable spark ignition fuel. The refinement of a spreadsheet-based fuel property calculator enabled insights into the fuel's essential properties. These insights facilitated necessary revisions to the production process, ultimately yielding a list of promising fuel blends. From this list, the most favorable spark ignition fuel candidate was selected and the first two research goals were met.

Chapter 4 outlines the experimental verification of various Ad-Libio fuel blends, generated by the fuel calculator, in terms of their resistance to knock. To

achieve this, an alternative octane evaluation method was developed based on the equipment available in the engine laboratory at UGent. This method utilizes the assessment of pressure oscillations during knock, addressing the historical challenge of correlating octane number with oscillation-based knock intensity. By providing insights into the oscillation behavior of fuels during knock, this alternative evaluation method offers valuable contributions to the study of knock-resistive properties.

Chapter 5 capitalizes on the insights gained in Chapter 4 and elucidates the significant enhancements achieved through the utilization of toluene standardization fuels in place of traditional primary reference fuels. This substitution resulted in a drastic improvement in octane estimation accuracy, with results showing no significant deviation from those obtained using the traditional ASTM RON methodology. Moreover, the use of toluene standardization fuels enables the estimation of RON values exceeding 100, while maintaining the same experimental uncertainty observed with fuels below RON 100, which is difficult or unattainable with the conventional RON method. With these results, the third research goal was met, although a promising variation of the method was developed in the next chapter.

Chapter 6 delineates the efforts made to reconcile the disparities between octane measurement and knock detection using a knock sensor. In pursuit of this objective, an octane quantification method was developed, leveraging the groundwork laid in Chapters 4 and 5. The obtained results laid the groundwork for the development of an alternative octane estimation method that circumvents the need for pressure measurement equipment, which is typically absent in production engines. This approach aligns more closely with the manner in which knock is detected in a production engine, marking the initial strides toward providing an alternative and practical future-proof octane estimation solution.

The final chapter, Chapter 7, synthesizes the findings and insights gleaned from the doctoral research conducted. It elucidates the contributions made to the existing state-of-the-art and identifies prospective directions for future research, leveraging the discoveries and advancements made in this study.



# 2

## Fuel properties relevant to spark ignition engines

This chapter provides an overview of the working principle of spark ignition engines, followed by an exploration of key properties associated with SI engine fuel, namely octane rating, volatility, and energy density. The aim is to offer definitions and fundamental knowledge of spark ignition principles, establishing the foundation for the research conducted in this work.

## 2.1 Operation of Spark Ignition Engines

Spark ignition engines, commonly referred to as gasoline engines, play a vital role in modern transportation and power generation. Understanding their operation is essential for the subsequent discussions in this work. This chapter aims to provide a comprehensive overview of the working principles behind spark ignition engines, emphasizing key components, processes, and factors influencing their performance.

These engines comprise several essential components that collaborate to facilitate combustion and power generation. The primary components include the cylinder, piston, spark plug, intake and exhaust valves, and crankshaft.

The operation of a spark ignition engine follows a four-stroke cycle: intake, compression, power, and exhaust, as illustrated in Figure 2.1.

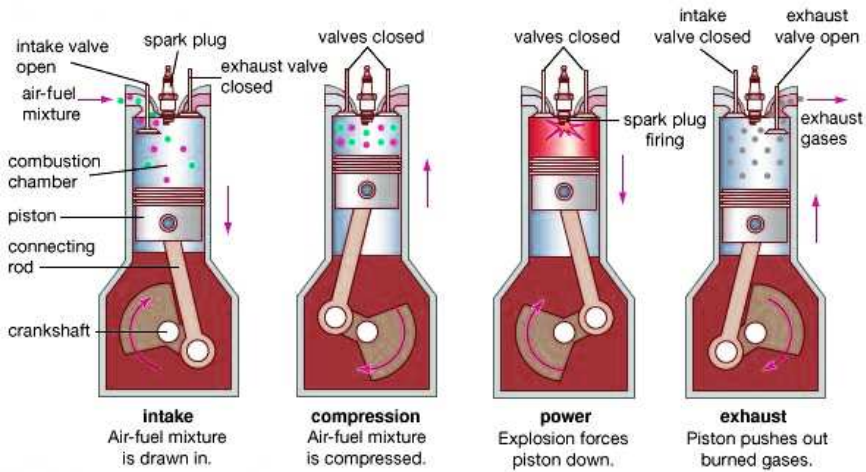


Figure 2.1: Working principle of a four-stroke spark ignition engine

During the intake stroke, the intake valve opens and the piston moves downward from top dead centre (TDC), creating a vacuum in the cylinder. This vacuum draws in a mixture of air and fuel from the intake manifold.

In the compression stroke, the intake valve closes, and the piston moves upward from bottom dead centre (BDC), compressing the fuel-air mixture. This compression increases the mixture's temperature and pressure, preparing it for combustion.

The power stroke is initiated by the spark plug, which generates a spark to ignite the compressed fuel-air mixture. The ignition of the mixture causes rapid expansion, generating high pressure that pushes the piston downward with significant force. This downward motion of the piston is converted into rotational motion by the crankshaft.

Finally, in the exhaust stroke, the exhaust valve opens, and the piston moves upward again, pushing the exhaust gases out of the cylinder and into the exhaust system.

The timing of the ignition spark, known as ignition timing, is precisely controlled by the engine's control system to optimize performance and efficiency. Similarly, the amount of fuel delivered into the cylinder, known as fuel delivery, is regulated by the fuel injection system based on factors such as engine load, speed, and intake air temperature.

The pressure variation inside the cylinder is illustrated in Figure 2.2, highlighting the distinction between a motoring cycle and a fired cycle. In a 'motoring' cycle, no fuel is injected into the cylinder, whereas in a fired cycle, fuel is injected into the intake manifold. In the depicted scenario, the ignition spark occurs at 20° before top dead centre (BTDC), and the segment of the trace from point A to point B is known as the ignition delay, which is the time needed for the fuel to ignite. During this phase, there is minimal disparity in cylinder pressure between a fired and motoring cycle. Subsequently, from point B to point C, combustion of gasoline initiates, forming a turbulent flame front that rapidly traverses the cylinder, leading to a significant pressure increase compared to a motoring cycle.

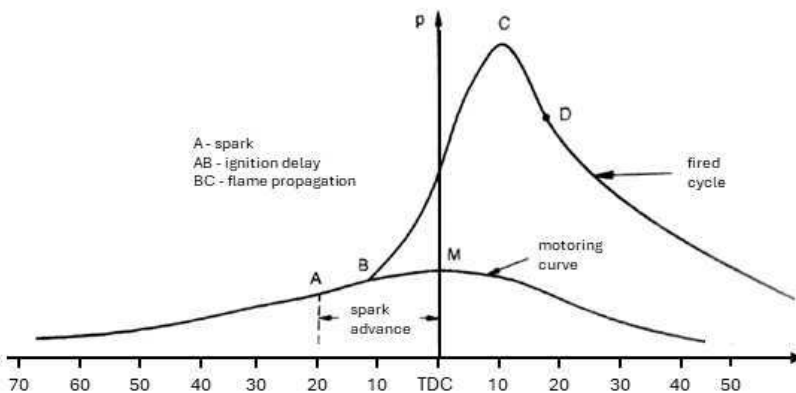


Figure 2.2: Pressure trace of a motored versus a fired combustion cycle , modified from [32].

Several engine-related factors influence the performance of spark ignition engines, such as compression ratio and valve timing. Equally important is the fuel itself, some of the most essential properties for a fuel to be suitable for use in spark ignition engines are [33]:

- **Octane Rating:** This indicates the fuel's resistance to knocking or detonation. Higher octane fuels are needed for high-performance engines to prevent premature ignition, which can damage the engine. This is explained in detail later in this work.
- **Volatility:** The ability of the fuel to vaporize at low temperatures is essential for smooth starting and operation, particularly in cold weather conditions.
- **Chemical composition:** The composition of hydrocarbons and additives in the fuel influences combustion characteristics, emissions, and engine performance.
- **Energy density:** Fuels with higher energy density can provide more power per unit of volume or weight, impacting the vehicle's autonomy.
- **Stability:** Fuels should remain stable during storage to prevent degradation and the formation of deposits or gums that could harm the engine.
- **Cleanliness:** The purity of the fuel, including its sulfur content and the presence of contaminants, affects emissions and engine longevity.
- **Corrosiveness:** Fuels should not contain corrosive substances that can damage fuel system components.
- **Compatibility with engine components:** Some fuels may contain additives or compounds that can harm certain engine components if used long-term.

## 2.2 Typical gasoline composition

The most used spark ignition engine fuel is gasoline, a complex mixture of hydrocarbons, which are molecules composed primarily of carbon (C) and hydrogen (H) atoms. The number of carbon atoms in gasoline molecules can vary widely depending on the specific hydrocarbons present in the mixture [34]. Typically, gasoline contains hydrocarbons with carbon chain lengths ranging from about 5 to 12 carbon atoms per molecule. This includes straight-chain alkanes (paraffins), branched-chain alkanes, cycloalkanes (naphthenes), and aromatic hydrocarbons (such as benzene, toluene, and xylene).

Paraffins, or alkanes, represent hydrocarbons characterized by a straight-chain molecular structure composed solely of saturated bonds, rendering them highly stable compounds. Generally, paraffins exhibit inferior antiknock qualities, particularly as the carbon chain length increases. Moreover, due to their numerous hydrogen atoms, they possess the highest heating value [35].

Olefins, or alkenes, share a straight-chain structure akin to paraffins but feature one or more double unsaturated bonds. A single double bond has minimal antiknock impact, whereas two or three double bonds typically result in significantly reduced knocking tendencies [35]. However, these double bonds render the carbon structure unstable, leading to oxidation during storage and the formation of gummy deposits, which fuel specifications generally limit. Olefins with multiple carbon double bonds are undesirable due to storage issues, thus necessitating refinement to ensure gasoline predominantly comprises mono olefins [36, 37].

Naphthenes share the same chemical formula as olefins but possess a ring structure, often referred to as cyclo-paraffins or cycloalkanes. Constituted of saturated bonds, they tend to exhibit stability. Cyclopentane, a compound in the naphthene series ( $C_nH_{2n}$ ), is an example [37].

Conversely, aromatic compounds also feature a ring structure but contain unsaturated double bonds. The presence of unsaturated bonds confers greater stability compared to other unsaturated compounds like naphthenes. Benzene ( $C_6H_6$ ) represents the simplest structure, with various aromatic compounds forming when one or more hydrogen atoms of benzene molecules are replaced with an organic radical such as paraffins, naphthenes, and olefins [37]. Introducing two or three double bonds in both naphthenes and aromatics reduces knocking tendencies. Additionally, long side chains attached to the benzene structure have a similar effect [34].

The different Ad-Libio fuel compositions, which will be discussed in the next chapter, deviate significantly from typical gasoline. To explore the fuel properties and draw comparisons to gasoline, it is essential to understand the most important fundamental SI properties and their testing methods. This will be addressed in the following sections.

## 2.3 Knock resistance

### 2.3.1 Abnormal combustion - knock

The engine can suffer adverse effects if the fuel within the mixture ignites spontaneously before the spark initiates or before the flame front reaches the gases ahead of it. This leads to uncontrolled combustion processes, resulting in significantly increased pressure and pressure fluctuations inside the cylinder. This phenomenon, termed knock in one scenario and pre-ignition in another, is illustrated in Figure 2.3. It occurs when the pressure and temperature surpass the threshold for the fuel to resist auto-ignition in the end-gas zone.

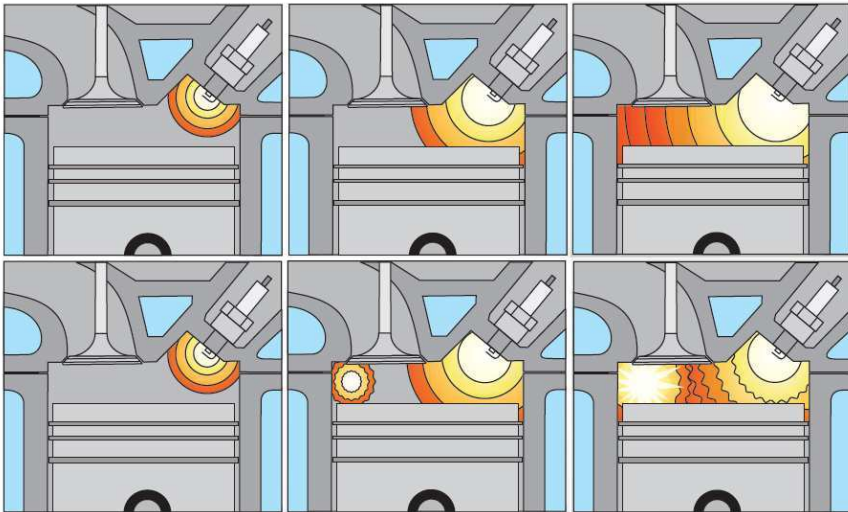


Figure 2.3: Normal SI combustion (top) versus knocking combustion (bottom).

Engine knock poses a complex challenge, originating from the spontaneous ignition of pockets of end-gas within the combustion chamber. This triggers a cascade of harmful effects that compromise both engine performance and durability. Engine knock initially disturbs the smooth functioning of the powertrain, causing irregularities in the combustion process. These disruptions manifest audibly as high-frequency pressure waves, commonly recognized as a rattling or knocking noise. Primarily, engine knock limits thermal efficiency by disturbing the ideal progression of combustion events. Premature ignition of unburned fuel-air mixtures leads to the generation of excessive heat and pressure gradients within the cylinder, causing significant pressure spikes as illustrated in

Figure 2.4. Consequently, the engine fails to extract optimal energy from the fuel, resulting in diminished power output and compromised fuel economy [33].

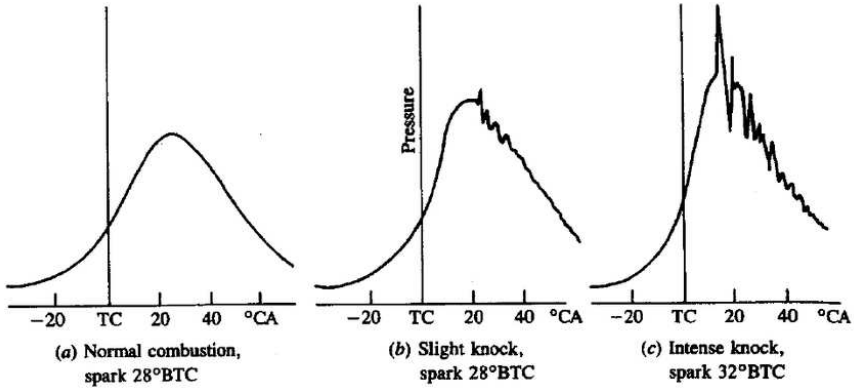


Figure 2.4: Cylinder pressure traces for normal combustion and knocking combustion cycles.

The abrupt pressure surges exert undue stress on engine components, particularly pistons, connecting rods, bearings, and valves. This persistent mechanical strain accelerates wear and fatigue, hastening the onset of component failure and necessitating premature maintenance or replacement. In its most severe manifestations, engine knock can lead to irreversible damage, causing engine failure. Prolonged exposure to abnormal combustion conditions exacerbates thermal stresses, leading to piston scuffing, ring land erosion, and valve burning. These structural impairments compromise engine integrity, mandating extensive repairs or complete overhauls [38]. The illustration in Figure 2.5 shows an extreme example of engine damage caused by engine knock.



*Figure 2.5: A damaged piston, the result of extensive exposure to engine knock.*

Consequently, mitigating engine knock is imperative not only to preserve driving comfort but also to uphold engine performance and durability. Given that knock significantly constrains efficiency in spark ignition engines, it emphasizes the critical need for understanding and effectively managing this phenomenon. The following section will thus explore the definition of a fuel's resistance to knock.

### **2.3.2 Knock resistance of spark ignition fuels**

Investigation of the knock phenomenon dates back to the early 1900s. Around 1930, the Cooperative Fuel Research committee introduced the Cooperative Fuel Research (CFR) engine and the octane scale. This scale assesses the autoignition characteristics of a sample fuel by comparing it to a reference blend with a specified octane number. The reference blends consist of binary combinations of 2,2,4-trimethylpentane (also known as iso-octane) and n-heptane, referred to as primary reference fuels (PRFs). According to the definition, the octane number (ON) of a PRF blend is equivalent to the volumetric ratio of iso-octane in a mixture of iso-octane and n-heptane, as expressed in Equation 2.1. For instance, a blend comprising 95% iso-octane and 5% n-heptane would have an ON of 95.

$$ON = \frac{(\text{volume of iso-octane})}{(\text{volume of iso-octane} + \text{volume of n-heptane})} \cdot 100 \quad (2.1)$$

Two traditional test methods were developed to assign a fuel's octane rating. The initial ON development involved the research octane number (RON) test method

first, with the motor octane number (MON) test being introduced later. The MON method was developed in response to on-road testing that revealed the inadequacy of RON alone, since some fuels that met RON specifications did not seem to meet performance expectations on the road [39]. The main differences between RON and MON conditions are listed in Table 2.1.

*Table 2.1: RON and MON test conditions*

| <b>Parameter</b>          | <b>RON test</b>              | <b>MON test</b> |
|---------------------------|------------------------------|-----------------|
| Engine Speed              | 600 rpm                      | 900 rpm         |
| Spark Timing              | 13° BTDC                     | 14° - 26° BTDC  |
| Inlet air temperature     | 20°-52° C based on barometer | 38 °C           |
| Inlet mixture temperature | Not controlled               | 149 °C          |

### 2.3.3 RON and MON methodology

Determining the Research Octane Number (RON) of a fuel involves following testing procedures outlined in the ASTM-D2699 standard [40]. The setup utilizes a Cooperative Fuel Research (CFR) engine with adjustable compression ratios, depicted in Figure 2.6.

A magnetorestrictive pressure pickup system, called the D1 model is linked via a "detonation meter" circuit board to a "knockmeter" display as illustrated in Figure 2.7 and provides data on knock intensity. Initially, a sample fuel is introduced into the system, and the air-to-fuel ratio is fine-tuned until the knock meter indicates maximum deflection, indicating peak knock intensity (KI). Subsequently, the compression ratio is adjusted to attain a specific knock intensity level, typically when the knock meter needle is centered. This compression ratio remains constant throughout the test. Two PRF blends are chosen such that, at their air-fuel ratio for maximum KI, one blend exhibits stronger knocking (higher KI) while the other shows weaker knocking (lower KI) compared to the sample fuel. The RON of the sample fuel is then determined via interpolation, based on the differences in KI readings. This method is known as "bracketing". The same methodology is applied when defining the Motor Octane Number (MON) albeit with different parameters as indicated in Table 2.1 and outlined in the ASTM-D2700 standard [41].

The knock resistance of a fuel, when measured with the RON method, is influenced by various factors [33, 34]:



*Figure 2.6: The CFR engine.*

- **Chemical composition:** The molecular structure of the hydrocarbons in the fuel affects its knock resistance. Fuels with higher concentrations of branched-chain hydrocarbons or aromatic compounds tend to have higher knock resistance.
- **Heat of vaporization:** The heat of vaporization, or the energy required to convert the liquid fuel into vapor, influences the temperature and pressure inside the combustion chamber. Fuels with higher heat of vaporization tend to resist autoignition and knock better, due to their cooling effect on the intake charge.
- **Air-Fuel Ratio:** The ratio of air to fuel in the combustion mixture affects knock resistance. Leaner mixtures (higher air-to-fuel ratio) typically have higher knock resistance due to lower combustion temperatures.
- **Intake air temperature and pressure:** conditions of higher pressure and temperature tend to decrease the fuel's knock resistance.
- **Additives:** Some fuel additives, such as octane boosters or anti-knock agents



Figure 2.7: The D1 pressure pickup (a) - detonation meter (b) - knockmeter (c).

like tetraethyl lead (TEL), can enhance knock resistance by altering the chemical properties of the fuel or modifying the combustion process.

Other factors that have an influence on knock resistance cannot be captured with the RON test, namely:

- **Engine Design:** Various factors within engine design, including compression ratio, and combustion chamber geometry play crucial roles in determining knock resistance. Higher compression ratios often necessitate the use of fuels with higher octane ratings to mitigate knock. However, as the CFR engine utilized in RON testing typically maintains fixed spark timing and engine geometry, apart from its adjustable compression ratio, the impacts of these factors cannot be assessed within the confines of the RON test.
- **Operating Conditions:** Factors like engine load, speed, and temperature influence knock resistance. Under high load and/or high-speed conditions, the likelihood of knock increases, requiring fuels with higher octane ratings.

The MON test provides additional information on a fuel's resistance to knocking under different driving conditions by simulating higher-speed and heavier-load engine operation. The impact of charge cooling represents a notable distinction between RON and MON, a topic extensively explored in literature [42, 43]. RON measurements prescribe a fixed intake air temperature, whereas MON measurements are performed with a fixed temperature of the air-fuel *mixture*, so after the fuel is injected in the intake manifold. Fuels with high latent heat of vaporization, such as ethanol, exhibit heightened octane sensitivity due to the significant cooling effect on the intake air during fuel induction in RON tests. Consequently, this results in a lower temperature of the air-fuel mixture compared to a reference fuel with lower latent heat of vaporization, such as a PRF mixture, leading to a higher RON [42, 43].

The difference between RON and MON is known as the octane sensitivity ( $S$ ), expressed in Equation 2.2.

$$S = RON - MON \quad (2.2)$$

Octane sensitivity can be understood as a measure of the difference in autoignition chemistry of a sample fuel when operating conditions change. A high octane sensitivity suggests that the fuel's performance may vary significantly under different operating conditions. Since the advancement in automotive technology has led to engine designs and operational parameters deviating significantly from the standard conditions of RON and MON tests [44], their relevance to modern engine fuels is being scrutinized [45]. However, RON and MON are still well established and commonly employed metrics today and are considered as one of the key quality indicators of a gasoline fuel.

### **2.3.4 Minimum RON and MON with European fuel standards**

The EN228 standard [26] is a European norm that outlines the requirements and specifications for unleaded gasoline (petrol) used as a motor fuel for vehicles. It covers various aspects of gasoline quality and composition to ensure that it meets the necessary standards for performance, emissions, and engine compatibility. EN228 specifies the allowable components and their concentrations in gasoline. This includes requirements for the presence of specific hydrocarbons, as well as limits on undesirable compounds such as sulfur, benzene, olefins, and aromatics. These limits are set to ensure that the gasoline meets environmental and health standards and performs optimally in vehicle engines. The standard includes requirements for the octane rating of gasoline, and sets forward a minimum RON of 95 and minimum MON of 85. Alongside minimum RON and MON requirements, the EN228 standard also establishes minimum requirements for other fuel aspects, which will be discussed in the following paragraphs.

## **2.4 Volatility**

Volatility plays a crucial role in the performance, efficiency, and safety of automotive engines. Volatility refers to the tendency of gasoline to vaporize, and it directly impacts engine starting, fuel combustion, and emissions control. Understanding gasoline volatility is essential for optimizing engine operation and mitigating potential issues such as cold starts and vapor lock.

During cold starts, particularly in colder climates, the volatility of gasoline determines how effectively the fuel can vaporize and mix with air for combustion. Low volatility gasoline may struggle to vaporize sufficiently, leading to difficulties in starting the engine and causing rough idling or stalling. In contrast, gasoline with higher volatility evaporates more readily, facilitating quicker engine starts and smoother operation, especially in cold weather conditions.

Vapor lock is another critical concern associated with gasoline volatility. Vapor lock occurs when gasoline vaporizes prematurely in the fuel system, forming vapor bubbles that disrupt fuel flow to the engine. This can result in engine hesitation, power loss, or even complete engine failure. Vapor lock is more likely to occur in hot ambient temperatures, as increased temperatures exacerbate gasoline volatility.

### **2.4.1 Reid Vapor Pressure (RVP)**

For SI engines, volatility is measured with Reid Vapor Pressure (RVP) test method, described in ASTM-D323 [46]. It determines the pressure exerted by the fuel vapor at 100°F (37.8°C) when the fuel is contained in a sealed vessel. The RVP value indicates the fuel's tendency to evaporate at typical operating temperatures. Gasoline with a higher RVP value has greater volatility and evaporates more readily, while lower RVP values indicate lower volatility.

### **2.4.2 Reid Vapor Pressure methodology**

The RVP test is carried out by pouring the fuel sample into a specially designed container, cooled at 0°C. The container is securely sealed to a gas chamber, to prevent leaks during the test. The assembly, containing the fuel sample, is then placed in a temperature-controlled water bath set to the specified test temperature of 37.8°C. This temperature simulates the conditions under which the gasoline's vapor pressure will be measured. After immersion in the water bath, the gasoline sample is allowed to equilibrate for a specified period, around 30 minutes. During this time, the gasoline vaporizes inside the bomb until the pressure reaches equilibrium. Once equilibrium is reached, the pressure gauge on the bomb is read to determine the pressure exerted by the gasoline vapor. This pressure reading represents the RVP of the fuel sample at the test temperature.

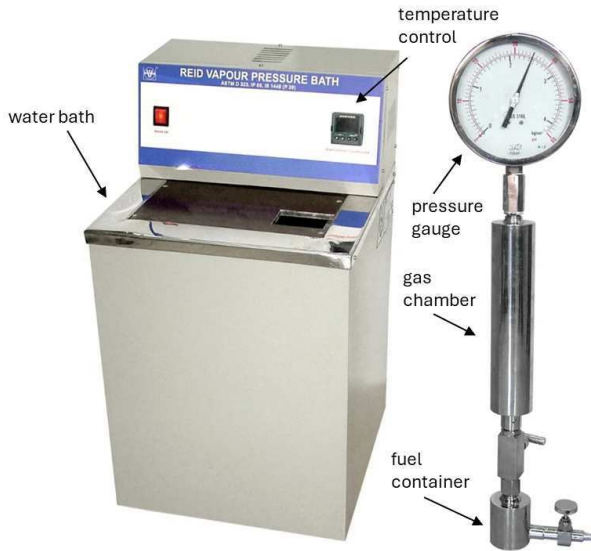


Figure 2.8: The components of the RVP setup.

### 2.4.3 RVP limits with European fuel standards

The EN228 standard imposes limits on fuel volatility to control emissions and ensure safe engine operation. Typically, maximum RVP values are specified for gasoline sold during different seasons. In winter months where cold start issues are prominent, minimum RVP values are located between 50 and 70 kPa, with an upper RVP limit situated at 80 to 100 kPa respectively. Lower RVP limits are mandated for summer months to prevent vapor lock issues in warmer weather and have 45 kPa as a lower limit, with the maximum RVP limit situated between 60 and 70 kPa, as indicated in Table 2.2.

Table 2.2: Season-dependent min and max RVP requirements for gasoline fuel according to EN228

| EN228 RVP limits | Summer | Winter |
|------------------|--------|--------|
| kPa, min         | 45     | 50-70  |
| kPa, max         | 60-70  | 80-100 |

## 2.5 Other SI fuel properties

### 2.5.1 Energy density

A fuel's energy density defines the Air-Fuel Ratio (AFR), a crucial parameter in combustion engines, representing the ratio of the mass of air to the mass of fuel present in the combustion mixture. A stoichiometric AFR refers to the ideal ratio where all fuel is combusted completely, typically around 14.7 parts of air to 1 part of fuel for gasoline. Lambda ( $\lambda$ ) is a dimensionless value used to express the AFR relative to the stoichiometric ratio. It is calculated by dividing the actual AFR by the stoichiometric AFR. For example, if the actual AFR is 14.7 and the stoichiometric AFR is also 14.7, the lambda value would be 1 ( $14.7/14.7 = 1$ ). Lambda values greater than 1 indicate a lean mixture (excess air), while values less than 1 indicate a rich mixture (excess fuel). The importance of lambda in spark ignition (SI) engines lies in its role in optimizing combustion efficiency and emissions. Lambda control allows the engine management system to adjust the air-fuel mixture to achieve the ideal stoichiometric ratio or other desired ratios based on operating conditions. This helps maximize fuel efficiency, power output, and emissions control, ensuring optimal engine performance while minimizing harmful pollutants.

Alcohols like ethanol or methanol contain less energy than gasoline per unit of volume. As a result, alcohols requires a larger volume of fuel to achieve the same air-fuel ratio as gasoline. Therefore, engines designed to run on ethanol or ethanol-gasoline blends typically require larger injectors to deliver the necessary fuel volume for proper combustion. In a flex-fuel engine, the fuel composition can vary between gasoline and ethanol blends, allowing the engine to run on different fuel types without requiring modifications. The engine management system monitors the alcohol content of the fuel and adjusts parameters such as fuel injection timing and duration to optimize performance. When the alcohol content increases, the engine management system increases the amount of fuel injected to maintain the desired air-fuel ratio and achieve optimal combustion. Conversely, when the alcohol content decreases, the injected fuel quantity is reduced accordingly to maintain proper engine operation. This flexibility allows flex-fuel vehicles to utilize a range of fuel compositions while maintaining performance and efficiency. In Europe however, the flex-fuel market is limited to only a few Member States [47]. The EN228 standard limits the maximum volume ratio of ethanol in gasoline to 10% since most vehicles and vessels are compatible with this ethanol/gasoline volume ratio. Higher blends may require adaptations of the power trains.

### 2.5.2 Chemical composition

A fuel's chemical composition is regulated through EN228 as well, mainly since the mix of hydrocarbons and additives in the fuel not only influence combustion characteristics and engine performance, but emissions as well [34]. The purity of the fuel, including its sulfur content and the presence of contaminants, affects emissions and engine longevity. Also, corrosive substances in the fuel can damage fuel system components while some additives may compounds that can harm certain engine components if used long-term. And finally, fuels should remain stable during storage to prevent degradation and the formation of deposits or gums that could harm the engine. Most EN228-restricted chemical components are listed in table 2.3 for illustration.

*Table 2.3: Limitations to chemical components according to EN228*

| <b>Component</b>            | <b>Units</b> | <b>Limits</b>            | <b>Main reason</b> |
|-----------------------------|--------------|--------------------------|--------------------|
| Lead                        | mg/l         | max 5.0                  | emissions          |
| Sulfur                      | mg/kg        | max 10.0                 | health aspects     |
| Manganese                   | mg/l         | max 2.0                  | health aspects     |
| Copper strip corrosion      | rating       | clear and bright at 50°C | engine damage      |
| Aromatics content           | % (V/V)      | max 35.0                 | emissions          |
| Benzene content             | % (V/V)      | max 1.0                  | emissions          |
| Oxygen content              | % (m/m)      | max 3.7                  | energy content     |
| Methanol content            | % (V/V)      | max 3.0                  | energy content     |
| Ethanol content             | % (V/V)      | max 10.0                 | energy content     |
| Ethers and other oxygenates | % (V/V)      | max 12.0 - max 22.0      | energy content     |

### 2.5.3 Emissions

Of the four types of hydrocarbons present in regular gasoline, aromatics have the most significant impact on emissions [48, 49]. Short-chain aromatics, which comprise the larger part of gasoline, are particularly noteworthy [49]. Higher contents of aromatics are generally associated with increased PM emissions [48–51], mainly because aromatics are stable molecules that decompose slowly, making them more likely to form soot precursors [34]. Aromatics also contribute significantly to unburned hydrocarbon (UHC) emissions [34, 48, 49, 51].

Additionally, they tend to exacerbate CO emissions [49, 51] and formaldehyde emissions [48], both of which are toxic. While aromatics do not directly impact NOx emissions, He et al. observed a slight increase in NOx emissions at higher engine speeds [49].

The other regular hydrocarbon types have a less pronounced influence on emissions composition and have therefore been less studied. Paraffins and olefins, for example, are the primary emission sources of volatile organic compounds (VOCs) [49].

Gasoline additives, including oxygenates like ethanol, play a crucial role in emissions reduction. Oxygenates, partly oxidized molecules containing oxygen atoms, emit less CO and UHCs due to their ability to provide additional oxygen during combustion [34, 48, 52, 53]. This leads to better and more complete combustion, facilitated by faster flame speed [52]. Oxygenated biofuels also generally emit less NOx and soot than hydrocarbon fuels due to their charge cooling effect, which lowers peak temperatures [53, 54]. Additionally, oxygenates typically have low sulfur content [34].

Ethanol, the most common oxygenate gasoline additive, has been extensively studied for its effects on emissions. It reduces CO and UHC emissions and generally lowers NOx emissions due to its higher latent heat of vaporization and lower heating value compared to gasoline, introducing a charge cooling effect [34, 50, 55, 56]. However, Mourad and Mahmoud suggest that the higher oxygen content in ethanol can increase NOx formation [57]. In GDI SI engines, Yang et al. found no significant change in NOx emissions with varying ethanol content [48]. Ethanol blending also decreases CO2 emissions due to its lower carbon-to-hydrogen ratio [34, 50]. However, ethanol's lower heating value may decrease engine power, potentially leading to cold start problems [55]. Ethanol also increases aldehyde emissions, including formaldehyde and acetaldehyde [48, 58].

These considerations underscore why EN228 imposes restrictions on the chemical composition of gasoline, as outlined in Table 2.3.

## 2.6 Chapter Conclusions

In this chapter, we delve into the fundamental operating principles of the four-stroke spark ignition (gasoline) engine. Following this exploration, we shift our focus to the general composition of gasoline and discuss the essential

properties it possesses, crucial for ensuring the smooth operation of a spark ignition engine. We specifically examine octane rating, volatility, energy density, and chemical composition, delving into their impact on engine performance. Additionally, we explore how these properties are measured and compare them to the EN228 regulations for gasoline fuels. These insights lay the groundwork for the subsequent chapter, where we introduce a pioneering second-generation spark ignition biofuel known as Ad-Libio.

# 3

## Sustainable fuel development

This chapter details the process of designing a second-generation naphthenic biofuel derived from woody biomass feedstock. It begins by clarifying the chemical principles involved, followed by an examination of the properties of its various components. To assess the fuel's suitability for use in spark ignition engines, blend laws were explored. Additionally, potential fuel compositions were calculated using a fuel blend calculator in conjunction with a publicly available database on spark ignition fuels.

## 3.1 Introduction

Amongst the different types of renewable fuels, hydrocarbon mixtures are and will remain the most efficient ones in terms of energy density. Biofuels are hydrocarbon-based renewable fuels and are typically generated out of biomass, plants and crops that during their lifetime capture CO<sub>2</sub> from the atmosphere. When converted into biofuel and upon combustion in the engine, the CO<sub>2</sub> that once was absorbed from the atmosphere is released again. When produced in a carbon-neutral way, the biofuel's carbon cycle is hence neutral, in contrast to fossil fuels which are derived from fossilized biomass that has been stored for millions of years under the earth's surface. Biofuels can partially replace fossil fuels when blended with a fossil fuel, without affecting the operation of legacy combustion engines in use today. Fossil fuel/biofuel blends are a viable pathway to a step-by-step replacement of fossil fuels by sustainable fuels. Currently, in Europe, B7 (a diesel fuel blend containing 7 volume% of biodiesel), E5 and E10 (gasoline with 5 and 10 volume% of bioethanol respectively) are widely in use. However promising the use of biofuels may seem, there are many limits regarding their use in current combustion engines: technical limits [59], ethical considerations with the first-generation biofuels [60] and the simple fact that there is not enough biomass available to fuel the world's transport needs with first-generation biofuels alone [61].

The production of biofuels from lignocellulosic biomass is found to be an emerging trend that can help - at least partly - overcome the previously discussed problems of first-generation biofuels. Lignocellulosic materials are among the most promising potential feedstocks for the production of biofuels such as bioethanol, butanol, biohydrogen, biogas (biomethane), and bio-oils like lignin oil. Lignocellulose can be obtained from woody crops that typically do not compete with agriculture and furthermore can be harvested on areas that are not fit for food production. Fuels derived from it are the so-called second-generation biofuels. Although care must be taken with production, one can state that the use of second-generation (2G) biofuels is considerably more ethically acceptable than first-generation biofuels [62].

The Ad-Libio project aims to develop novel advanced 2G biofuels to support the decarbonization of the transportation sector. The biorefinery process designed by researchers at KU Leuven [31] generates biofuels that can blend with fossil gasoline or replace gasoline altogether. In the latter case, they can be called sustainable drop-in fuels, which cannot be distinguished from current fuels by the engines in use today. The end products of the new process differ considerably from that of the more common biofuel products like biodiesel (fatty acid methyl esters

- FAME) or ethanol. It consists mainly of naphtha-type molecules and oxygenates. Being different from the products that are typically used in fossil fuel/biofuel blends, their usability in transportation fuel needs to be examined. In this work, the potential of this new biofuel as a blend component for, or replacement of, gasoline is explored. The impact on the most important fuel properties for SI engines is examined by means of a modified fuel blend property calculator [63] and a fuel compound property database [64]. The blend properties are compared against the EN228 norm for gasoline fuel to investigate whether blends with the new 2G biofuel components would be applicable in the short term as an addition to or a replacement for the commonly used 1G biofuels. A first look is taken at the origin of the 2G biofuel itself, after which the most important fuel parameters are examined for SI engines, relating them to the current European fuel norms. Calculations of blended SI fuel properties are then performed to estimate the potential of the naphthenic biofuel for on-road use.

## **3.2 Lignocellulosic biofuel explained**

### **3.2.1 The basic building blocks**

The production of biomass-based hydrocarbon fuels depends on many factors, such as biomass feedstock, the desired fuel type and the chosen production process itself. Whichever process is chosen, to make a biofuel truly renewable, the production must rely on renewable energy (e.g. green electricity or energy from renewable fuels). Renewable carbon can be found in lignocellulose, a polymeric composite in biomass, which provides rigidity to the plant and protects it against microorganisms. Second generation lignocellulosic biomass, derived from wood crops and agricultural residue whose consumption does not interfere with human needs, is widely available and cheap, making it interesting feedstock for emerging biorefinery applications. The structural and chemical features of lignocellulose vary strongly between different feedstocks but in general, lignocellulosic biomass can be divided into hardwood, softwood and grasses [65], as illustrated in Table 3.1.

Table 3.1: Example of lignocellulosic biomass classification, based on chemical composition.

|                  | Hardwoods |        | Softwoods |        | Grasses     |            |
|------------------|-----------|--------|-----------|--------|-------------|------------|
| % Dry Weight     | Birch     | Willow | Pine      | Spruce | Corn Stover | Rice Straw |
| Cellulose        | 38.2      | 43.0   | 46.4      | 43.4   | 35.6        | 34.2       |
| Hemicellulose    | 19.7      | 29.3   | 22.9      | 18.0   | 22.1        | 24.5       |
| Lignin           | 22.8      | 24.2   | 29.4      | 28.1   | 12.3        | 11.9       |
| NSC <sup>a</sup> | 19.3      | 3.5    | 1.3       | 10.5   | 30.0        | 29.4       |

<sup>a</sup>NSC includes non-structural compounds such as fats, oils, proteins, terpenes and others in low concentrations.

Each individual component of the lignocellulosic matrix has its intrinsic characteristics. While the first lignocellulosic building block, cellulose, exclusively exists of regularly ordered C6 sugars (e.g. glucose), the second building block, hemicellulose, contains diversely arranged C6 (e.g. mannose, galactose) and C5 sugars (e.g. xylose, arabinose). This is depicted in Figure 3.1.

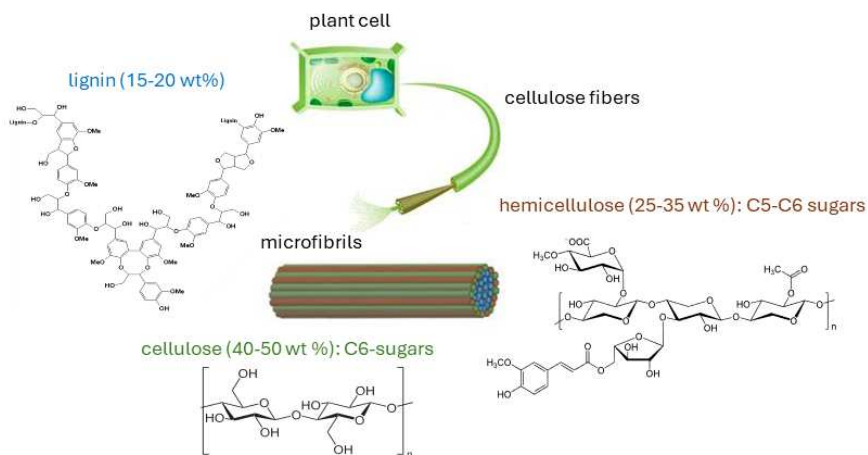


Figure 3.1: The different components of the lignocellulosic matrix.

Because of their relatively simple carbon skeleton, which can be cleaved into the desired hydrocarbon mixtures, cellulose and hemicellulose seem the most interesting ones to create hydrocarbon-based biofuels. By contrast, the third lignocellulosic building block, lignin, looks very different due to its irregularly

incorporated C9-C11 phenols. Notwithstanding the fact that it is not used in the Ad-Libio process, this lignin fraction could also serve as a biofuel precursor, creating different hydrocarbon mixtures with other fuel properties. As a consequence of their weak or unsaturated atom bonds, these biopolymers have a high degree of affinity to bind with hydrogen atoms. Hydrogen can therefore be used as a component to increase the energy density of the lignin-based polymers. Also, the Ad-Libio process uses hydrogen affinity to add green hydrogen (hydrogen from renewable sources like wind or solar energy) to the cellulosic and lignocellulosic polymers, which can therefore be considered as effective hydrogen energy acceptors. This makes the Ad-Libio process a hybrid process, where green carbon is combined with green hydrogen to form a combustible hydrocarbon mix. Before individual lignocellulosic components (i.e. cellulose, hemicellulose, lignin) can act as a biofuel precursor, raw biomass needs to be disassembled. For this purpose, the wood is mechanically treated (e.g. debarked, cleaved, milled) to enable further processing. Next, the obtained wood particles undergo basic extraction of the non-structural compounds such as fats, oils, proteins and terpenes, which can be used for other bio-based applications. In a first step of the actual biomass fractionation, (step 1, Figure 3.2), lignin is extracted from the lignocellulosic network in the presence of an alcohol solvent and subsequently stabilized by catalytically depolymerizing it in stable fragments.

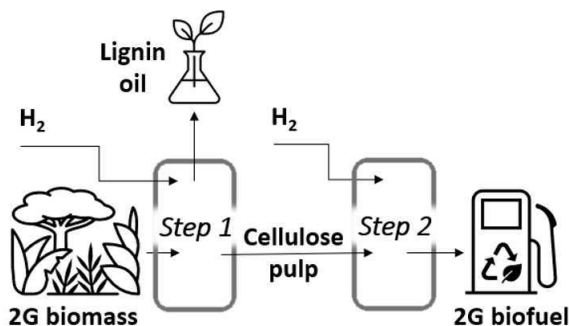


Figure 3.2: Overview of the novel bio naphtha process.

Due to the mild reaction conditions (i.e. temperature and hydrogen pressure), cellulose and a large part of hemicellulose stay untouched throughout this refinery process. So besides the lignin oil a solid pulp is retained, which predominantly consists of C6 and C5 sugars. This fibrous sugar pulp is the ideal source for implementation of energy-rich hydrogen molecules, yielding a hydrocarbon mixture in the naphtha-range (C5-C6 molecules) [31].

### 3.2.2 A novel catalytic treatment

Bioethanol production from 1G feedstock is a well-developed and well-established sugar upgrading method. However, bioethanol production from 2G feedstock involves enzymatic saccharification followed by sugar fermentation through yeast cells, which comes with some disadvantages:

- Not every sugar type is transformed with the same efficiency due to differences in type affinity with yeast cells.
- One third of the carbon feedstock is released as carbon dioxide during ethanol formation, which not only is a greenhouse gas but also means that the available carbon is used inefficiently.
- Scaleup hurdles such as huge cost of the enzyme cocktails for saccharification and poor growth of fermenting microorganisms in industrial environments may hinder the breakthrough of this saccharification process from 2G feedstock.

Compared to 2G bioethanol production through fermentation, the bionaphtha production process has some advantages. This process is used in the second part of the biorefinery process (step 2, Figure 3.2). A selective conversion, which is only possible within a biphasic solvent system consisting of two immiscible solvents that form two distinct liquid phases, takes place. Each liquid phase contains its own catalyst with its own specific function. Reactions take place under relatively low temperature (250°C) and relatively low hydrogen pressure (50 bar), making it a mild and sustainable approach compared to more energy-intensive processes like gasification (800-900 °C), pyrolysis (300-500 °C) or liquefaction (200-250 °C but at elevated pressures of 100-250 bar). In the aqueous compartment, the (hemi)cellulosic pulp is broken up into its monomeric sugars (i.e. glucose, mannose, galactose, xylose, arabinose). Subsequently, these sugars are dehydrated to (hydroxymethyl)furfural intermediates, losing part of the oxygen in the form of water. As a result of the intermediates' changing solubilities regarding the different solvents, the next reaction steps occur in the organic compartment. In short, these transformations lead to a further oxygen removal, by adding renewable energy to the molecules in the form of hydrogen. As an end result, this cascade gives rise to hydrocarbons containing five to six carbon atoms in their skeleton. The most prevalent components are hexane, pentane, methyl cyclopentane, 2-methylpentane, cyclopentane, 2,5-dimethyltetrahydrofuran, all of which could act as fuel components for internal combustion engines. The last four molecules are oxygenates. It should be noted that the amount of oxygen in the

outcome of the process can be regulated by controlling the amount of hydrogen. The more hydrogen used in the process, the lower the amount of oxygenates in the resulting naphthenic biofuel and the higher the volumetric energy content. A typical biofuel composition of the naphtha process outcome can be found in Table 3.2, with a simplified visual representation illustrated in Figure 3.3.

Table 3.2: Typical outcome of the Ad-Libio process.

| Biofuel component   | Volume % |
|---|----------|
| n-hexane  | 70       |
| n-pentane   | 13       |
| methyl cyclopentane   | 9        |
| 2-methylpentane   | 1        |
| cyclopentane  | 1        |
| 3-methylpentane, methyl/ethyl/propyl cyclohexane, butane, methylpropane | 5        |
| tetrahydropyran, dimethyl tetrahydrofuran, methyl tetrahydrofuran       | 1        |

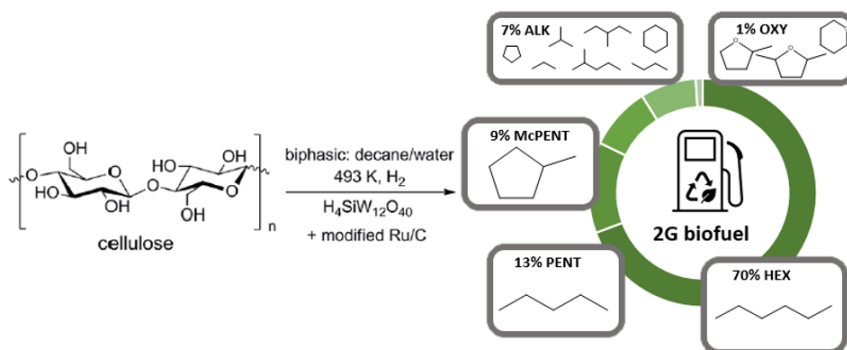


Figure 3.3: Ad-Libio process outcome, simplified.

To avoid waste production, each output stream needs to be purified for further use or recycling. First, the gaseous phase, mainly comprising residual hydrogen, butane, propane and methane, is removed from the liquid reaction mixture. Second, the aqueous and organic layer, together forming the liquid phase, are separated from each other. The aqueous compartment can be recycled without additional treatment, since it remains untouched during reaction. Unreacted intermediates which are possibly left behind, are converted in a subsequent run.

The organic compartment on the other hand, is further treated by separating the naphtha-type biofuel from the less volatile solvent. This organic solvent can be reused, producing no direct waste streams overall. The typical biofuel process outcome is investigated next for suitability as an SI fuel.

### **3.3 Fuel property investigation**

#### **3.3.1 Investigation of separate components with a fuel property database**

Thanks to a fuel property database from RWTH Aachen university [64], the relevant properties of each naphtha-type fuel component can be looked up. The database contains 615 potential SI engine fuel components that encompass a wide range of chemical compounds. Each component's physical and chemical properties have been compiled into a comprehensive overview. These values have been primarily derived from experimental data sourced from literature reviews and evaluations. In instances where experimental evidence is lacking, values have been estimated using advanced models like artificial neural networks or established quantitative structure-property relationship models. The available compounds and associated properties are listed in Table 3.3.

*Table 3.3: Available compounds and associated properties in RWTH Aachen SI fuel database*

| <b>Available chemical compounds</b> | <b>Available properties</b> |
|-------------------------------------|-----------------------------|
| alkanes                             | RON                         |
| alkenes                             | MON                         |
| dienes                              | octane sensitivity          |
| trienes                             | cetane number               |
| aromatics                           | heat of vaporization        |
| alcohols                            | liquid density              |
| ketones                             | surface tension             |
| esters                              | viscosity                   |
| ethers                              | boiling point               |
| furanics                            | melting point               |
| oxygenated benzenoids               | vapor pressure              |
| nitrogenated components             | lower heating value         |
|                                     | H/C ratio                   |
|                                     | oxygen content              |
|                                     | molecular weight            |
|                                     | water solubility            |

The database is available on Aachen University's website [66]. The tool is based on Microsoft Excel and is easy to use. The fuel compound for which the properties are requested can be entered in a search field, as illustrated in Figure 3.4, after which the data becomes available to the user.

## Fuel Database Search Engine

Fuel property database corresponding to: A property database of fuel compounds with emphasis on spark-ignition engine applications, Preprint submitted to Applications in Energy and Combustion Science (2020).

This search engine only provides a quick overview of fuel property data. Detailed information on the fuels, their property values as well as metadata, explanations, and references are provided in the other worksheets of this document.

Name of Compound (optional):

CAS number (optional):

|                       |   |                               |  |
|-----------------------|---|-------------------------------|--|
| Formula:              | <input type="text" value="C6H14"/>                    | Fuel class:                   | <input type="text" value="Linear alkanes"/>          |
| Molecular Weight:     | <input type="text" value="86.17536"/> g/mol           | SMILES code:                  | <input type="text" value="CCCCCC"/>                  |
| Boiling Point:        | <input type="text" value="69"/> °C                    | Melting Point:                | <input type="text" value="-95.3"/> °C                |
| Heat of Vaporization: | <input type="text" value="365.5"/> kJ/kg              | Vapor Pressure:               | <input type="text" value="20.4"/> kPa                |
| Lower Heating Value:  | <input type="text" value="44.5"/> MJ/kg               | Density:                      | <input type="text" value="654.7"/> kg/m <sup>3</sup> |
| Kinematic viscosity:  | <input type="text" value="0.498"/> mm <sup>2</sup> /s | Surface Tension (prediction): | <input type="text" value="20.3 ± 3"/> mN/m           |
| Solubility:           | <input type="text" value="0.0095"/> g/L               | Oxygen content:               | <input type="text" value="0"/> wt%                   |
| H/C ratio:            | <input type="text" value="2.33"/>                     |                               |  |
| RON:                  | <input type="text" value="24.8"/>                     | MON:                          | <input type="text" value="26"/>                      |
| Blending RON:         | <input type="text" value="19"/>                       | Blending MON:                 | <input type="text" value="22"/>                      |
| RON (ANN prediction): | <input type="text" value="27.2"/>                     | MON (ANN prediction):         | <input type="text" value="27.8"/>                    |
| OS (ANN prediction):  | <input type="text" value="0.3"/>                      |                               |  |

Figure 3.4: Fuel property database lookup result for n-hexane. The database contains more than 600 fuel components.

Several naphtha fuel components from the novel process were looked up from the database and are listed against the EN228 norm in Table 3.4. Upon examination of the individual Ad-Libio component properties, some preliminary observations can be made:

- N-hexane and n-pentane have a RON and MON number that is significantly lower than the EN228 required value of 95. With a volumetric share of 70% and 13% respectively, these components represent the major part of the Ad-Libio blend.
- Other components show more promising RON and MON numbers, but 2,5-dimethylfuran could pose a conflict with EN228, especially regarding

its oxygen content. Care should be taken in cases where it is combined with other oxygen-containing additives to formulate a fuel blend.

*Table 3.4: Properties of some of the naphtha process products, compared to EN228 requirements for gasoline fuel. Next to the RON and MON indication, components that are limited in quantity (expressed in maximum vol%) by the fuel norm are indicated as ‘not ok’ (nok) by which is meant that they must be limited in quantity to comply as a fuel blend component.*

|                     | RON<br>(min) | MON<br>(min) | olefins<br>(alkenes)? | aromatics? | oxygen<br>content? | ethers?                    | other oxygenated<br>molecules |
|---------------------|--------------|--------------|-----------------------|------------|--------------------|----------------------------|-------------------------------|
| Gasoline E10        | 95           | 85           | max 18 v%             | max 35 v%  | max 2.7 m%         | until max 2.7<br>m% oxygen | until max 2.7<br>m% oxygen    |
| n-hexane            | 24.8         | 26           | ok                    | ok         | ok                 | ok                         | ok                            |
| n-pentane           | 61.7         | 61.9         | ok                    | ok         | ok                 | ok                         | ok                            |
| Methyl cyclopentane | 91.3         | 80           | ok                    | ok         | ok                 | ok                         | ok                            |
| cyclopentane        | 101.3        | 85           | ok                    | ok         | ok                 | ok                         | ok                            |
| 2-methylpentane     | 73.4         | 73.5         | ok                    | ok         | ok                 | ok                         | ok                            |
| 2,5-dimethylfuran   | 101.3        | 88.1         | nok                   | ok         | nok                | nok                        | ok                            |

It appears likely that the renewable light naphtha-type fuel does not fully comply with the requirements outlined in EN228, and thus, cannot be used as a drop-in replacement for gasoline. Given this, further investigation into the suitability of Ad-Libio fuel components for blending is performed in the next sections.

### 3.3.2 Property calculations of blended components

In literature, research on SI and HCCI engines [67–69] has uncovered intriguing potential for utilizing naphtha-type fuel components in low-temperature combustion concepts. However, it’s important to note that these fuels do not meet EN228 compliance standards. Considering E10 gasoline fuel where octane number, along with the maximum amount of oxygen and aromatics content is stipulated, a first objective would be to create an EN228-compliant fuel with the Ad-Libio naphtha-type blending components instead of bioethanol. Typically, BOB blends are used to create gasoline blends with fossil and sustainable components. BOB stands for ‘Before Oxygenate Blending’, an unfinished gasoline blend that only lacks the addition of the predetermined volume of oxygenates (typically ethanol) to be a finished (e.g. E10 gasoline) SI fuel. BOB blends could be used to formulate EN228-compliant blends with the Ad-Libio fuel components. In order to efficiently predict the properties of gasoline in an efficient way, blended with naphtha components, a fuel blend property calculator [63] is used.

The project undertaken by the calculator's author Vinke of Bath University (UK) resulted in a tool for computation of fuel blending characteristics. These tools exist in the industry but have large budgets for development behind them and are undisclosed to the public. In addition to this, these tools are highly complex with specific software packages associated to them. The tool created by Vinke acts as a publicly available calculator using Microsoft Excel. Excel was chosen due to its ease of use, easy database management and mass accessibility. By implementing a dynamic database and an automatically updating script within the dataset, it is possible for the user to select new database entries without any modification to the script or worksheet. The tool is capable of estimating fuel mixture characteristics for any variation of fuel blends. The layout of the tool includes one worksheet for the database, one for the calculations and one for input and outputs of the desired values. In the database worksheet of the calculator, blend components are entered with their respective properties (mostly available in the RWTH Aachen fuel database).

Requested input data is name, type, density, LHV, molar mass, molecular carbon-hydrogen-oxygen ratio, stoichiometric laminar flame speed, RON, MON, Reid Vapor Pressure. In its original version, the user can select up to six blend components using a drop-down menu and input the volume fraction of each blend component. The drop-down menu works in conjunction with the database worksheet and automatically recognizes any fuels that previously have been added to the calculator's database. The calculations are based on relatively simple formulas, listed in table 3.5 with associated background information available from [63], providing estimates that are not validated for all mixtures.

Table 3.5: Overview of the formulas used to compute all mixture properties

| Blend Value                         | Formula   |
|-------------------------------------|---|
| Density (kg/m <sup>3</sup> )        | Sum of volume fraction times density of each component<br>$\rho_{Blend} = \rho_1 * \phi_1 + \rho_2 * \phi_2 + \dots$  |
| LHV (MJ/kg)                         | Sum of mass fraction times LHV of each component<br>$LHV_{Blend} = \omega_1 * LHV_1 + \omega_2 * LHV_2 + \dots$   |
| Molar Mass (kg/kMol)                | Sum of mole fraction times molar mass of each component<br>$M_{Blend} = x_1 * M_1 + x_2 * M_2 + \dots$  |
| Stoichiometric Air fuel ratio (AFR) | Sum of mass fraction times Stoichiometric AFR of each component<br>$AFR_{Blend} = \omega_1 * AFR_1 + \omega_2 * AFR_2 + \dots$  |
| Volumetric energy density (MJ/l)    | $\eta_{volumetric,blend} = LHV_{blend} * (\frac{\rho_{blend}}{1000})$   |
| Volumetric CO <sub>2</sub> (kg/l)   | Sum of volume fraction times carbon mass fraction of each component<br>$\theta_{CO2Blend} = \phi_1 * \omega_{carbon1} + \phi_2 * \omega_{carbon2} + \dots$  |
| Gravimetric CO <sub>2</sub> (kg/kg) | $\nu_{CO2Blend} = \theta_{CO2Blend} * \frac{1}{\rho_{Blend}} * 1000$  |
| RON                                 | Sum of mole fraction times RON of each component<br>$RON_{Blend} = x_1 * RON_1 + x_2 * RON_2 + \dots$   |
| MON                                 | Sum of mole fraction times MON of each component<br>$MON_{Blend} = x_1 * MON_1 + x_2 * MON_2 + \dots$   |
| Molar Ratio Products-Reactants      | Sum of mole fraction times molar ratio between products and reactants<br>$\eta_{Blend} = x_1 * \eta_1 + x_2 * \eta_2 + \dots$   |
| Oxygen content by mass in %         | Sum of mass fraction times oxygen mass fraction of each component<br>$O_{Blend} = \omega_1 * \omega_{oxygen1} + \omega_2 * \omega_{oxygen2} + \dots$  |
| Reid Vapor Pressure (RVP) (kPa)     | The formula contains conversion factors from psi to kPa. (Jarullah, 2013)<br>$RVP_{Blend} = (\phi_1 (\frac{RVP_1}{6.895})^{1.25} + \phi_2 (\frac{RVP_2}{6.895})^{1.25} + \dots)^{\frac{1}{1.25}} * 6.895$ |
| Heat of vaporisation (HoV) (kJ/kg)  | Sum of volume fraction times HoV of each component<br>$HoV_{Blend} = HoV_1 * \phi_1 + HoV_2 * \phi_2 + \dots$   |

A validation of the tool for RON, MON, LHV, stoichiometric AFR and volumetric CO<sub>2</sub> was done by developer Vinke, against blend values from literature. Next to dual blends used for validation, more complex ternary ones were taken from the paper by Turner et al. [17]. The ternary blends investigated in this paper consisted of gasoline 29.5%, ethanol 42.5%, methanol 28%; and gasoline 37%, ethanol 21%, methanol 42%. The resulting deviations of the calculated fuel properties relative to the measured ones, are shown in Table 3.6. The comparison between the results from the study of Turner et al. and the calculated fuel properties with ternary blends showed minimal discrepancies. The maximum error is 2.22%, all other errors are below 2% and some are close to or at 0%. The validation for the blending calculator was successful for the chosen components and resulting properties, resulting in the conclusion that the blending logic works for multi-component blends.

*Table 3.6: Validation of the fuel property calculator with Gasoline-Ethanol-Methanol blends and overview of the data generated by the calculator*

|         | Property                          | Measured | Fuel properties calculator | Difference |
|---------|-----------------------------------|----------|----------------------------|------------|
| Blend 1 | RON                               | 108.70   | 106.78                     | 1.78       |
|         | MON                               | 90.30    | 88.68                      | 1.81       |
|         | LHV (MJ/L)                        | 22.70    | 22.65                      | 0.22       |
|         | Stoichiometric AFR                | 9.69     | 9.84                       | 1.54       |
|         | Volumetric CO <sub>2</sub> (kg/l) | 1.62     | 1.62                       | 0.00       |
| Blend 2 | RON                               | 108.50   | 106.57                     | 1.79       |
|         | MON                               | 90.30    | 88.32                      | 2.22       |
|         | LHV (MJ/L)                        | 22.71    | 22.66                      | 0.22       |
|         | Stoichiometric AFR                | 9.71     | 9.89                       | 1.84       |
|         | Volumetric CO <sub>2</sub> (kg/l) | 1.62     | 1.62                       | 0.00       |

### 3.3.3 Improvements to the blend calculator

Assuming that the blend property calculator shows the same accuracy for other fuel types than gasoline, methanol and ethanol, a prediction could be made for fuel blends based on naphthenic type fuels. The typical Ad-Libio fuel components and their respective quantities of Table 3.2 are used to initiate the calculations.

Some shortcomings of the initial calculator had to be solved, before actual calculations could be made:

- The maximum input number was limited to six compounds, insufficient for a direct calculation of a blend with all Ad-Libio components.
- The minimum required volumetric percentage input is limited to 1 vol% per component.

After adaptation, the calculator is now capable of calculating blended properties of up to 20 components. The smallest volumetric input is lowered to 0.1 vol%. During the adaptation, the calculator was combined with the Aachen fuel database in a way that the selection of fuel components is now reduced to clicking a tick box, after which the component becomes available in the drop-down menu of the calculation sheet. For illustration purposes, the calculator interface is shown in figure 3.5.



### 3.3.4 Initial EN228-compliance checks for RON

Entering the components listed in Table 3.7 in the calculator resulted in an estimated RON of 41.2 for the first iteration of the Ad-Libio process outcome. For the furans, an even volume% of 0.33 was assumed per component. For n-butane, methyl- and ethyl cyclohexane, 1.6, 1.7 and 1.7 vol% was assumed respectively. As a reminder, the blended RON calculation is based on a linear molar fraction of each component in the blend, as expressed in Equation 3.1:

$$RON_{Blend} = x_1 * RON_1 + x_2 * RON_2 + \dots \quad (3.1)$$

Table 3.7: Calculation of the octane number of the Ad-Libio fuel blend

|   | Vol ratio | RON       |
|---|-----------|-----------|
| n-hexane  | 70        | 24.8      |
| n-pentane   | 13        | 61.7      |
| methyl cyclopentane   | 9         | 91.3      |
| 2-methylpentane   | 1         | 73.4      |
| cyclopentane  | 1         | 101.3     |
| 3-methylpentane, methyl/ethyl/propyl- cyclohexane,<br>butane, methylpropane | 5         | 45 to 103 |
| tetrahydropyran, dimethyl tetrahydrofuran,<br>methyl tetrahydrofuran        | 1         | 73 to 101 |
| <b>Blended RON calculation</b>  |           | 41.2      |

RON calculations based on linear mole fractions can provide a good initial insight into RON behavior. However, the RON behavior of blends containing naphthenic compounds, as listed above, could not be found in the literature and thus cannot be verified. Nevertheless, the disappointing - but not unexpected - results lead to the conclusion that, given the low RON of the naphthenic blend, alterations are likely necessary for the naphthenic fuel to be useful as a blend component, at best. This becomes clear when the calculator is used in an attempt to make an EN228-compliant fuel blend with a maximum of non-fossil fuel content. A

maximum of 2.7 mass% of oxygenates is taken into consideration as a limiting parameter. In this exercise, gasoline is defined as an average  $C_8H_{14}$  molecule, with a RON of 95 and a MON of 85. The volumetric content of the naphtha fuel is increased until the maximum oxygenate mass% of 2.7, the EN228 limit, is reached. The conclusion is that a maximum volume percentage of 16 vol% can be obtained with naphtha fuel blends. With a RON 95 BOB fuel, this would however result in a fuel blend with a RON of 84,60 which is not EN228-compliant. Reverse calculation would require a BOB fuel with a RON of 108 in order for the blend to be EN228-compliant with a RON of 95 and with a maximum of 2.7 mass% of oxygen content.

## **3.4 Revised production process outcome**

### **3.4.1 RON estimation of alternative blends**

The Ad-Libio production process parameters were altered in an attempt to increase the RON of the end product. By varying different process parameters, isomerization of the initial molecules could be obtained and different alternative process outcomes could quickly be calculated. Table 3.8 lists ten different theoretical fuel blends, with each “x” indicating the presence of a fuel component in the blend. For simplicity, the exact volume fractions of the components are not listed.

Table 3.8: Alternative Ad-Libio fuel compositions

| <b>Blend #</b>        | <b>1</b>  | <b>2</b>  | <b>3</b>  | <b>4</b>  | <b>5</b>  | <b>6</b>  | <b>7</b>  | <b>8</b>  | <b>9</b>  | <b>10</b> |
|-----------------------|-----------|-----------|-----------|-----------|-----------|-----------|-----------|-----------|-----------|-----------|
| Pentane               | x         | x         |           | x         | x         | x         | x         | x         | x         | x         |
| Methylbutane          |           | x         | x         | x         | x         | x         | x         | x         | x         | x         |
| Hexane                | x         | x         |           | x         | x         | x         | x         | x         | x         | x         |
| 2-methylpentane       |           | x         | x         | x         | x         | x         | x         | x         | x         | x         |
| 3-methylpentane       |           | x         | x         | x         | x         | x         | x         | x         | x         | x         |
| 2,2-dimethylbutane    |           | x         | x         | x         | x         | x         | x         | x         | x         | x         |
| 2,3-dimethylbutane    |           | x         | x         | x         | x         | x         | x         | x         | x         | x         |
| Ethanol               |           |           |           |           | x         | x         | x         | x         | x         | x         |
| Pentanol              |           |           |           | x         |           |           |           |           |           |           |
| Hexanol               |           |           |           | x         |           |           |           |           |           |           |
| Methylfuran           |           |           |           |           |           | x         |           |           |           |           |
| Dimethylfuran         |           |           |           |           |           | x         |           |           |           |           |
| Methylbenzene         |           |           |           |           |           |           | x         | x         | x         | x         |
| Ethylbenzene          |           |           |           |           |           |           | x         | x         | x         | x         |
| Propylbenzene         |           |           |           |           |           |           | x         | x         | x         | x         |
| 1- & 2-pentene        |           |           |           |           |           |           |           | x         |           | x         |
| 1-, 2- & 3-hexene     |           |           |           |           |           |           |           |           | x         | x         |
| <b>Calculated RON</b> | <b>38</b> | <b>76</b> | <b>84</b> | <b>71</b> | <b>82</b> | <b>91</b> | <b>94</b> | <b>95</b> | <b>92</b> | <b>94</b> |

The fuel blend calculator proved to be helpful by providing fast estimated RON calculations of every possible blend. It is clear that the isomerization of the original molecules leads to a significant increase in knock-resistive properties of the Ad-Libio fuel, with blend no 8 being the most promising. It was decided to synthesize this specific blend in the lab and have it tested for research octane number (RON), motor octane number (MON) and Reid Vapor Pressure according

to ASTM. The results, illustrated in the lab report in Figure 3.6 confirmed the initial calculations with a RON of 96.2 and a MON of 86.5.



UNIVERSITEIT GENT  
Sint-Pietersnieuwstraat 41  
9000 GENT

### ANALYTICAL REPORT LA-649355.01.A01

grade GASOLINE  
reference no. Bestelnummer: 4205162100 - BTW nr: BE0248015142

sample received on 15th March, 2023 from Universiteit Gent, Gent, marked as indicated below  
sample 001 "GHENT UNIVERSITY  
UGENT SYNTHETIC FUEL (2,5I)"

date received 15.03.2023  
start analyses 16.03.2023

|  |      |
|--|------|
|  | 001  |
| <u>Knock characteristics</u> , octane number                       |      |
| <sup>B</sup> - motor method<br>(MON - method ASTM D 2700)          | 86.5 |
| <sup>B</sup> - Research method<br>(RON - method ASTM D 2699)       | 96.2 |
| <u>Reid vapour pressure</u> at 37.8 °C, kPa<br>(method ASTM D 323) | 47.3 |
| <u>Dry vapour pressure</u> on 0.5L, kPa<br>(method ASTM D 5191)    | 48.1 |
| "Storage & disposal/destruction of sample"                         |      |

<sup>B</sup> The analyses marked with B are BELAC ISO 17025 accredited (No. 005-TEST)

Figure 3.6: ASTM Lab report of Ad-Libio blend 8

### 3.4.2 RVP estimation of the most promising fuel blend

Since RVP is an equally important parameter, an attempt was made to calculate the RVP of the most promising blend. As a reminder, Jarullah's blend law is given in Equation 3.2:

$$RVP_{Blend} = \left( \phi_1 \left( \frac{RVP_1}{6.895} \right)^{1.25} + \phi_2 \left( \frac{RVP_2}{6.895} \right)^{1.25} + \dots \right)^{\frac{1}{1.25}} * 6.895 \quad (3.2)$$

The calculated result leads to a RVP of 16.86 kPa, as opposed to the ASTM D323 test result of 47.3 kPa, as illustrated in Figure 3.6. The calculator's equation for RVP is therefore considered to be inaccurate for these types of blends. This is no

surprise, as vapor pressures of fuels that are composed of non-ideal components, particularly in the presence of oxygenates, are difficult to accurately predict with simple methods [70].

The inclusion of oxygenates in fuel can lead to changes in volatility behavior due to the introduction of non-ideal interactions into fuel blends. As a result, the vapor pressure of a blend does not show a linear correlation with the concentration of oxygenates.

Research in the fuel industry extensively explores the effects of short-chain alcohols such as methanol and ethanol [71–73]. It is observed that the addition of a relatively small volume (5% - 10%) of these alcohols significantly raises RVP, as demonstrated in Figure 3.7. However, with further increases in alcohol content, the impact of ethanol on RVP diminishes, and in some cases, higher volume percentages of ethanol result in lower RVP than the base fuel. Therefore, fuels with lower RVP or higher saturated hydrocarbon content experience greater increases in RVP upon the addition of alcohol [74].

Utilizing alcohols with longer chain lengths results in decreased volatility of the blend. Therefore, blending larger chain alcohols such as propanol and butanol does not lead to an increase in RVP for small volume percentages. Propanol ( $C_3H_7OH$ ) marginally increases RVP at very low concentrations, whereas butanol ( $C_4H_9OH$ ) decreases RVP even at minimal concentrations, as illustrated in Figure 3.7. Further elongation of the carbon chain continues to decrease RVP.

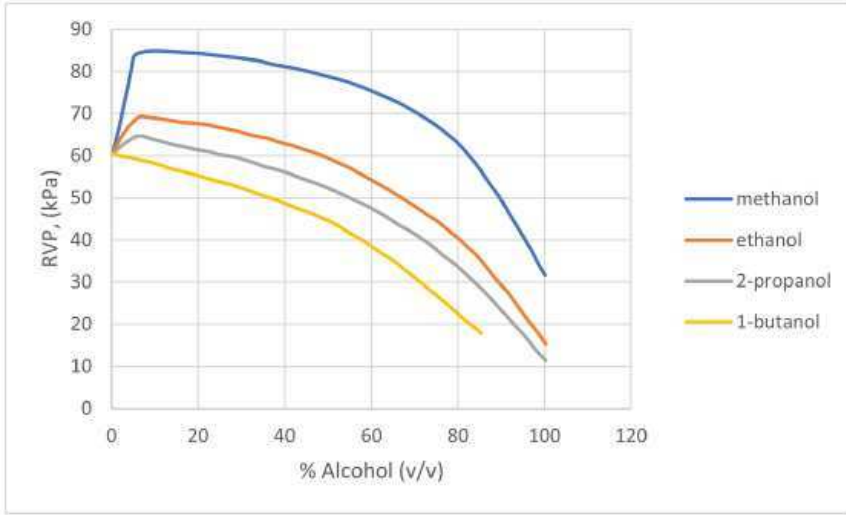


Figure 3.7: The effect on a blend's RVP with increasing alcohol content, modified from [71].

In case of an ideal mixture, Raoult's law, as depicted in Equation 3.3, describes the vapor pressure ( $P$ ) of a mixture at a specific temperature, where  $P_i$  represents the vapor pressure of component  $i$ , and  $x_i$  denotes its mole fraction [71].

$$P = \sum P_i x_i \quad (3.3)$$

The calculation of RVP involves the utilization of Equation 3.4, also known as the Clausius-Clapeyron equation [75]. Within this equation, RVP represents the Reid Vapor Pressure (kPa),  $P$  denotes the pressure (kPa) of the mixture at a given temperature  $T$  in Kelvin,  $T_r$  specifies the temperature at which the RVP is assessed (37.8 °C or 310.95 K),  $\Delta H_m$  represents the molar enthalpy of the mixture (J/mol), and  $R$  denotes the gas constant (8.3145 J/mol/K). This model becomes unusable when oxygenates, especially short-chain oxygenates, are blended with gasoline as those do not behave like ideal components.

$$P_r = P \times \exp \left\{ \frac{\Delta H_m}{R} \left( \frac{1}{T} - \frac{1}{T_r} \right) \right\} \quad (3.4)$$

In 1985, Furey conducted an analysis of volatility characteristics across various fuels [76]. From this study, a simple correlation was derived, expressed in

Equation 3.5, capable of capturing the initial increase in RVP. Here,  $C$  represents the alcohol concentration, while constants  $k$  and  $n$  depend on the neat alcohol and gasoline components. Despite numerous adjustments aimed at improving accuracy, these models still demonstrated limited precision when applied to newly developed fuels. Consequently, a unique model was required for each new fuel, resulting in a labor-intensive and inefficient process. Therefore, the goal of developing a predictive model for the RVP of new fuels before their production remains unmet [70].

$$RVP = kC^n \quad (3.5)$$

Due to its complexity and dependence on fuel components, further exploration into RVP calculation was considered a non-priority for the remainder of this study. Instead, emphasis was placed on experimental RVP investigation using ASTM-compliant equipment, leveraging the relative simplicity of the test, following the development of blends with promising RON values.

### 3.5 Chapter conclusions

A new second-generation potential biofuel is being developed for use in SI engines. Using a fuel blend property calculator, adjustments to the production process can be made quickly, resulting in a promising spark ignition fuel candidate with regards to RON. However, initial outcomes were unsuitable for on-road use. Modifications to the production process based on insights from a fuel database and a modified fuel blend calculator led to the creation of naphthenic fuel blends that could potentially replace gasoline.

The suitability of the most promising blends was confirmed through ASTM-compliant tests for RON and MON. However, accurately predicting RVP proved challenging due to the non-linear behavior of blends containing non-ideal components like short-chain alcohols. As a result, no immediate solution was pursued for correcting the RVP predictions from the calculator. Instead, future blends will be tested experimentally using ASTM-compliant equipment.

The next chapter will delve into the experimental framework for validating Ad-Libio fuel properties, focusing on RON.

# 4

## Development of a pressure-oscillation-based octane quantification method

This chapter outlines the experimental validations conducted during the development of Ad-Libio, a second-generation sustainable naphthenic spark ignition fuel. Initially, efforts are focused on devising a method to conduct in-house RON-like measurements using non-ASTM-compliant equipment available in the UGent laboratory. This endeavour led to the refinement of an alternative octane measurement approach that aligns more closely with contemporary knock detection technology in current engines, proposing a substitute for the outdated ASTM RON and MON measurement techniques. Subsequently, the effectiveness of this alternative method was evaluated against the ASTM method.

## 4.1 Insights into octane rating

### 4.1.1 Introduction

During the development of Ad-Libio, the fuel property calculator described in the previous chapter was utilized effectively as a screening tool to verify multiple blend compositions for their suitability as SI fuels, with a particular focus on octane number and Reid Vapor Pressure values. Since the calculator is considered as an estimation tool only, both important fuel properties needed experimental verification. Verification of Reid Vapor Pressure values was facilitated by the presence of ASTM D323-compliant equipment [77] in the laboratory. However, verifying RON and MON is more challenging because the CFR engine in the laboratory is non-ASTM compliant. The engine, having been previously utilized as a test frame for various combustion research projects, has long been stripped of its original RON measuring equipment. To this end, an alternative method was sought to replace the ASTM RON test, allowing quick and efficient in-house verification of different experimental blends. In the next sections, the RON and MON methods are analysed to provide deeper understanding of the principles behind octane measurement, followed by the sections describing the steps that were taken in the development of an alternative RON estimation method that can be performed with non-ASTM equipment, commonly found in an engine lab.

### 4.1.2 The history of RON and MON development

As explained in section 2.3.2, the knock phenomenon became a subject of investigation since the early 1900s [39] and around 1930 the Cooperative Fuel Research committee proposed the octane scale that is still in use today. Per definition, the octane number (ON) of a PRF blend is equal to the volumetric ratio of iso-octane in a mixture of iso-octane and n-heptane, as stated in Equation 2.1.

Based on the octane scale, two fuel test methods were developed. The research octane method, described in ASTM-D2699 [40], associates a sample fuel with a research octane number (RON). The motor octane method, described in ASTM-D2700 [41], was developed later to represent fuel behavior at more severe operating conditions and rates a fuel with a motor octane number (MON). The MON method was developed in response to on-road testing that revealed the inadequacy of RON alone, since some fuels that met RON specifications did not seem to meet performance expectations on the road (The 1932 and 1933 Uniontown tests [39]).

Section 2.3.3 describes how the MON test provides additional information on a fuel's resistance to knocking under different driving conditions by simulating higher-speed and heavier-load engine operation, with the main differences between RON and MON conditions being listed in Table 2.1.

The CFR Committee recognized the need for periodic revisions of the MON method, acknowledging that advancements in engine design and fuel characteristics might render the tests obsolete over time. In late 1933 to early 1934, a program was devised to validate the correlation between road and laboratory knock ratings and to explore avenues for improving the compatibility of fuels and engines [39].

Despite occasional updates in measurement technology, the RON and MON tests have remained largely unchanged. Despite some questioning of their relevance in literature [78], they continue to serve as primary indicators of a fuel's quality today.

#### **4.1.3 Knock intensity measurement principles with RON and MON**

Since knockmeter reading holds paramount importance in determining the RON and MON values, the following section delves into the evolution of knock intensity detection. At first, a bouncing pin sensor was used, positioned flush with the engine's combustion chamber. Upon occurrence of knocking, the pin is propelled upward, thereby closing an electrical circuit, incorporated in a burette containing a solution of 10% sulphuric acid in distilled water. This action triggers the generation of gas within the burette, which accumulates in the graduated arm of a U-tube. The quantity of gas amassed within a specific time frame is contingent upon the frequency and severity of the impacts experienced by the bouncing pin within that duration. The technology evolved in the 1940s into an electronic circuit, utilizing a signal generated by a component known as a detonation pickup. This pickup has undergone minimal changes since its inception and was specifically designed to replicate the signal response of the earlier bouncing pin system. Its purpose was to facilitate the transition away from the bouncing pin mechanism. The pickup includes the pickup face, magnetic body, magnetostrictive rod, coupling coil, and electric terminals. The pickup face interfaces directly with the dynamic pressure environment inside the combustion chamber of the test engine. Meanwhile, the magnetic body generates a stable magnetic field. As pressure fluctuations occur, the magnetostrictive rod experiences compression, causing micro magnetic poles to realign, thereby altering the overall magnetic field. When a coil of wire is positioned within this changing magnetic field,

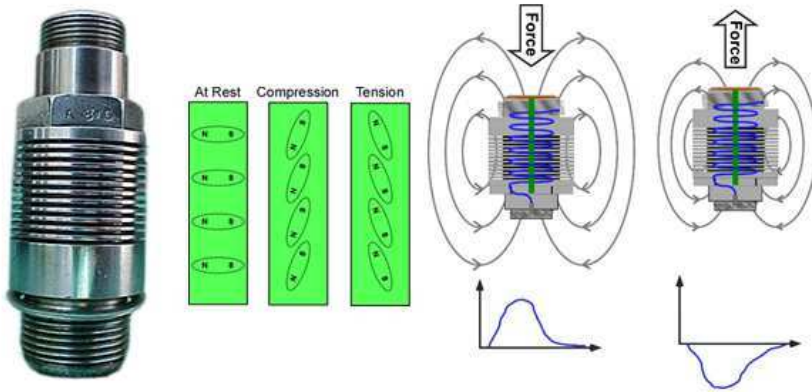


Figure 4.1: The detonation pickup and its working principle, modified from [79].

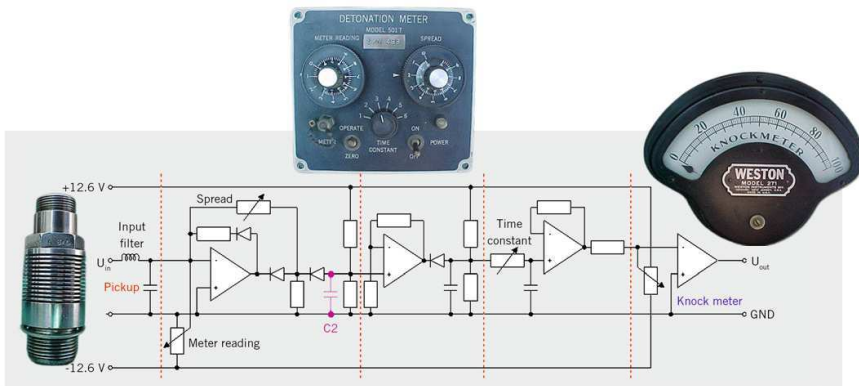


Figure 4.2: The ASTM detonation pickup - detonation meter - knockmeter signal processing setup, modified from [80]

a voltage is induced in the wire coil. Consequently, variations in pressure within the combustion chamber prompt the pickup to produce an electrical signal proportional to the rate of pressure change, as illustrated in Figure 4.1.

In the RON and MON measurement setup as described in ASTM-D2699 and D2700, knock intensity is assessed by analysing the output signal from the detonation pickup, which is named the model D1 sensor. The sensor's signal undergoes processing through a detonation meter, which, in turn, produces a signal for the knockmeter—a display indicating the intensity of knock. The electronics scheme is depicted in Figure 4.2.

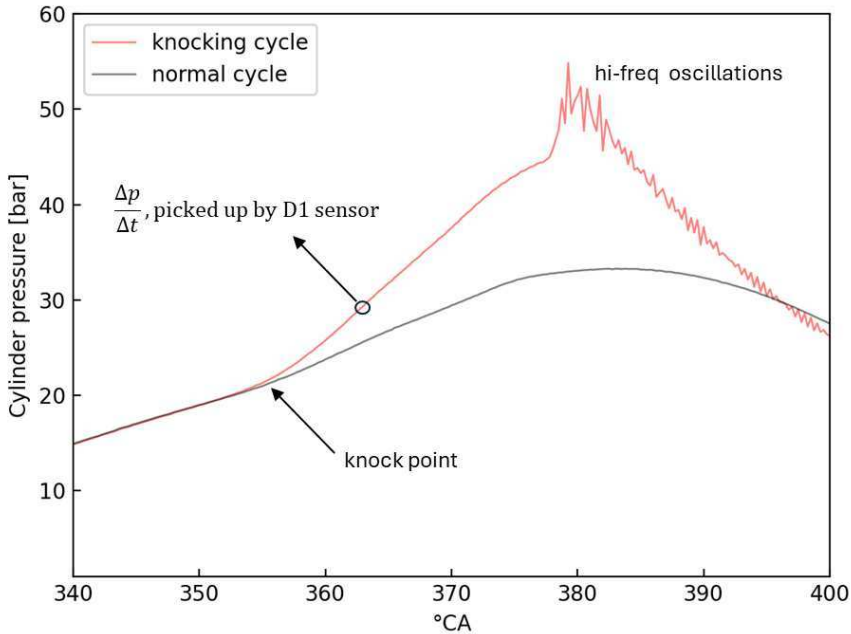


Figure 4.3: Change in pressure ( $\frac{\Delta p}{\Delta t}$ ) during knocking combustion vs normal combustion.

The historic low-frequency character of knock intensity measurement is more or less maintained with this setup since it acts as a low-pass signal filter with a 2.85 kHz limit [78, 80]. It measures ( $\frac{\Delta p}{\Delta t}$ ), the sudden pressure increase at the so-called ‘knock point’ where the cylinder pressure trace bends upwards when knocking combustion occurs, moving away from the normal cylinder pressure trace, as illustrated in Figure 4.3.

In 2010, Waukesha introduced a new digital version of the CFR test measurement system. The introduction of the so-called XCP panels aimed to replace the detonation meter and knockmeter but kept the detonation pickup itself. Therefore, it can be inferred that the integration of digital technology primarily involves digitizing the procedures through digital signal recording, data processing, and control, as discussed in [40, 41, 81]. Figure 4.4 provides a screenshot of an XCP panel where many resemblances can be found with the original detonation meter setup, illustrating that the ASTM knock measurement principle in itself has not changed.

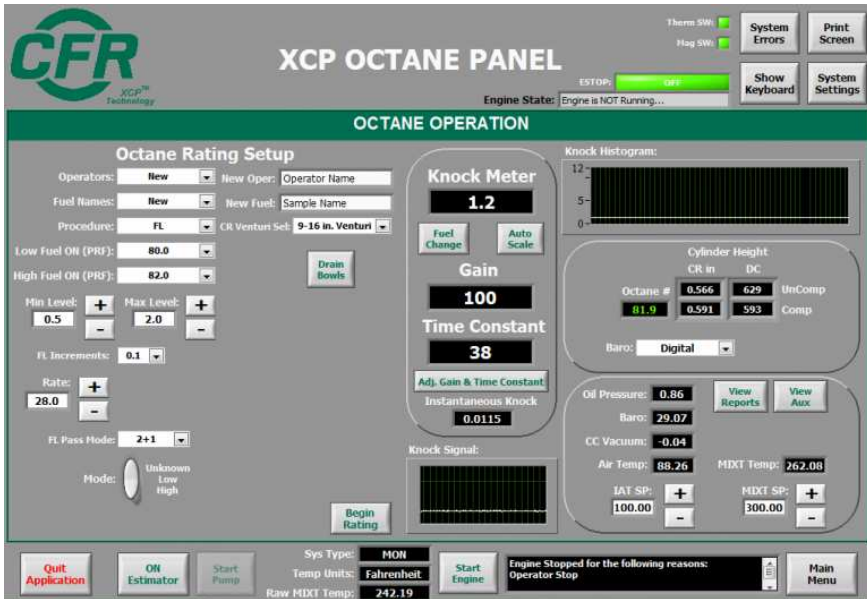


Figure 4.4: The XCP panel technology, still relying on the signal from the D1 detonation pickup [82].

## 4.2 The high-frequency character of knock

Arrigoni was one of the first scientists to investigate the high-frequency aspect of knock in the 1970s [83], and noticed high-frequency pressure oscillations around top dead centre (TDC) when knocking combustion occurred. These oscillations usually occur within a frequency range of 3.5 to 15 kHz and are represented by the pressure spikes in Figure 4.3. Since the RON/MON knock measurement system acts as a signal filter with a cutoff frequency of around 2.85 kHz, the pressure fluctuations  $\Delta P_f$  that occur during knocking combustion are ignored [80, 84].

In a contemporary production SI engine, those high-frequency oscillations cause engine vibrations that are picked up by a so-called knock sensor. The majority of knock sensors are of the accelerometer type, a technology based on piezo-ceramic material, combined with seismic mass, generating a signal to the engine's ECU when the sensor is excited by the high-frequency pressure oscillations — not necessarily the  $\left(\frac{\Delta p}{\Delta t}\right)$  — during knocking combustion. Next to the fact that the D1 pickup system's frequency spectrum is limited to 2.85 kHz, knock sensors are generally mounted on the engine block surface as depicted in Figure 4.5, in contrast to the D1's mounting position, which is mounted flush with the



*Figure 4.5: A production engine knock sensor, mounted on the engine block.*

combustion chamber wall.

Arrigoni's work indicated that there is a good correlation between the knockmeter signal and the high-frequency pressure oscillations, but later work from Yates et al. [85] revealed an inconsistent correlation between the pressure oscillations and the corresponding octane number for the RON and MON reference conditions. The shortcomings of the ASTM RON/MON methodology further become evident in Figure 4.6, which illustrates a knocking combustion cycle of a PRF and a toluene standardization fuel (TSF), both sharing the same RON of 97. Both fuels show the same  $\left(\frac{\Delta p}{\Delta t}\right)$  (identical RON) after the knock point, but feature a different oscillation intensity. In this case, if RON would be associated with this oscillation intensity, the engine's knock sensor would 'measure' another kind of 'RON' than the RON that was measured by the D1 pickup system in the CFR engine.

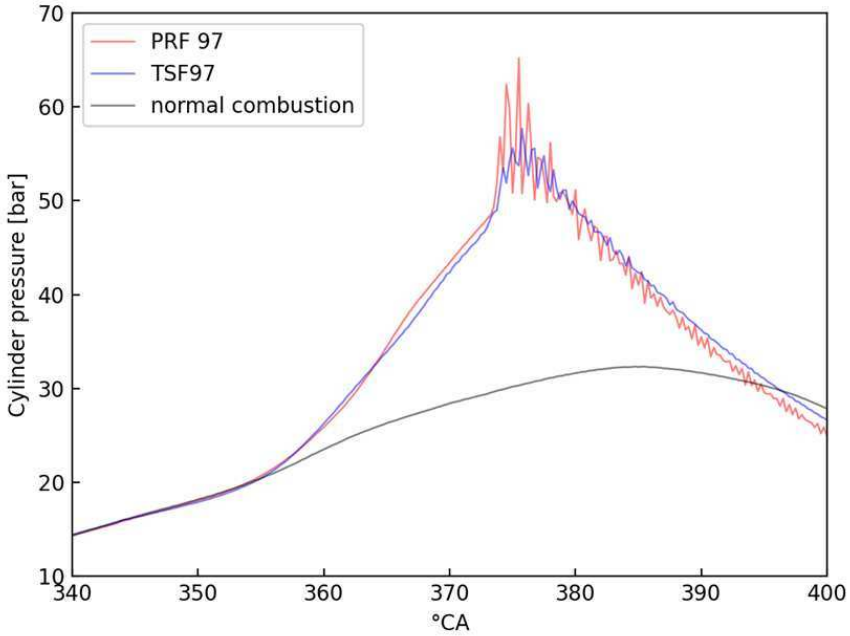


Figure 4.6: Oscillation behaviour of PRF RON 97 and TSF RON 97 for one knocking combustion cycle. Compression ratios are 9.1 for the PRF and 8.6 for the TSF.

The inconsistency between the knock intensity signal from the knock sensor and the conditions used for rating fuels for octane values suggests a potential discrepancy between octane rating and the knock limit typically detected by a modern knock sensor [78]. Additionally, the conditions under which the RON and MON tests are conducted diverge considerably from those found in modern SI engines. The ASTM RON and MON tests still rely on carburetors, use low engine speeds, disregards boosting and do not necessarily operate at stoichiometric conditions, which further supports the argument that RON and MON are not reliable indicators of knock resistance for contemporary engines. In the context of the Ad-Libio development, a novel approach to octane rating was devised. This method hinges on the fuel's oscillation characteristics, aiming to address the historical shortcomings of the ASTM octane rating system. This work introduces a novel approach that addresses the traditionally weak correlation between oscillation intensity and ASTM RON, a step not previously taken. The subsequent sections delve into the background of alternative knock intensity measurement and present the methodology description of an alternative RON measurement method.

## 4.3 Oscillation-based knock intensity

### 4.3.1 Maximum amplitude of pressure oscillations - MAPO

Since the introduction of Arrigoni's work, knock intensity (KI) was redefined in literature in an attempt to better match the phenomenon that is measured by the accelerometer-based knock sensor. Based on a filtered pressure signal where the oscillations are isolated from the cylinder pressure trace, different expressions have been developed to quantify knock intensity. A commonly used KI indicator is the maximum amplitude of pressure oscillations (MAPO), the highest occurring pressure peak in a combustion cycle, as illustrated in Figure 4.7.

However, upon examining consecutive combustion cycles, it becomes evident that there is a weak correlation—if any—between the rate of pressure change ( $\frac{\Delta p}{\Delta t}$ ) at the knock point and the pressure oscillations that ensue from it. Figure 4.7 shows two separate combustion cycles with PRF 98 in the CFR engine. Cycle 1 has a steeper ( $\frac{\Delta p}{\Delta t}$ ) compared to cycle 2, which would lead to higher readings on the ASTM D1 pickup, but it features lower pressure peaks, leading to a lower MAPO-based KI reading. So a steeper ( $\frac{\Delta p}{\Delta t}$ ) does not always lead to higher oscillation pressures.

### 4.3.2 The stochastic nature of knock

Different methods have been applied in the literature to provide quantification metrics of successive knocking combustion cycles, with the running average of MAPO being commonly applied [86]. However, even with a high number of combustion cycles, although the running average may evolve to a stable KI outcome, there is generally a weak correlation between a fuel's octane number and MAPO-based KI quantification [87, 88]. The main reason can be found in the stochastic nature of knock. The MAPO varies with every combustion cycle and if an average value is to be calculated, the outcome is often significantly different when a different section of a measurement run is considered, as illustrated in Figure 4.8, where a different average MAPO is obtained for every 1000 combustion cycles.

The stochastic nature of knock makes it difficult to provide RON or MON quantification on MAPO-based observations or oscillation behaviour in general. Brunt [87] came to the conclusion that a moving averaged smoothing function can be used to calculate KI if a correct sample size and crank angle resolution are

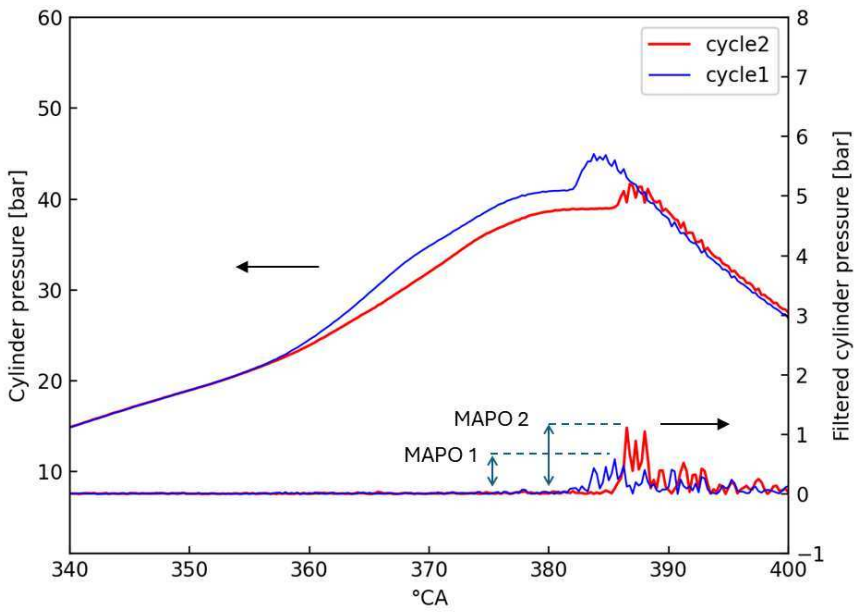


Figure 4.7: Example of successive knocking cycles of RON 98 PRF. Steeper initial pressure curves do not necessarily lead to higher pressure oscillation amplitudes.

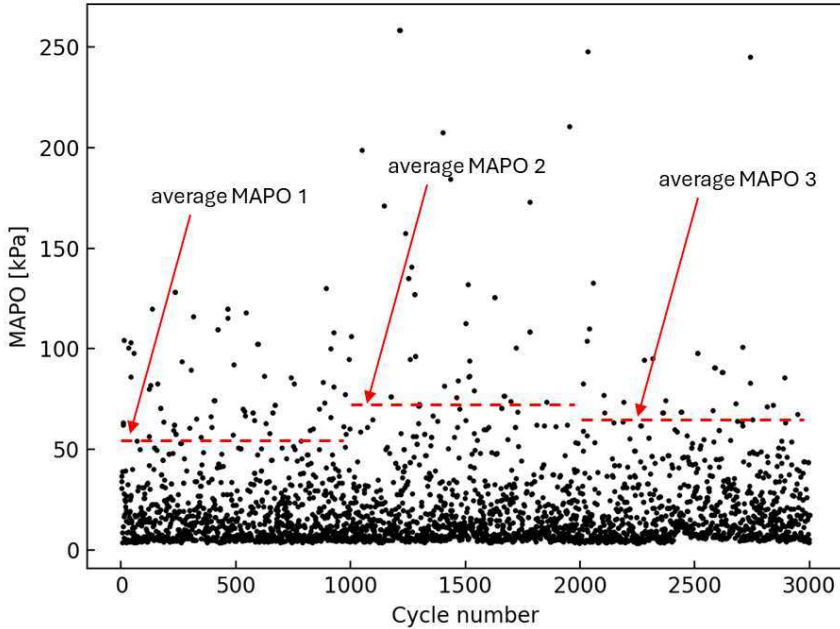


Figure 4.8: MAPO plot of 3000 successive combustion cycles, in this case of iso-octane. Every dot represents one MAPO, demonstrating the stochastic behavior of knock.

used in combination with a pressure transducer with suitable properties, mounted at the correct location. He also concluded that it is impossible to obtain a definitive quantitative measure of knock intensity that could be applied to all engine types [87]. It was noted elsewhere that no clear correlation between the RON/MON rating and pressure oscillations could be found [85, 89]. To overcome this, Yates and Swarts proposed to use the RON/MON method in combination with a new metric called Maximum Amplitude Rating (MAR) to express the severity of the pressure oscillations during knocking combustion [90]. This method combines the classic RON/MON rating with a pressure oscillations behavior assessment, basically performing a standard RON test with the standard ASTM measurement system and combining it with a piezoelectric cylinder pressure sensor to measure the high-frequency pressure fluctuations. The method's better insight in fuel behavior comes at the cost of a more complex measurement system, combining different measurement techniques into one machine. Although KI has been intensively studied in the past and different measurement metrics have been proposed [83, 91, 92], quantifying KI into a fuel's antiknock rating for comparison with RON or MON has not been done until now. This is confirmed by the work

of Rockstroh et al., who investigated a variety of knock metrics and found a rather low correlation coefficient between knockmeter readings and MAPO [88].

In the Ad-Libio framework, the need for an easy and quick octane number quantification method arose since the octane numbers of a large number of different fuel blends, developed with the fuel calculator, needed verification. Relying on an external laboratory to screen different Ad-Libio fuels for ASTM-compliant RON and MON would not only represent a significant financial cost, it would be a time-consuming matter too since quick in-house verifications of subtle fuel composition changes would require significant logistical efforts. Instead, an alternative octane evaluation method was investigated and developed to assess a fuel's knock-resistive properties with a variable-compression-ratio single-cylinder CFR engine, based on knock-induced pressure oscillations instead of the  $\left(\frac{\Delta p}{\Delta t}\right)$ -method prescribed by the ASTM. Implementing this principle effectively would lead to a cost-effective setup, as it requires only standard engine laboratory equipment while providing deeper insights into the oscillation behavior of the novel fuels.

Given the historical lack of correlation between RON and high-frequency pressure oscillation intensity during knock, the following sections of this work analyze the method that is used to effectively address this longstanding issue.

## 4.4 Pressure-oscillation-based octane measurement

### 4.4.1 Measurement setup

The experimental setup is based around a CFR engine, where the original carburetor system is replaced by a port fuel injection system. The D1 pressure pickup sensor is replaced by a Kistler 701A pressure transducer, mounted flush with the cylinder wall. A PID-controlled electrical air heater is mounted in the air intake in front of the fuel injector. The exhaust is equipped with an Innovate LM-2 wideband air/fuel ratio meter (lambda sensor) kit. A crank angle encoder with  $0.25^\circ$  resolution is connected to the crankshaft. The measurement setup is connected to a National Instruments PXI-1050 chassis and a BNC-2120 data acquisition system. The data acquisition setup is controlled by a Labview 2015 program, while the engine spark timing is controlled by a Motec ECU. The setup diagram is depicted in Figure 4.9.

The cylinder pressure trace is stored as a function of crank angle degrees, for a user-defined number of cycles. For each cycle, the pressure trace is then

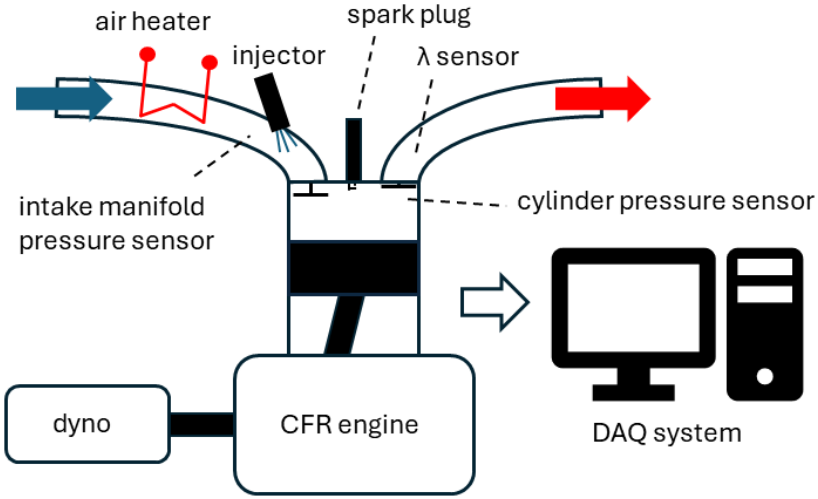


Figure 4.9: Experimental setup.

filtered in a Python script with a 5th-order bandpass Butterworth filter, with cut-off frequencies at 3.5 kHz and 10.8 kHz. This is one order higher than used by Kim et al. [93], to obtain a sharper cutoff at the desired frequencies while still remaining a stable and reliable filter. Huber et al. suggested a bandpass filter between 3.5 and 15 kHz [80] but with a sampling rate of 4 samples per °CA, the higher cutoff frequency cannot be reached due to Nyquist's theorem, which states that sampling should be done at least twice as fast as the maximum frequency of the system. The upper limit of the bandpass filter is defined by Equation 4.1, for an engine speed of 900 rpm, which was the chosen engine speed as explained in the next paragraph.

$$\frac{1}{2} \cdot \frac{900 \text{ rev}}{\text{min}} \cdot \frac{1 \text{ min}}{60 \text{ s}} \cdot 360 \frac{\text{degrees}}{\text{rev}} \cdot 4 \frac{\text{samples}}{\text{degree}} = 10800 \text{ Hz} \quad (4.1)$$

The combination of the measurement setup and the application of the bandpass filter allows to extract the high-frequency pressure oscillations from the cylinder pressure signal. Figure 4.10 shows a typical example of the data that is generated for one combustion cycle.

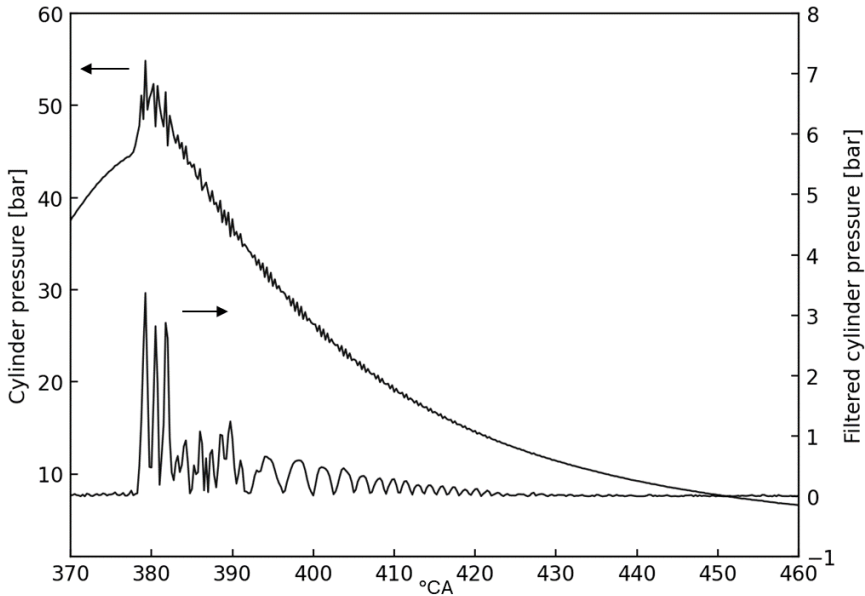


Figure 4.10: cylinder pressure trace with filtered signal.

#### 4.4.2 Engine parameters

Since an alternative for the ASTM RON test is aimed for, the engine parameters were inspired by most of the settings of the traditional test. One significant difference is the engine speed, which is configured to 900 RPM instead of 600. Given that 900 rpm is the CFR's maximum speed, it represents the closest achievable speed to mimic real-world engine speeds. Intake air temperature and ignition timing were selected according to ASTM RON specifications, resulting in the engine setup parameters listed in Table 4.1.

#### 4.4.3 A new knock intensity definition

Knock, being a stochastic phenomenon, is subject to a large cycle-to-cycle variability. In a successive number of cycles, the peak cylinder pressures can vary considerably from cycle to cycle which can create reproducibility problems if KI calculations need to be performed with a limited number of cycles. Figure 4.8 serves as an example, where the KI calculation, defined by the average MAPO of the first 1000 cycles differ from the KI calculated from cycle 1000 to 2000 and are

*Table 4.1: Engine parameters of the test setup*

| <b>Parameter</b>         | <b>Value</b>       | <b>Unit</b> |
|--------------------------|--------------------|-------------|
| Speed (n)                | 900                | rpm         |
| Ignition timing (IT)     | 13                 | °BTDC       |
| Intake air temperature   | 50                 | °C          |
| Sample rate (CA-based)   | every 0.25         | °CA         |
| Sample rate (time-based) | 21.6               | kHz         |
| Equivalence ratio        | 1 (stoichiometric) | -           |

also different from the KI calculated over cycles 2000 to 3000 and so on. When enough cycles are added to the running average, the KI will converge to a certain value, allowing to quantify a fuel's knock-resistive properties. However, too large a number of samples should be avoided to reduce the time and cost of the test, and possibly avoid engine damage.

Instead of the traditional way of averaging every cycle's peak pressure over a large number of cycles, it was investigated whether it was possible to obtain robust information with a minimized sample size with each test run. During an average knocking cycle, the filtered cylinder pressure peak is followed by several pressure peaks of (mostly, but not always) lesser but comparable intensity. Instead of MAPO, the (single) highest pressure peak, indicated as  $p_1$  in Figure 4.11, a multitude of pressure peaks in the same cycle were used. With this method, knock intensity is calculated by averaging the highest pressure oscillation amplitudes, expressed in Equation 4.2, where  $X$  is the number of pressure peaks considered. This new KI is thus defined as the average of the maximum pressure oscillations using  $X$  pressure peaks  $AMPO_X$ .

$$KI_{\text{of 1 cycle}} = AMPO_X = \frac{\sum_{i=1}^X P_i}{X} \quad (4.2)$$

When  $AMPO_X$  is averaged out over a number of combustion cycles, the mean average of maximum pressure oscillations using  $X$  pressure peaks ( $MAMPO_X$ ) can be calculated, expressed in Equation 4.3. The method is called MAMPO, for mean average of maximum pressure oscillations.

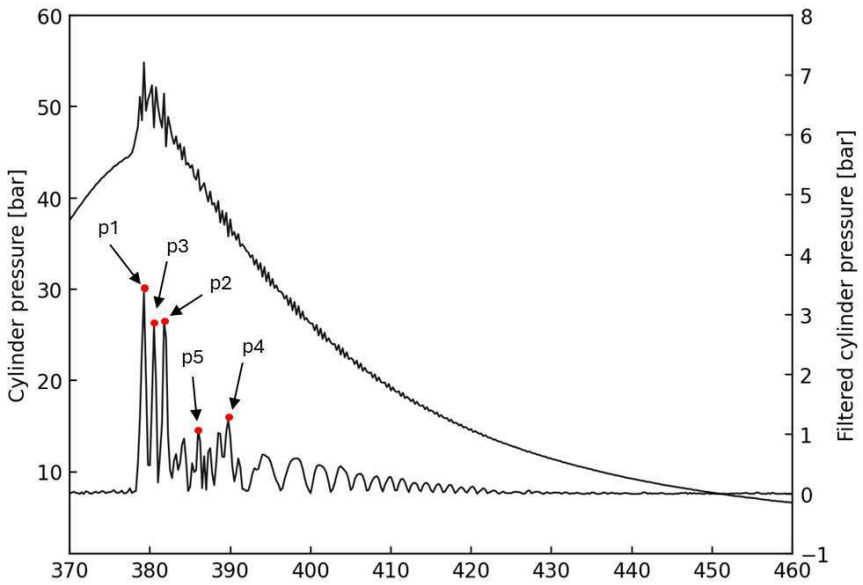


Figure 4.11: A knocking combustion cycle and its corresponding filtered signal, with the five highest amplitudes shown.

$$MAMPO_X = \frac{\sum_{j=1}^{N_{\text{cycles}}} AMPO_{Xj}}{N_{\text{cycles}}} \quad (4.3)$$

#### 4.4.4 Influence of knock intensity and sample size on reproducibility

To further develop the octane rating method, a choice had to be made with regards to:

- The number of pressure peaks  $X$  to calculate  $AMPO_X$ .
- The sample size (number of combustion cycles) with which  $MAMPO_X$  will be calculated.
- The reference  $MAMPO_X$ -based knock intensity value to compare fuels to each other.

The influence of these parameters on the reproducibility of the octane rating test needs to be investigated to determine whether the stochastic nature of knock can be dealt with, leading to consistent and reproducible octane test results. With this in mind, the test setup was employed using E10 gasoline. Two test runs, each consisting of 3000 samples, were conducted: one under light knocking conditions and the other under heavy knocking conditions. Light knock was defined audibly by increasing the compression ratio until knock could be heard, yielding a  $MAMPO_{20}$  value of 10 kPa. Heavy knock was defined by further increasing the compression ratio until a well-pronounced knocking sound could be heard, resulting in a  $MAMPO_{20}$  value of 70 kPa.

Figure 4.12 shows the evolution of  $MAMPO_X$ , in a light knocking combustion situation, for different sample sizes, as a function of the number of pressure peaks ( $X$ ) used. Figure 4.13 shows the same, but in heavy knocking conditions.

A clear descending trend in  $MAMPO_X$  value is observed with an increasing number of pressure peaks ( $X$ ). This is to be expected, since averaging ever smaller pressure peaks in a cycle will reduce its average value. A vertical spread can be observed in the  $MAMPO_1$ ,  $MAMPO_2$ ,  $MAMPO_5$ ,  $MAMPO_{10}$ ,  $MAMPO_{20}$ ,  $MAMPO_{30}$  calculations.

$MAMPO_X$  values obtained with 250 samples clearly differ from those obtained with 500 samples or more in light knocking conditions as shown in Figure

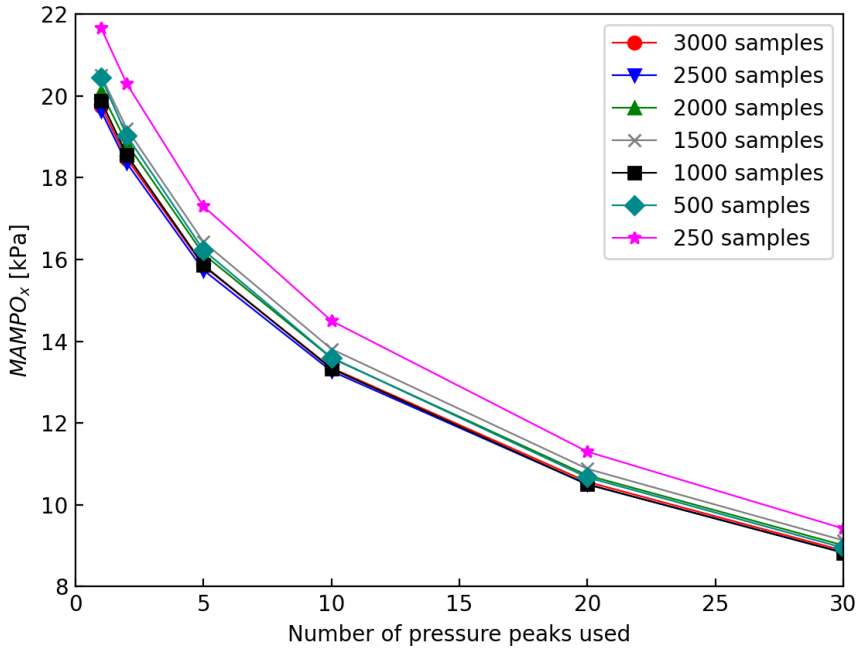


Figure 4.12: MAMPO<sub>x</sub> values as a function of number of pressure peaks per cycle, with different sample sizes, in light knocking conditions.

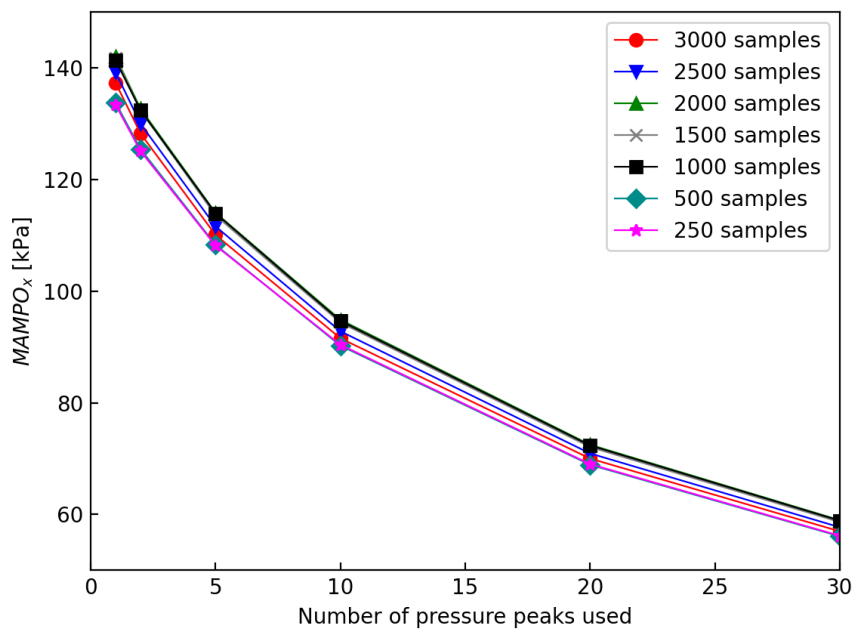


Figure 4.13: MAMPO<sub>X</sub> values as a function of number of pressure peaks per cycle, with different sample sizes, in heavy knocking conditions.

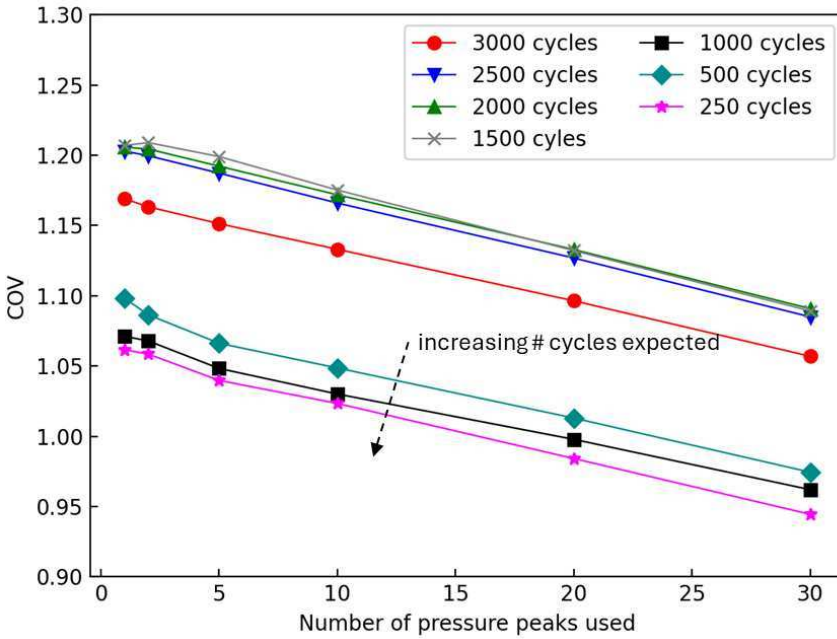


Figure 4.14: COV for different MAMPO<sub>X</sub> values with different sample sizes in light knocking conditions.

4.12. The differences in MAMPO<sub>X</sub> values are less outspoken in heavy knocking conditions as can be seen in Figure 4.13.

For light knock situations, the coefficient of variance, the spread of the KIs of every individual cycle, divided by the average KI of all cycles in the sample, indicated in Equation (4.4), was calculated and plotted in Figures 4.14 and 4.15 as a function of the number of pressure peaks used to calculate MAMPO<sub>X</sub>, with different sample sizes.

$$COV = \frac{\text{Standard deviation of AMPO}_X}{MAMPO_X} \quad (4.4)$$

An interesting observation can be made with the light knock situation in Figure 4.14. The sample size does not necessarily decrease the MAMPO<sub>X</sub> COV, as would be expected. Instead, we see the lowest COV occurring with the smaller sample sizes. It seems that the stochastic nature at light knocking combustion conditions (corresponding to a MAMPO<sub>1</sub>-value of 20 kPa) is pronounced in such a way that a sample size below 1000 cycles cannot be considered as reliable nor reproducible

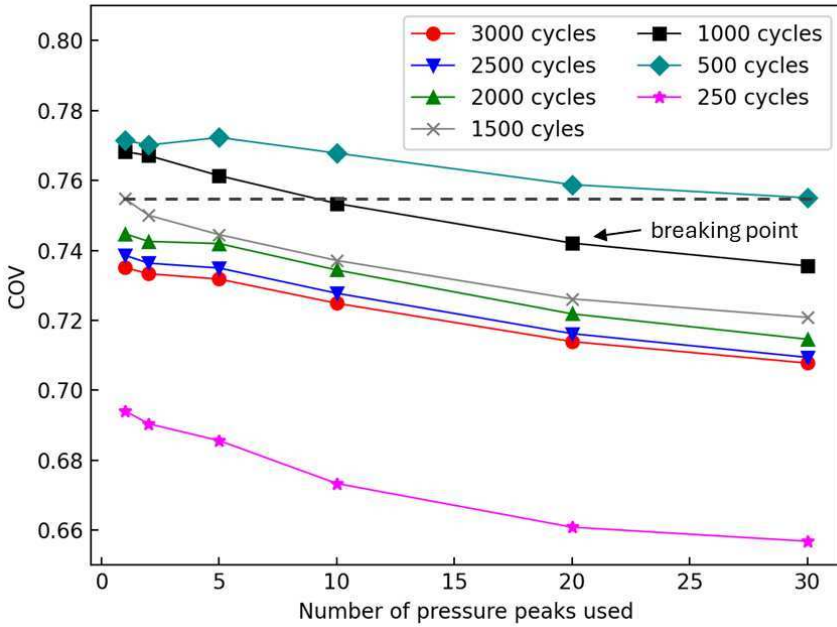


Figure 4.15: COV for different MAMPO<sub>x</sub> values with different sample sizes in heavy knocking conditions.

since it does not contain enough data to be representative, in contrast with a sample size of 1500 cycles or more that shows a consistent behavior. Although increasing the number of pressure peaks has a positive effect on COV, it does not remedy the unreliability of the MAMPO<sub>x</sub> result with sample sizes of 1000 or less.

A different conclusion can be made when knock intensity is increased. Looking at the graph in Figure 4.15, a lower COV than in the light knock case can be observed, independent of the number of samples or the number of pressure peaks used. Still, an anomaly can be seen since the lowest COV value is obtained with the lowest sample size of 250 samples, leading to the conclusion that this sample size is too small to produce reliable results. Also, a clear effect on COV value is noticeable when the MAMPO<sub>x</sub> value is calculated with an increasing number of pressure peaks. The horizontal dashed line indicates that the COV of the combination MAMPO<sub>1</sub>/1500 cycles is equal to the COV of MAMPO<sub>10</sub>/1000 cycles or the COV of MAMPO<sub>30</sub>/500 cycles. In the same way, the same COV as MAMPO<sub>1</sub>/3000 cycles could be obtained with MAMPO<sub>10</sub>/1500 or MAMPO<sub>30</sub>/1000 cycles in Figure 4.15. To conclude the cycle-to-cycle variability analysis, it can be stated that a higher knock intensity has a positive impact on the reproducibility of knock intensity calculations and that the MAMPO<sub>x</sub> method of KI calculation further

decreases the COV with an increasing number of pressure peaks used.

#### 4.4.5 The choice of MAMPO<sub>20</sub> test parameters

Finally, a choice needs to be made with regards to knock intensity, sample size and number of pressure peaks. Although fewer samples generate a higher COV, absolute priority is given to the economical use of sample fuels, so 500 samples are chosen as the target sample size for reproducible results. More samples can be taken if enough sample fuel is available, fewer samples would lead to unreproducible results. The choice on the number of pressure peaks is a compromise. A low number of pressure peaks leads to a high COV, a high number of pressure peaks potentially leads to insensitivity between calculated KIs of different fuels. For fear of averaging too many pressure peaks, leading to a loss in sensitivity of the MAMPO<sub>X</sub> calculation, using 30 pressure peaks or more was discarded. For the chosen sample number of 500, a number of pressure peaks inferior to 10 does not represent a downward trend in the curve on Figure 4.15 and was therefore also not retained. The COV of 500 samples with a MAMPO<sub>20</sub> value of 40 kPa was measured with E10 gasoline and was found to be 1.19. No significant difference with the COV of MAMPO<sub>10</sub> could be found, so either 10 or 20 pressure peaks would qualify but given the limited sample size, the highest number of pressure peaks, 20, was retained. This value corresponds to a slight breaking point in the COV curve, indicated in Figure 4.15 after which the downward trend in the variability of the test results becomes less outspoken. With the resulting MAMPO-based octane rating method, the engine's compression ratio (CR) is adapted until a targeted MAMPO<sub>20</sub> value is obtained. The CR at which this value is reached is then considered to be a measure for the knock-resistant property of the fuel. To define this targeted value, the previously discussed heavy knock intensity with a MAMPO<sub>20</sub> value of 70 kPa was considered, but this generates knocking occurrences that are too severe for the measuring equipment to sustain for extended periods of operation. Therefore, the average value between the discussed light (10 kPa) and heavy (70 kPa) knock situations was chosen, leading to a target MAMPO<sub>20</sub> of 40 kPa. This knocking intensity was clearly audible with the test setup, making it easier for the operator to initially adjust the engine's compression ratio without overly stressing the measuring equipment. The final parameters for the MAMPO<sub>20</sub> calculation are summarized in Table 4.2.

*Table 4.2: Combined engine and knock parameter settings*

| <b>Engine Parameters</b>                    |               |                  |
|---|---------------|------------------|
| <b>Parameter</b>                            | <b>Value</b>  | <b>Unit</b>      |
| Speed (n)                                   | 900           | rpm              |
| Ignition timing (IT)                        | 13            | °BTDC            |
| Intake air temperature                      | 50            | °C               |
| Sample rate (CA-based)                      | every 0.25    | °CA              |
| Sample rate (time-based)                    | 21.6          | kHz              |
| Equivalence ratio                           | 1             | (stoichiometric) |
| <b>Data Parameters</b>                      |               |                  |
| <b>Parameter</b>                            | <b>Value</b>  | <b>Unit</b>      |
| Number of samples                           | 500 (minimum) | -                |
| Number of pressure peaks for averaging AMPO | 20            | -                |
| MAMPO <sub>20</sub> target value            | 40            | kPa              |

## 4.5 System calibration with primary reference fuels

In order to test whether a correlation can be found between octane number and MAMPO<sub>20</sub>, 11 different primary reference fuels (PRFs) were synthesized, starting from ON 90 to ON 100 in steps of 1 ON unit. Lower octane numbers were not considered.

Each fuel was tested with the bracketing method in the CFR engine, with the engine settings of Table 4.2 applied. The engine's compression ratio was set to obtain a MAMPO<sub>20</sub> value slightly below and slightly above 40 kPa. Linear interpolation was used to obtain a calculated compression ratio at which MAMPO<sub>20</sub> would be 40 kPa for that specific PRF. The results are plotted in Figure 4.16.

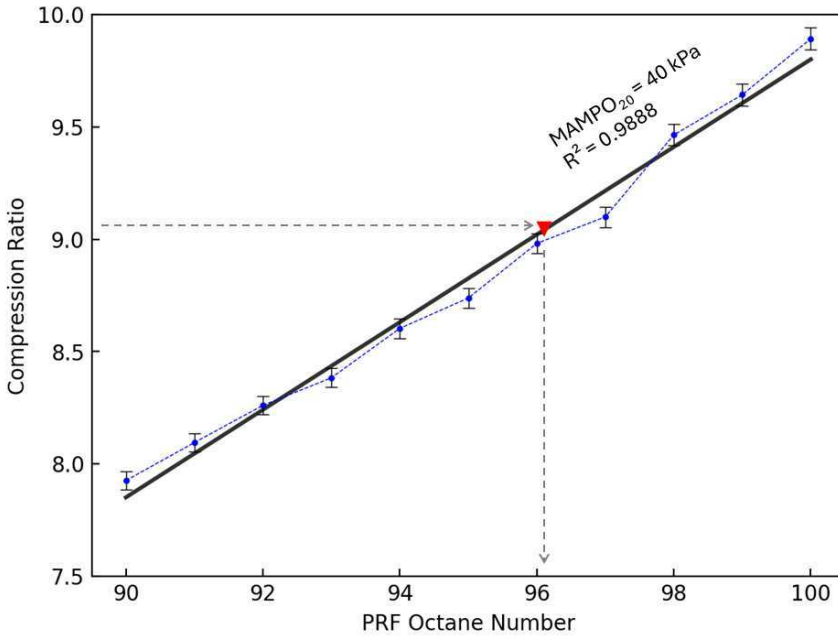


Figure 4.16: Compression ratio as a function of PRF octane number for MAMPO<sub>20</sub> KI of 40 kPa

The interpolated compression ratio needed to obtain a MAMPO<sub>20</sub> of 40 kPa was found to show a clear linear behavior as a function of PRF-based octane number with an  $R^2$  value of 0.9888. Given the linear relationship between CR and RON, a linear regression model was fitted to the data which is described by Equation 4.5.

$$MAMPO_{20} \text{ RON} = 50.22 + 5.07 \cdot CR \quad (4.5)$$

It seems that, by applying the MAMPO<sub>20</sub> methodology, the stochastic nature of knock is harnessed and the traditional weak correlation between pressure oscillations and RON is solved.

A sample fuel can thus be subjected to the MAMPO<sub>20</sub> RON test by obtaining a KI slightly above 40 kPa and slightly below. The compression ratio (CR) required to achieve a knock intensity (KI) of exactly 40 kPa can then be calculated. Equation 4.5 is then used to determine the RON number, renamed MAMPO<sub>20</sub>-RON to reflect the method of RON measurement. The uncertainty of the thus obtained RON value is discussed in the next section.

## 4.6 Sensitivity analysis

Upon observation of Equation 4.5 is followed, it is clear that the error on the measured MAMPO<sub>20</sub> ON is directly related to the error on the CR, set to obtain a MAMPO<sub>20</sub> of 40 kPa. Different parameters, known to affect the auto-ignition behavior, are considered:

- variations in air temperature
- air-to-fuel ratio ( $\lambda$ )
- ignition timing
- errors in PRF blend composition
- resolution of the pressure sensors

The error on the setting of the compression ratio is assumed to be derived from the cylinder head position gauge of the CFR, that can be read with an accuracy of  $\pm 0.01$ . The absolute error (AE) on the compression ratio setting was calculated by master thesis students Van Biesen and Demeersseman [94], based on the relationship between micrometer reading and the CFR's compression ratio, featuring an average slope of 1.09 between gauge position 35 and 37 as indicated in Figure 4.17, resulting in an AE on the CR of  $\pm 0.011$ .

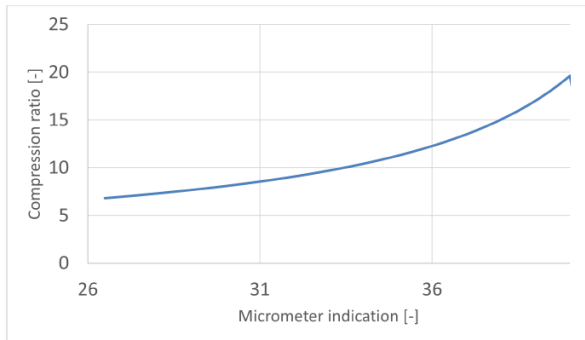


Figure 4.17: CFR compression ratio as a function of micrometer indication.

The in-cylinder pressure sensor measures the relative cylinder pressure in relation to the absolute inlet pressure. Both sensors have a relative error (RE) of 0.5%. The relative in-cylinder pressure is thus measured with a total RE of  $\pm 1\%$ . It

is assumed that the digital Butterworth filter which is applied to the pressure trace does not influence the error, meaning that the error of 1% is transported throughout the entire calculation of AMPO and MAMPO. For the targeted value of 40 kPa, this means an absolute error (AE) of 0.4 kPa. Since the average value of 20 pressure peaks is calculated, the AE on the result adds up to 8 kPa and must be divided by 20, keeping the AE at 0.4 kPa. To define the influence of 0.4 kPa difference on the CR, the case of PRF 95 was taken, where MAMPO<sub>20</sub> was measured at two different compression ratios, as listed in Table 4.3.

Table 4.3: CR-MAMPO<sub>20</sub> relationship for PRF 95

| CR          | MAMPO <sub>20</sub> (kPa)          |
|-------------|------------------------------------|
| 8.725       | 49.1                               |
| 8.809       | 64.8                               |
| $\Delta$ CR | $\Delta$ MAMPO <sub>20</sub> (kPa) |
| 0.002       | 0.4                                |

The rule of three has been applied to calculate the difference in compression ratio as a consequence of the 0.4 kPa error in MAMPO<sub>20</sub> calculation. Combined with the previously defined AE on the CR of 0.011, the total CR error is hence 0.013 and when applied to Equation 4.5, an error of  $\pm 0.066$  in MAMPO<sub>20</sub>-RON can be applied. This can be rounded off to 0.1 MAMPO<sub>20</sub>-RON for simplicity reasons. The ignition timing error, being fixed at 13° BTDC at all times, is defined by the upward ramp signal of a hall effect sensor in the engine's ignition system and is considered to be nil. All PRF blends were produced in-house using a graduated cylinder with 1 ml divisions and were produced in batches of 11. For the PRF of RON 95, the AE on the RON of the calibration PRF was therefore calculated as being 0.095 and this error was maintained throughout all calibration PRFs. No significant relation was found between a 10°C span of intake air and the obtained MAMPO<sub>20</sub>-RON value and the error therefore is considered nil, given the fact that the intake air temperature is PID-controlled and intake air temperature variations are considered below 2°C. From literature, it is clear that a significant relation does exist between  $\lambda$ -value and MAMPO<sub>20</sub>-RON. Measurements of the same E10 fuel batch were taken on both sides of stoichiometric combustion conditions and the resulting derived octane numbers are listed in Table 4.4. To define the MAMPO<sub>20</sub>-RON error, the worst case of 10% increase in  $\lambda$  resulting in a 2.22% increase in calculated MAMPO<sub>20</sub>-RON was taken into consideration. Given that the AE on the  $\lambda$ -value is 0.01 as defined by the air-fuel ratio measurement system, (a RE of 1% at  $\lambda = 1$ ), the RE on the MAMPO<sub>20</sub>-RON that would be caused by

*Table 4.4: Influence of lambda on derived MAMPO<sub>20</sub> ON of gasoline E10.*

| $\lambda$ Measured | $\lambda$ Deviation | MAMPO <sub>20</sub> -RON | MAMPO <sub>20</sub> -RON Deviation |
|--------------------|---------------------|--------------------------|------------------------------------|
| 0.90               | -10%                | 96.35                    | 0.61%                              |
| 0.95               | -5%                 | 96.05                    | 0.29%                              |
| 1.00               | 0%                  | 95.77                    | 0.00%                              |
| 1.05               | 5%                  | 96.72                    | 0.99%                              |
| 1.10               | 10%                 | 97.90                    | 2.22%                              |

an error in  $\lambda$  is 0.222%, for a RON 95 fuel leading to an absolute error of 0.21 MAMPO<sub>20</sub>-RON.

The total combined error, caused by  $\lambda$  and CR uncertainties on the MAMPO<sub>20</sub>-RON measurement is therefore estimated at  $\pm 0.3$  MAMPO<sub>20</sub>-RON. This relatively small error seems to be confirmed by the high  $R^2$ -value of the regression model of Equation 4.5 and falls within the  $\pm 0.3$  rating tolerance from the ASTM procedure [40]. Since these results are based on a set of assumptions, an experimental error analysis based on standard deviation measurements is performed in a later stage and described in section 5.3.

## 4.7 MAMPO<sub>20</sub> verification measurements

In a first verification step, the MAMPO<sub>20</sub> method was used to test two commercially available gasoline fuels, E10 (RON 95), E5 (RON 98) and the Ad-Libio blend, which was previously tested for ASTM-RON in section 3.4.1. The results are listed in Table 4.5

*Table 4.5: Comparison of RON and MAMPO<sub>20</sub> RON of different fuels.*

| Fuel                     | ASTM RON | MAMPO <sub>20</sub> RON | Difference |
|--------------------------|----------|-------------------------|------------|
| E10                      | 95       | 93.3                    | 1.7        |
| E5                       | 98       | 96.6                    | 1.4        |
| Ad-Libio (final version) | 96.2     | 95.1                    | 1.1        |

A noticeable difference in octane number quantification can be noted between the ASTM RON and MAMPO<sub>20</sub> RON method, that falls out of the uncertainty limit discussed in the previous section. The MAMPO<sub>20</sub> method assigns lower RON values to the fuels when compared to the ASTM method.

This difference can be explained by the difference in how RON is measured in the ASTM and MAMPO<sub>20</sub> method. The measurement result obtained with ASTM's D1 pickup does not necessarily correlate with the high-frequency oscillations that are measured in the MAMPO<sub>20</sub> setup.

However, it is a known fact that PRFs do not represent the behaviour of modern-day gasoline fuels, that contain more than linear or branched paraffins. Since up to 50% of an actual gasoline is made out of fuels that are neither linear nor branched paraffins, other non-paraffinic compounds are necessary to replace or complement PRF mixtures. The most widely used surrogate is toluene, leading to the introduction of the so-called toluene standardization fuels (TSFs) [45]. The oscillation behavior of TSFs seems to more closely represent that of gasolines and other fuels with non-paraffinic compounds. In the next chapter, measurements are performed to determine whether the accuracy of the MAMPO<sub>20</sub> RON method can be improved by changing the reference fuels.

## 4.8 Chapter conclusion

With the introduction of the MAMPO method, a new method was devised to investigate the RON of a sample fuel. The method is based on measuring pressure oscillations during knock events. Historically, no correlation could be found between a fuel's RON and the high-frequency pressure oscillations during knock due to the stochastic nature of the MAPO-based knock intensity. By introducing the MAMPO<sub>20</sub> methodology, this stochastic nature is dealt with, leading to a very high correlation between RON and MAMPO<sub>20</sub> knock intensity.

Despite the high correlation, it was found that the knocking oscillation behavior of PRFs does not correspond to the behavior of fuels containing compounds other than paraffinic ones. This leads to an offset in MAMPO<sub>20</sub>-derived RON values compared to the ASTM RON values.

While the difference between ASTM RON and MAMPO<sub>20</sub>-RON results is small enough for ballpark estimations of experimental fuel blends, as seen with the Ad-Libio blend, it is too high to ensure accurate RON results. Therefore, a revision of the method with regards to reference fuels is necessary, which will be discussed in the next chapter.

# 5

## Pressure-oscillation-based octane quantification with toluene standardization fuels

Building on the conclusions of the previous chapter, where an alternative octane measurement approach was developed and proved to be insufficiently accurate for contemporary gasolines, an attempt is made to increase the accuracy by using toluene standardization fuels (TSFs) instead of PRFs. Consequently, the effectiveness of this alternative method was evaluated beyond the conventional RON 100, a threshold traditionally difficult to achieve accurately using the ASTM method.

## 5.1 Octane Sensitivity and the need for toluene standardization fuels

The fact that PRFs no longer accurately represent modern-day gasoline fuels is not new and is related to a different behavior of linear and branched paraffinic fuels (such as PRFs) and, on the other hand, other chemical families that nowadays account for about half the content of an actual gasoline [95].

The need for better reference fuels originates in the difference between a fuel's RON and MON, defined as octane sensitivity (S), expressed in Chapter 2 by Equation 2.2.

Typically, contemporary gasoline will exhibit a higher RON compared to its MON counterpart, leading to a positive octane sensitivity value. The rationale behind this phenomenon relates to the presence of a 'negative temperature coefficient' (NTC) region in the ignition delay curves of paraffinic fuels, including primary reference fuels. This characteristic implies that paraffinic fuels exhibit greater resistance to auto-ignition at the temperatures and pressures typical of the MON test compared to real-world fuels. Actual gasoline compositions consist of a blend of n-, i-, and cyclo-paraffins, olefins, and aromatics. Unlike paraffinic compounds, olefins, and aromatics generally lack a pronounced NTC region, if present at all. Consequently, during the MON test, paraffinic fuels demonstrate increased resistance to auto-ignition, resulting in higher MON values [95].

The recognition of octane sensitivity in actual gasoline holds significant implications for current engine technologies. There is compelling evidence suggesting that with the increasing adoption of boosted (turbocharged) and downsized engines, the fuel's true resistance to auto-ignition transitions from being solely determined by its RON or MON. To this end, another parameter called the Octane Index (OI) was devised [96]. The Octane Index is defined by the equation  $OI = RON - KS$ , where K is a constant influenced solely by the engine conditions. In the work by Kalghatgi et al. [96], a number of modern light-duty engines were tested, and K has been found to be negative in many cases. This means that a fuel with high sensitivity can exhibit an Octane Index higher than its RON value. Subsequently, if K is known for a specific engine and load point, it can be compared with the octane requirement (OR) of the engine, which is defined as the minimum octane index required for the engine's ECU not to perform its knock-limiting algorithms.

Arguably, this method theoretically offers a solution for the outdated RON and MON indications. However, it relies on knowing the K-factor of a specific engine,

*Table 5.1: The complete ASTM-accepted toluene standardization fuel list*

| TSF Blend RON | Rating Tolerance | TSF Blend Composition, vol % |           |           |
|---------------|------------------|------------------------------|-----------|-----------|
|               |                  | toluene                      | isooctane | n-heptane |
| 65.1          | ± 0.6            | 50                           | 0         | 50        |
| 75.6          | ± 0.5            | 58                           | 0         | 42        |
| 85.2          | ± 0.4            | 66                           | 0         | 34        |
| 89.3          | ± 0.3            | 70                           | 0         | 30        |
| 93.4          | ± 0.3            | 74                           | 0         | 26        |
| 96.9          | ± 0.3            | 74                           | 5         | 21        |
| 99.8          | ± 0.3            | 74                           | 10        | 16        |
| 103.3         | ± 0.9            | 74                           | 15        | 11        |
| 107.6         | ± 1.4            | 74                           | 20        | 6         |
| 113.0         | ± 1.7            | 74                           | 26        | 0         |

which can vary depending on factors such as the engine’s load point or atmospheric conditions. Additionally, it is important to note that the knock-limiting algorithm relies on the engine’s knock sensor, which operates using different technology than the D1 pressure pickup used in the RON and MON tests.

Octane sensitivity research leads to an emerging need for simple surrogate fuels, that exhibit a sensitivity behavior similar to gasoline. The most widely used surrogate type with a non-paraffinic compound are mixtures of isooctane, n-heptane and toluene, called toluene reference fuels (TRFs) or toluene standardization fuels (TSFs) [97]. Since TSFs more accurately reflect the behaviour of the aromatic components found in real gasoline fuels [98–100], it has led in the past to an amendment of the ASTM RON test method, which since then includes a ‘fit for use’ test using TSFs with accepted reference value (ARV) RONs [101] ranging from 65.1 RON to 113.0 RON, as depicted in Table 5.1.

It is worth noting that, in addition to similar octane sensitivity behavior as gasoline, TSFs also demonstrate comparable oscillation behavior during knock [102]. To explore potential improvements to the MAMPO method, outlined in the previous section, several TSFs were selected and tested under the same operating conditions as the PRF-based MAMPO method, as listed in Table 4.2. TSFs with a RON lower than 89.3 were excluded from consideration. The selected TSFs are provided in

Table 5.2: Toluene standardization fuel list used to recalibrate the MAMPO RON method.

| TSF Blend<br>RON | Rating<br>Tolerance | TSF Blend Composition, vol % |           |           | Compression ratio<br>for MAMPO <sub>20</sub> |
|------------------|---------------------|------------------------------|-----------|-----------|--|
|                  |                     | toluene                      | isooctane | n-heptane |  |
| 89.3             | ± 0.3               | 70                           | 0         | 30        | 7.61   |
| 93.4             | ± 0.3               | 74                           | 0         | 26        | 8.06   |
| 96.9             | ± 0.3               | 74                           | 5         | 21        | 8.63   |
| 99.8             | ± 0.3               | 74                           | 10        | 16        | 9.23   |
| 103.3            | ± 0.9               | 74                           | 15        | 11        | 10.06  |
| 107.6            | ± 1.4               | 74                           | 20        | 6         | 10.99  |
| 113.0            | ± 1.7               | 74                           | 26        | 0         | 12.00  |

Table 5.2.

## 5.2 MAMPO method with TSFs

In accordance with the methodology that was used with PRFs, all TSFs were subjected to knocking combustion with a MAMPO<sub>20</sub> intensity slightly above and below 40 kPa. Table 5.2 lists the interpolated compression ratios for which all TSFs would be knocking with a MAMPO<sub>20</sub> intensity of 40 kPa. Similar to the PRF scenario, a linear relationship was observed between the TSF's octane number and the compression ratio needed to obtain a 40 kPa MAMPO<sub>20</sub> knocking intensity. The  $R^2$  value of the regression line was found to be 0.9903, better than in the PRF case. The thus obtained TSF-based RON estimation can be expressed by Equation 5.1.

$$\text{TSF-based MAMPO}_{20} \text{ RON estimation} = 51.78 + 5.12 \cdot \text{CR} \quad (5.1)$$

For clarity and to distinguish from the PRF-based method, the TSF-based MAMPO<sub>20</sub> will, from now on, be indicated as MAMPO<sub>20T</sub>, where T stands for 'TSF-based'. The regression line of the TSFs is juxtaposed with that of the PRFs in Figure 5.1, with the earlier compression ratio measurements for E10, Ad-Libio and E5 highlighted on the graph. The significant deviation of the TSF

measurements from the TSF regression line can be attributed to the inclusion of three measurements above RON 100 in the regression, which, although utilized for the analysis, are not visible on the chart.

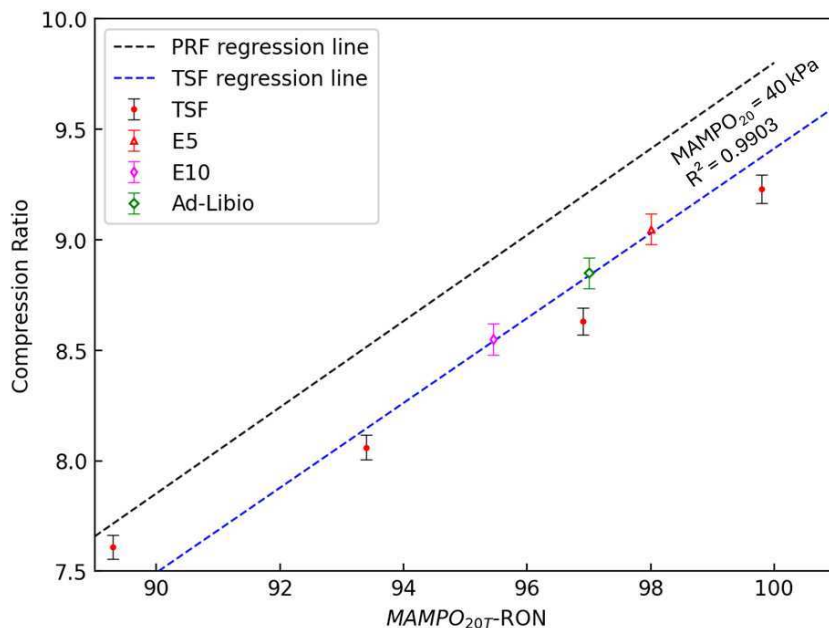


Figure 5.1: Compression ratios for RON 95 and RON 98 gasoline to obtain MAMPO<sub>20T</sub> KI of 40 kPa.

One can note that the offset between ASTM RON and MAMPO<sub>20T</sub> RON is noticeably smaller for both gasoline types compared to the case when PRFs are used as a reference. Table 5.3 gives a comparative overview.

Table 5.3: Differences between PRF- and TSF-based MAMPO<sub>20</sub> RON estimations

| Sample Fuel | ASTM RON | MAMPO <sub>20</sub> RON | Difference | MAMPO <sub>20T</sub> RON | Difference |
|-------------|----------|-------------------------|------------|--------------------------|------------|
| E10         | 95       | 93.3                    | -1.7       | 95.5                     | +0.5       |
| Ad-Libio    | 96.2     | 95.1                    | -1.1       | 97.0                     | +0.8       |
| E5          | 98       | 96.6                    | -1.4       | 98.1                     | +0.1       |

The smaller differences between ASTM RON and MAMPO<sub>20T</sub> RON seem to confirm the fact that TSFs better represent the oscillation behaviour of gasoline and

that better RON estimations can be made, based on oscillation behaviour during knock, with the MAMPO<sub>20T</sub> method compared to the PRF-based method. The experimental uncertainty limits of  $\pm 0.3$  RON, as was calculated in the sensitivity analysis of section 4.6, seems to be on the optimistic side. Assuming an uncertainty value of  $\pm 0.3$  on the ASTM RON number of 96.2 for Ad-Libio, the upper value of 96.5 (96.2+0.3) does not meet the lower value of the MAMPO<sub>20T</sub> result, being 96.7 (97.0-0.3). The RON numbers of E10 and E5 are suspected not to be exactly 95 and 98, both being pump-grade gasolines. A secondary verification is therefore necessary, explained in the next section.

### 5.3 Accuracy verification through standard deviation measurements

To evaluate the precision of the MAMPO<sub>20T</sub> method, confidence intervals (CIs) for the obtained MAMPO<sub>20T</sub> RON and CR values were examined. To this goal, the standard deviations of MAMPO<sub>20T</sub> RON and CR values are determined as follows: initially, 15 tests are conducted at a consistent CR, yielding MAMPO<sub>20</sub> values slightly below 40 kPa. Likewise, an equal number of tests are performed at another constant CR, resulting in MAMPO<sub>20</sub> values slightly above 40 kPa. The experimental results, conducted by master thesis students Decuyper and De Rudder, with E5 and at three different days, are summarized in Table 5.4.

Following this, every trial performed at a lower compression ratio (CR) is matched with a trial at a higher CR, allowing for interpolation to a MAMPO value of 40 kPa. This method yields  $15^2 = 225$  distinct pairs for which the CR corresponding to a MAMPO value of 40 kPa is determined via interpolation. These compression ratios are then applied to calculate the MAMPO<sub>20T</sub>-RON using Equation 5.1. Once all MAMPO<sub>20T</sub>-RON values and CRs for each pair are determined, the standard deviation for MAMPO<sub>20T</sub>-RON values and corresponding CRs can be computed using Equations 5.2 and 5.3.

$$\bar{x}_N = \frac{1}{N} \sum_{i=1}^N x_i \quad (5.2)$$

$$\sigma = \sqrt{\frac{1}{N} \sum_{i=1}^N (\bar{x}_N - x_i)^2} \quad (5.3)$$

In this context,  $\bar{x}_N$  denotes the mean RON and mean CR within a pair, while  $\sigma$  represents the standard deviation of the experimental group. With the standard

Table 5.4: Conducted experiments to determine MAMPO<sub>20T</sub> standard deviation with E5

| E5     | MAMPO at<br>CR = 9.01 (kPa) | MAMPO at<br>CR = 9.07 (kPa) | MAMPO at<br>CR = 9.01 (kPa) | MAMPO at<br>CR = 9.07 (kPa) |
|--------|-----------------------------|-----------------------------|-----------------------------|-----------------------------|
| Test 1 | 34.07                       | 49.18                       | Test 9                      | 32.77                       |
| Test 2 | 32.87                       | 46.28                       | Test 10                     | 39.26                       |
| Test 3 | 32.78                       | 41.99                       | Test 11                     | 36.49                       |
| Test 4 | 34.34                       | 45.88                       | Test 12                     | 35.35                       |
| Test 5 | 34.84                       | 41.85                       | Test 13                     | 38.47                       |
| Test 6 | 37.86                       | 45.26                       | Test 14                     | 34.13                       |
| Test 7 | 38.59                       | 44.36                       | Test 15                     | 39.23                       |
| Test 8 | 32.86                       | 46.01                       |                             |                             |

Table 5.5: Experimental error on the MAMPO<sub>20T</sub> RON test for E5

| E5                      | RON          | CR            |
|-------------------------|--------------|---------------|
| Mean value              | 98.12        | 9.043         |
| Standard deviation      | 0.082        | 0.016         |
| 95% confidence interval | 98.12 ± 0.16 | 9.043 ± 0.031 |
| 99% confidence interval | 98.12 ± 0.21 | 9.043 ± 0.041 |

deviation determined, confidence intervals (CI) can be established using Equation 5.4 and Equation 5.5, which correspond to 95% and 99% confidence levels, respectively.

$$95\% \text{ CI} = [\bar{x}_N \pm 1.96 \cdot \sigma] \quad (5.4)$$

$$99\% \text{ CI} = [\bar{x}_N \pm 2.58 \cdot \sigma] \quad (5.5)$$

The results, presented in Table 5.5, confirm the high repeatability of the MAMPO<sub>20T</sub> method for RON measurement: a rating tolerance of 0.2 with is completely in line with, or even exceeds, the ASTM octane rating tolerance of ± 0.3 for octane numbers up to RON 100 [40]

## 5.4 Conclusions for RON up to 100

The MAMPO<sub>20T</sub> method exhibits a strong correlation between the ASTM RON scale and oscillation behaviour during knock and shows a significant improvement over the historically weak correlations between AMPO and RON in the literature for PRFs and TSFs alike.

Due to the distinct differences in the oscillation behavior between PRFs and TSFs, an observable offset emerges between their respective regression lines. This discrepancy arises from variations in their response to knocking pressure oscillations. While TSFs exhibit a closer resemblance to the oscillation behavior found in real-world gasolines, PRFs deviate from this behavior to some extent. Consequently, TSFs can serve as more accurate reference fuels for estimating RON numbers within acceptable error limits of  $\pm 0.3$  ON, aligning with ASTM standards.

However, it is essential to note that the accuracy of the RON estimation heavily relies on the similarity between the knocking oscillation intensity of the sample fuel and that of the reference fuels. Empirical evidence suggests that TSFs demonstrate a more congruent oscillation behavior with commercial-grade gasoline, making them a suitable choice for this purpose.

In contrast to assertions in literature [103], utilizing a pressure oscillation system such as MAMPO<sub>20T</sub> does not inherently disturb the RON scale, although discrepancies in RON may emerge with fuels exceeding RON 100, which will be discussed in the next section.

## 5.5 MAMPO<sub>20T</sub> method for fuels exceeding RON 100

### 5.5.1 ASTM RON for fuels exceeding RON 100

Commonly employed techniques for enhancing engine efficiency encompass elevating the compression ratio, downsizing paired with turbocharging, downsizing, or employing cylinder deactivation [104]. These approaches typically elevate the pressure and temperature within the cylinder's air-fuel mixture, potentially inducing partial autoignition, which can lead to detrimental knocking combustion [104]. Because of the knock constraints observed in contemporary engines, both researchers and automotive manufacturers have

advocated for fuels featuring elevated octane ratings [105]. Consequently, certain premium gasoline variants, as well as E85, achieve octane ratings exceeding 100 [106, 107]. Traditional fuels utilized tetraethyl lead (TEL) to boost their octane ratings, yet TEL was gradually phased out from commercial gasoline usage. Its complete prohibition occurred in the 1990s, primarily due to its harmful effects on human health and the environment. However, ASTM octane ratings surpassing 100 necessitate the incorporation of diluted TEL into iso-octane for use as reference fuels [40, 41]. Numerous oxygenates, including methanol and ethanol, exhibit octane ratings exceeding 100, leading to an elevated frequency of TEL admixture into iso-octane for RON rating assessments in commercial gasoline blends.

To avoid the use of TEL, ASTM has adopted a ‘fit for use’ assessment procedure. During a fit for use examination, a TSF with the corresponding RON level is compared against bracketing primary reference fuels (PRFs) and must fall within the specified RON tolerance of Table 5.2. If the TSF fails to meet the RON tolerance criteria, adjustments can be made to the intake air temperature within a range of  $\pm 22^{\circ}\text{C}$  for RON ratings ranging from 80.2 to 100 [40]. Once the intake air temperature is adjusted, the TSF is retested to ensure compliance and must rate within a more stringent  $\pm 0.1$  RON tolerance to successfully pass the fit for use test. It is important to note that in ASTM-D2699, no intake air temperature tuning is allowed for TSFs of  $\text{RON} > 100$  or  $\text{RON} < 87.1$  [40]. For these RON levels, the untuned TSF’s RON rating needs to be within the allowable tolerance in Table 5.2. The fit for use procedure is cumbersome, to say the least, and still relies on bracketing with PRFs for fuels below RON 100. This has raised questions about whether this procedure can be adapted and the number of TSF fit for use tests can be reduced [100].

When RON 100 is exceeded, the ASTM method omits the fit for use tests, but the RON method becomes increasingly imprecise, up to  $\pm 1.7$  for RON numbers 113 and higher, as indicated in table 5.6.

In the next sections, the MAMPO<sub>20T</sub> method will be evaluated for its usefulness beyond RON 100.

## 5.5.2 Beyond RON 100 calibration

In a subsequent test run, distinct RON 100+ fuels underwent testing using the MAMPO<sub>20T</sub> method, and the findings are juxtaposed with their corresponding ASTM RON values in Table 5.7.

Table 5.6: Toluene standardization fuel list used to recalibrate the MAMPO RON method.

| TSF Blend<br>RON | Rating<br>Tolerance | TSF Blend Composition, vol % |           |           | Compression ratio for<br>MAMPO <sub>20</sub> |
|------------------|---------------------|------------------------------|-----------|-----------|--|
|                  |                     | toluene                      | isooctane | n-heptane |  |
| 99.8             | ± 0.3               | 74                           | 10        | 16        | 9.23   |
| 103.3            | ± 0.9               | 74                           | 15        | 11        | 10.06  |
| 107.6            | ± 1.4               | 74                           | 20        | 6         | 10.99  |
| 113.0            | ± 1.7               | 74                           | 26        | 0         | 12.0   |

Table 5.7: Differences between ASTM and MAMPO20 RON for RON 100+ fuels.

| Sample fuel | ASTM RON | CR for 40 kPa MAMPO <sub>20</sub> | MAMPO <sub>20T</sub> RON | Difference |
|-------------|----------|-----------------------------------|--------------------------|------------|
| Ethanol     | 108.6    | 11.33                             | 109.9                    | +1.3       |
| Methanol    | 108.7    | 10.85                             | 107.5                    | -1.2       |
| Toluene     | 120      | 12.99                             | 118.5                    | -1.5       |

The ASTM RON values were obtained from the Aachen fuel database [64]. Those assumed values are within the ranges that can be found in literature and that span RON values of 107-109 for ethanol and 106-109 for methanol [100]. It is worth noting the MON of ethanol and methanol, which amount to 89.7 and 88.6 respectively. The considerable octane sensitivity (RON-MON) of both alcohols highlights the substantial contribution of their heat of vaporization (HoV) to their knock resistance. This characteristic is reflected in the RON test, whereas the MON test nullifies this characteristic by heating the intake charge to a fixed temperature of 149°C [41]. The chart in Figure 5.2 gives a complete overview of the RON classification of all fuels used in the test and shows the same distinct linear relationship between compression ratio and octane number for PRFs and TSFs alike.

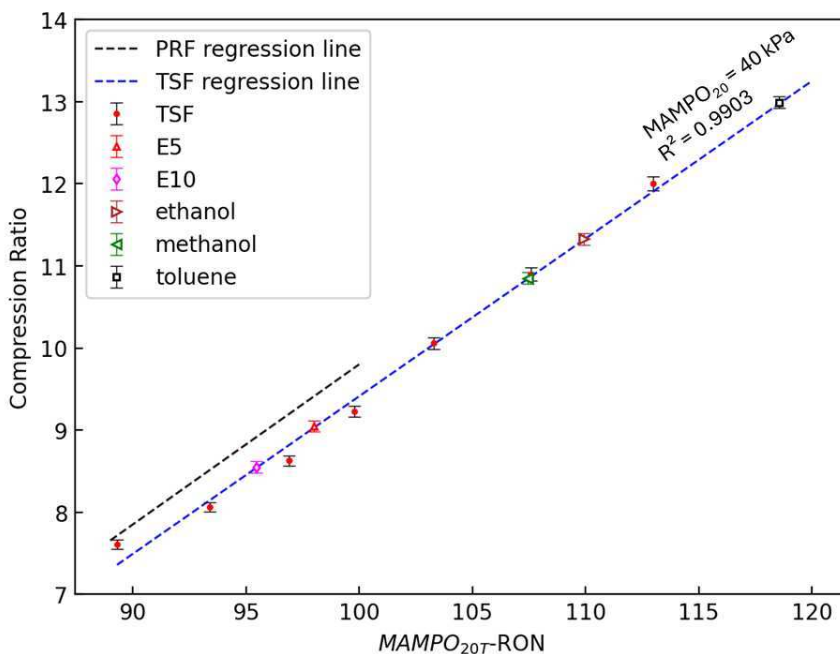


Figure 5.2: Compression ratio as a function of TSF octane number for MAMPO<sub>20T</sub> of 40 kPa.

### 5.5.3 Discussion

Upon observing Figure 5.2, it can be seen that ethanol is associated with a higher MAMPO<sub>20T</sub> RON value when compared to its respective ASTM RON, while the inverse is true for methanol and toluene. In order to explain this difference, the AMPO<sub>20</sub> distributions of different TSFs were compared to ethanol, methanol, and toluene in the box-whisker diagram of Figure 5.3. Each circular marker shows the average of the 20 highest oscillation pressure peaks per combustion cycle. A total of 500 successive combustion cycles were plotted for every fuel. The mean AMPO<sub>20</sub> value for every fuel (MAMPO<sub>20</sub>) was 40 kPa ± 5 kPa and is represented by the horizontal line in the graph, indicating that all fuels knock with comparable knock intensity. For every fuel, the needed compression ratio to obtain a MAMPO<sub>20</sub> of 40 kPa is listed on the x-axis.

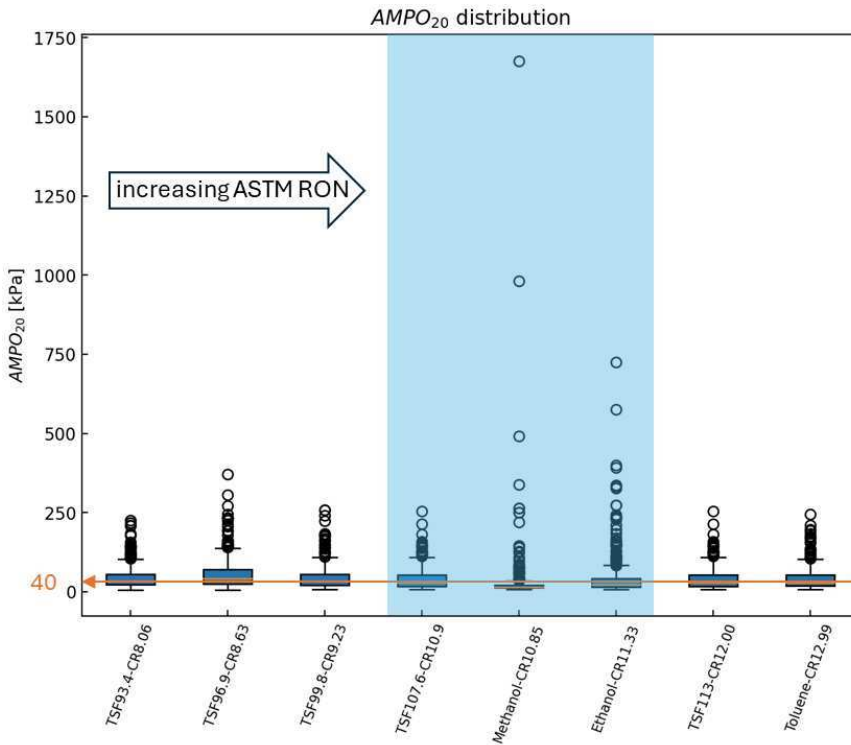


Figure 5.3: AMPO<sub>20</sub> distribution of different fuels in ascending RON order, 500 combustion cycles per fuel, knocking with MAMPO<sub>20T</sub> around 40 kPa.

Across all TSF fuels, it is evident that the oscillation behaviour remains consistent up to the TSF with RON 113. However, the divergence in oscillation behaviour between methanol, ethanol, and the TSFs is significant. In the shaded area on Figure 5.3, the oscillation behaviours of TSF 107.6, methanol, and ethanol are compared. Although they feature a comparable ASTM RON, methanol demonstrates oscillation events that are one order of magnitude higher than the primary oscillations. Ethanol exhibits comparable but notably lower oscillation intensities. Consequently, ethanol demonstrates a higher MAMPO<sub>20T</sub> RON compared to methanol, despite having an almost identical ASTM RON. The intense oscillation properties of methanol and ethanol could be subscribed to the respective high laminar flame speeds of both alcohols. Since ethanol features lower laminar flame speeds than methanol [108], one can conclude that flame speed and oscillation intensity are likely connected. This seems to be confirmed by the oscillation behaviour of toluene, shown on the right side of the graph. In comparison, toluene and TSFs in general show lower laminar flame speeds than

ethanol and methanol [108, 109], and it is observed that toluene exhibits much milder pressure oscillations, similar to all TSFs used in the test. Consequently, high laminar flame speeds may well be a possible cause of the extreme outliers in the case of methanol and ethanol. Other factors influencing the oscillation behaviour may be found in deviations in end-gas autoignition characteristics as was found in the study by Han et al. [102]. The utilization of TSFs as reference fuels ensures that the MAMPO<sub>20T</sub> scale does not disrupt the RON scale for current gasoline formulations. However, it does introduce discrepancies in the RON scale for experimental fuels exceeding RON 100. In such cases, fuels like ethanol and methanol, despite sharing the same ASTM RON, are classified differently. This disparity underscores the inadequacy of the ASTM RON test in capturing the behaviour of fuels during knock and confirms the possible added value of the MAMPO<sub>20T</sub> method as a ‘real life’ octane classification method.

### 5.5.4 MAMPO<sub>20T</sub> octane rating tolerance for fuels exceeding RON 100

Similar to the tests performed in section 5.3, the precision of the MAMPO<sub>20T</sub> method was tested TSF fuels exceeding RON 100. A test was done with TSF 107.6, having an octane tolerance of  $\pm 1.4$  with the ASTM RON test. Again, 15 tests are conducted at a consistent CR, this time with TSF107.6, yielding MAMPO<sub>20</sub> values slightly below 40 kPa. Likewise, an equal number of tests are performed at another constant CR, resulting in MAMPO<sub>20</sub> values slightly above 40 kPa. The experiment results, performed over several days by master thesis students Decuyper and De Rudder, are summarized in Table 5.8.

Table 5.8: Conducted experiments to determine MAMPO<sub>20T</sub> standard deviation with TSF 107.6

| TSF    | MAMPO at         | MAMPO at         | MAMPO at         | MAMPO at         |
|--------|------------------|------------------|------------------|------------------|
| 107.6  | CR = 10.97 (kPa) | CR = 11.05 (kPa) | CR = 10.97 (kPa) | CR = 11.05 (kPa) |
| Test 1 | 33.31            | 41.25            | Test 9           | 38.84            |
| Test 2 | 37.03            | 49.03            | Test 10          | 36.76            |
| Test 3 | 38.77            | 44.32            | Test 11          | 35.02            |
| Test 4 | 36.56            | 50.26            | Test 12          | 37.65            |
| Test 5 | 32.79            | 50.28            | Test 13          | 35.76            |
| Test 6 | 33.35            | 51.54            | Test 14          | 39.94            |
| Test 7 | 31.43            | 42.95            | Test 15          | 39.61            |
| Test 8 | 34.92            | 42.46            |                  | 41.62            |

Table 5.9: Experimental error on the MAMPO<sub>20T</sub> RON test for TSF 107.6

| <b>TSF 107.6</b>        | <b>RON</b>   | <b>CR</b>     |
|-------------------------|--------------|---------------|
| Mean value              | 107.6        | 11.01         |
| Standard deviation      | 0.110        | 0.021         |
| 95% confidence interval | 107.6 ± 0.21 | 10.99 ± 0.042 |
| 99% confidence interval | 107.6 ± 0.28 | 10.99 ± 0.055 |

For TSF 107.6, the 99% confidence interval turns out to be ± 0.28 RON. This result underlines the capability of the MAMPO<sub>20T</sub> RON method to define a fuel's octane number in a precise way and represents a potentially significant improvement to the ASTM method.

## 5.6 Chapter conclusions

The MAMPO<sub>20</sub> method exhibits a strong correlation between the ASTM RON scale and the oscillation behaviour during knock and shows a significant improvement to the historically weak correlations between AMPO and RON in the literature for PRFs and TSFs alike.

Due to the distinct differences in the oscillation behavior between PRFs and TSFs, an observable offset emerges between their respective regression lines. This discrepancy arises from variations in their response to knocking pressure oscillations. While TSFs exhibit a closer resemblance to the oscillation behavior found in real-world gasolines, PRFs deviate to some extent. Consequently, TSFs can serve as more accurate reference fuels for estimating RON numbers within acceptable error limits of ± 0.3 ON, aligning with ASTM standards.

However, it is essential to note that the accuracy of the MAMPO RON method heavily relies on the similarity between the knocking oscillation intensity of the sample fuel and that of the reference fuels. Empirical evidence suggests that TSFs demonstrate a more congruent oscillation behavior with commercial-grade gasoline, making them a suitable choice for this purpose.

In contrast to assertions in the literature [103], utilizing a pressure oscillation system such as MAMPO<sub>20T</sub> does not inherently disturb the RON scale, although discrepancies in RON may emerge with fuels exceeding RON 100.

The cumbersome fit-for-use assessment required by ASTM is no longer necessary with the MAMPO<sub>20T</sub> method.

The MAMPO<sub>20T</sub> RON method, in contrast to the ASTM method, is able to distinguish the difference in oscillation behaviour between PRFs and TSFs that share the same ASTM RON. As a result, the approach links PRF reference fuels with a MAMPO<sub>20T</sub> RON number higher than their corresponding ASTM RON. This is due to the requirement of higher compression ratios for PRFs compared to RON-equivalent TSFs to achieve the MAMPO<sub>20</sub> knock intensity of 40 kPa. The divergence in classifying PRFs on the MAMPO<sub>20T</sub> RON scale can likely be attributed to differences in lower flame speeds of PRFs, which necessitate higher compression ratios to obtain equal knock intensities compared to oxygenated fuels. The absence of this distinction in the ASTM method underscores the credibility of the MAMPO<sub>20T</sub> method as a more accurate octane quantification system reflecting real-world conditions. Fuels with molecular structures similar to those of primary reference fuels would exhibit smaller deviations from ASTM RON when the PRF-based MAMPO RON method is used.

The MAMPO<sub>20T</sub> method seems viable for assessing fuels surpassing RON 100 without complications. Notably, this method discerns between ethanol and methanol, showcasing a MAMPO<sub>20T</sub> RON difference of 2.4, whereas the ASTM RON method indicates only a 0.1 RON difference. One might question whether the ASTM RON method is capable of accurately determining the difference in RON of methanol and ethanol altogether. The ASTM method appears to be quite cumbersome and lacks precision when dealing with fuels having a RON exceeding 100, particularly when TSFs are employed as reference fuels. In contrast, the MAMPO<sub>20T</sub> method is straightforward to use and maintains its precision across the entire spectrum of octane ratings exceeding 100. This underscores how the MAMPO<sub>20T</sub> method can distinguish between two fuels with nearly identical ASTM RON values based on variations in oscillation behaviour. The inadequacy of the ASTM RON test to capture the behaviour of fuels during knock confirms the possible added value of the MAMPO<sub>20T</sub> method as a ‘real life’ octane classification method for fuels below and above RON 100.

One limitation of the MAMPO<sub>20T</sub> method arises from its inability to measure knock intensity in real time, since the MAMPO KI value needs to be calculated through post-processing, rendering it impractical for real-time applications. Due to its reliance on an averaging algorithm, the method loses detailed cylinder pressure information upon application. The systematic factors influencing high-frequency oscillation behaviour, while showing a connection to laminar flame speed, remain incompletely understood to date. Further investigation is necessary to gain deeper insights into this behaviour. The existing approach utilizes a CFR engine where the

compression ratio serves as the adjustable parameter for evaluation. Given that the MAMPO method can be implemented whenever cylinder chamber pressure can be monitored, future investigations could utilize a commercial engine with a fixed compression ratio. Other parameters such as ignition timing, boost pressure, or intake temperature could be manipulated instead, on the condition that the results are sufficiently reproducible. Implementing a version of the MAMPO method in a production engine would enable a more direct assessment of a fuel's octane behaviour within that specific engine. It would also allow a direct approach for an assessment of the engine's octane requirement (OR) [96] since the method enables a direct measurement of knock intensity, independent of the antiknock strategy of the engine's ECU that relies on measurements of the knock sensor instead. It would also provide a solution to the contention that operating conditions deviate from real-world scenarios.

In the next chapter, the connection between  $MAMPO_{20T}$  knock intensity and knock sensor output will be explored and potential correlations will be assessed. This investigation could facilitate the quantification of knock intensity using a knock sensor, potentially replacing the need for pressure transducers entirely.

# 6

## Octane quantification with a knock sensor

In this chapter, initial steps are taken towards quantifying octane levels in a manner akin to detecting knock in a production engine, i.e. utilizing a knock sensor. Traditionally employed to identify knock events, the potential of utilizing the sensor's signal output for octane quantification is explored. If successful, this approach would bring 'real life' octane quantification and knock detection closer together, since both concepts would rely on the same sensor technology.

## 6.1 The principle of knock detection

The MAMPO method relies on a cylinder pressure sensor to gauge the pressure oscillations within the combustion chamber. Within the extensive array of knock detection methods, those relying on in-cylinder pressure sensors offer the highest level of precision in detection [110]. Nevertheless, these sensors still encounter challenges related to durability and cost. In on-board applications, knock detection is often accomplished through vibration measurement with so-called knock sensors, albeit with limitations in accuracy stemming from natural vibrations and external noise interference [110]. Typically installed on the engine block, cylinder head, or intake manifold, depending on the vehicle model, most knock sensors are of the accelerometer type and comprise a piezoelectric component capable of generating a voltage when subjected to mechanical strain. This component is affixed to a resonant chamber designed to amplify the vibrations induced by engine knock. The knock sensor is connected to the Engine Control Unit (ECU).

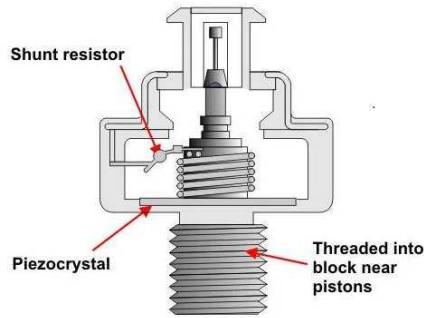


Figure 6.1: Diagram of a knock sensor.

Upon occurrence of knock, the knock sensor detects the resulting vibration, converting it into an electronic signal. This signal's magnitude and frequency correlates with the knock intensity. Subsequently, the ECU receives and analyzes this signal and upon identification of knock, the ECU adjusts the ignition timing by a few degrees, a process known as ignition timing retardation, until the knock subsides. In most cases, the knock sensor signal could be interpreted as a binary signal. If a certain vibration intensity threshold is exceeded, the ECU detects it as knock and acts upon the ignition timing.

In the following section the output signal of a knock sensor is investigated to determine whether a correlation can be found between  $MAMPO_{20}$  knock intensity, discussed in the previous chapters, and the knock sensor signal. To this end, the

CFR engine is equipped with a Bosch standard issue knock sensor (part number 0261231226), mounted directly onto the cylinder head, as depicted in Figure 6.2



*Figure 6.2: Mounting location of the knock sensor on the CFR engine.*

## **6.2 Pressure oscillations versus knock sensor signal**

The knock sensor proved to be a challenge since no information could be obtained regarding its accuracy, resolution or reproducibility specifications, necessitating

experimental accuracy verification which is discussed later in this chapter. To investigate the signal output of the knock sensor, it was connected to the CFR's data acquisition system and sampled at the same rate with which the combustion chamber pressure signal is sampled, every  $0.25^\circ\text{CA}$ . Figure 6.3 depicts the knock sensor signal output for a non-knocking combustion cycle and Figure 6.4 represents the signal from a knocking combustion cycle. Signal filtering is not applied since it proves to be unnecessary. The valve actuation was clearly visible on the knock sensor signal but the signal was sampled between inlet valve closing and exhaust valve opening.

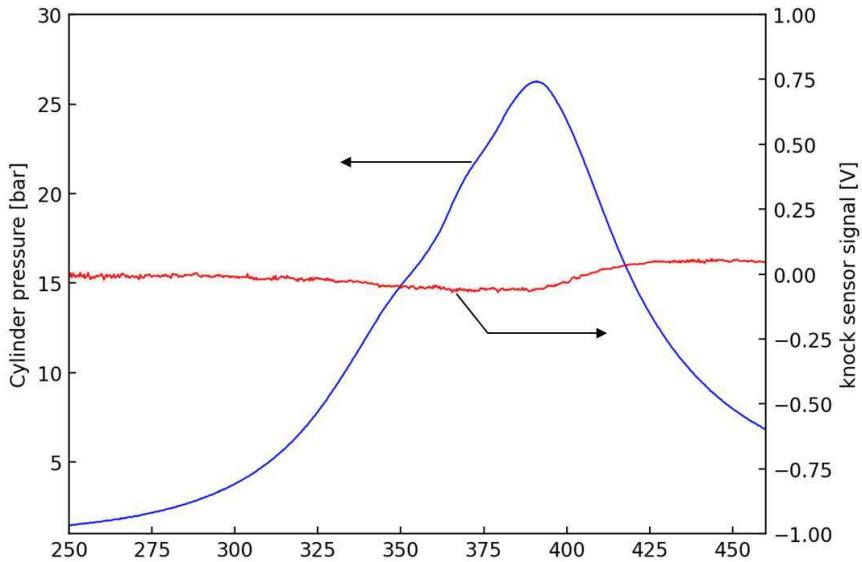


Figure 6.3: The chamber pressure signal and corresponding knock sensor output for a non-knocking combustion cycle.

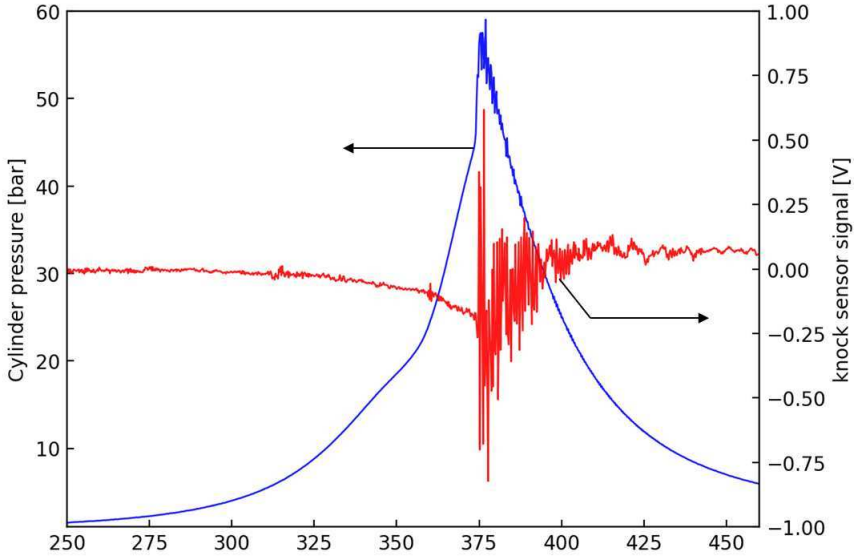


Figure 6.4: The chamber pressure signal and corresponding knock sensor output for a knocking cycle.

Upon observation of the signals of Figure 6.4, a correspondence between the knock sensor output signal and pressure oscillation is suspected, leading to a further in-depth exploration of the knock sensor signal. Since the MAMPO method processes the combustion chamber pressure data with a double averaging algorithm, the knock sensor signal is processed in a similar way and its correlation with MAMPO knock intensity is explored, as is explained in the next section.

### 6.3 Knock intensity definition based on knock sensor signal output

In order to generate knock intensity information, similar to the MAMPO principle but based on the knock signal output, knock intensity is redefined. The average knock oscillation (AKO) of  $X$  knock sensor oscillations ( $AKO_X$ ) is defined as the average of the  $X$  highest peak-to-peak amplitudes, as shown in Equation 6.1 and depicted in Figure 6.5.

$$AKO_X = \frac{1}{X} \sum_{j=1}^X \max_j - \min_j \quad (6.1)$$

Similarly to the  $MAMPO_X$  method, the average of these averages is named the mean average knock oscillations ( $MAKO_X$ ), defined by equation 6.2.

$$MAKO_X = \frac{\sum_{i=1}^N AKO_{Xi}}{N} \quad (6.2)$$

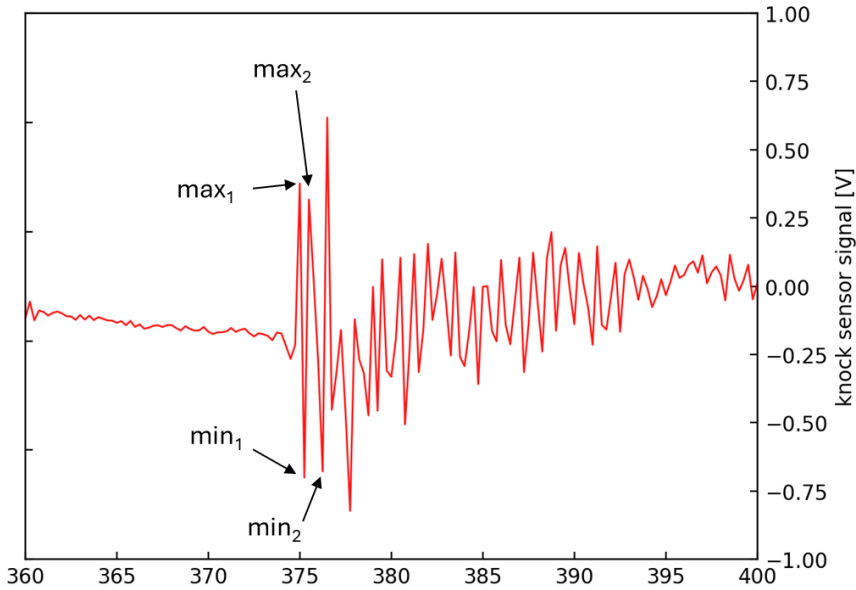


Figure 6.5: Peak-to-peak knock sensor signal oscillations.

## 6.4 Correlation between $MAMPO_{20}$ versus $MAKO_{20}$ knock intensity

To investigate whether a correlation can be found between  $MAMPO_{20}$  and  $MAKO_X$  knock intensity, the same number of oscillation peaks per cycle is initially selected. Hence,  $MAKO_{20}$ , defined by Equation 6.3 and  $MAMPO_{20}$  are measured at the same time and 20 highest and 20 lowest voltage peaks are stored and averaged over 500 successive combustion cycles, similar to the MAMPO method, with the settings of table 4.2 applied.

$$MAKO_{20} = \frac{\sum_{i=1}^{500} AKO_{20i}}{500} \quad (6.3)$$

To investigate how  $MAMPO_{20}$  and  $MAKO_{20}$  relate, different fuels were subjected to increasing  $MAMPO_{20}$  knock intensities and corresponding  $MAKO_{20}$  intensities were recorded. The fuels used were: TSF93.4, TSF96.9, PRF95 and E10. Upon observing the results in Figure 6.6, one can notice a linear relationship between  $MAKO_{20}$  and  $MAMPO_{20}$  with  $R^2$  values close to unity pointing out the good correlation between  $MAMPO_{20}$  and  $MAKO_{20}$  knock intensity.

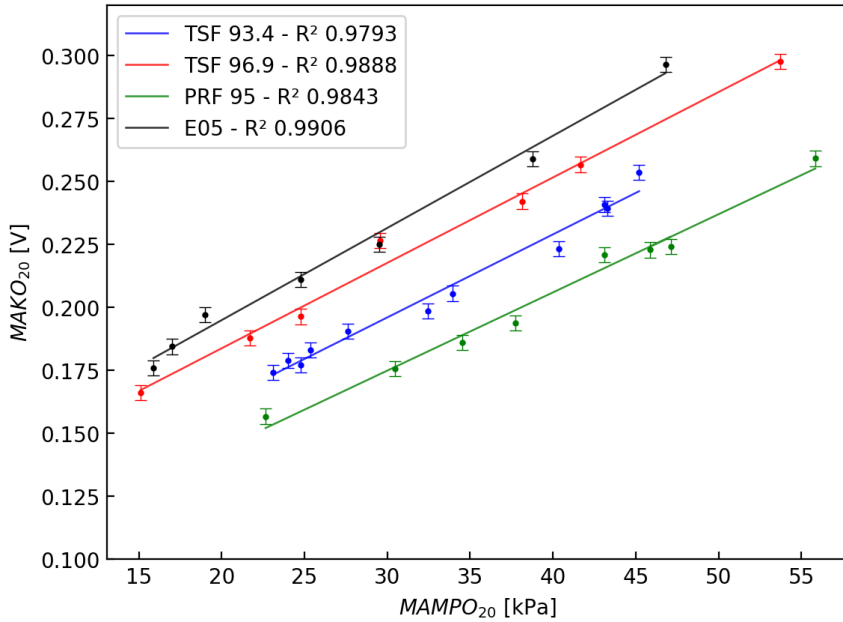


Figure 6.6:  $MAMPO_{20}$ - $MAKO_{20}$  relationship for different fuels

Notwithstanding the strong linear correlation between  $MAMPO_{20}$  and  $MAKO_{20}$ , it can be noticed that for the same  $MAMPO_{20}$ , the corresponding  $MAKO_{20}$  values are different with every fuel. When a specific fuel knocks with a given  $MAMPO_{20}$  knock intensity, the corresponding  $MAKO_{20}$  intensity will be higher with increasing RON of that fuel. This can be explained by considering the relationship between the knock sensor and the geometry of the CFR. When higher RON fuels are utilized, it becomes necessary to use higher compression ratios to obtain the same knock intensity compared to lower RON fuels. This adjustment influences the resonance frequency of the CFR, thereby resulting in a different response from the knock sensor.

The conclusion drawn from the correlation investigation in this section is evident: a constant  $MAMPO_{20}$  knock intensity does not correspond to a constant  $MAKO_{20}$

value. Furthermore, it is observed that the regression lines for TSF increase in level with higher RON numbers. E5, boasting the highest RON, also exhibits the highest line in the graph. However, the regression line for PRF 95, despite having a higher ASTM RON, is positioned below that of TSF 93.4. This observation confirms the assertion that PRFs do not exhibit behavior similar to TSFs or modern-day gasoline fuels.

## 6.5 Constant $MAMPO_{20}$ curve of 40 kPa

In a manner akin to the methodology employed in the MAMPO approach, the TRFs listed in Table 6.1 are utilized to establish a relationship between the MAKO value and the CR at a MAMPO value of 40 kPa. This process entails examining the MAKO, CR, and MAMPO values of two experiments for each TSF. Initially, the CR is configured to generate a MAMPO value slightly below 40 kPa in the first experiment, while in the subsequent experiment, the CR is adjusted to produce a MAMPO value slightly above 40 kPa. Through interpolation of these two experiments to a MAMPO of 40 kPa, the corresponding MAKO value and CR can be deduced.

Table 6.1: 40 kPa  $MAMPO_{20}$  knock intensity and corresponding  $MAKO_{20}$  value

| RON   | TSF blend composition, vol% |            |           | CR for 40kPa | corresponding |
|-------|-----------------------------|------------|-----------|--------------|---------------|
|       | Toluene                     | Iso-octane | n-Heptane | $MAMPO_{20}$ | $MAKO_{20}$   |
| 89.3  | 66%                         | 0%         | 34%       | 7,58         | 0,2423        |
| 93.4  | 74%                         | 0%         | 26%       | 8,18         | 0,2422        |
| 96.9  | 74%                         | 5%         | 21%       | 8,77         | 0,25          |
| 99.8  | 74%                         | 10%        | 16%       | 9,26         | 0,2612        |
| 103.3 | 74%                         | 15%        | 11%       | 10,07        | 0,2984        |
| 107.6 | 74%                         | 20%        | 6%        | 11,01        | 0,326         |

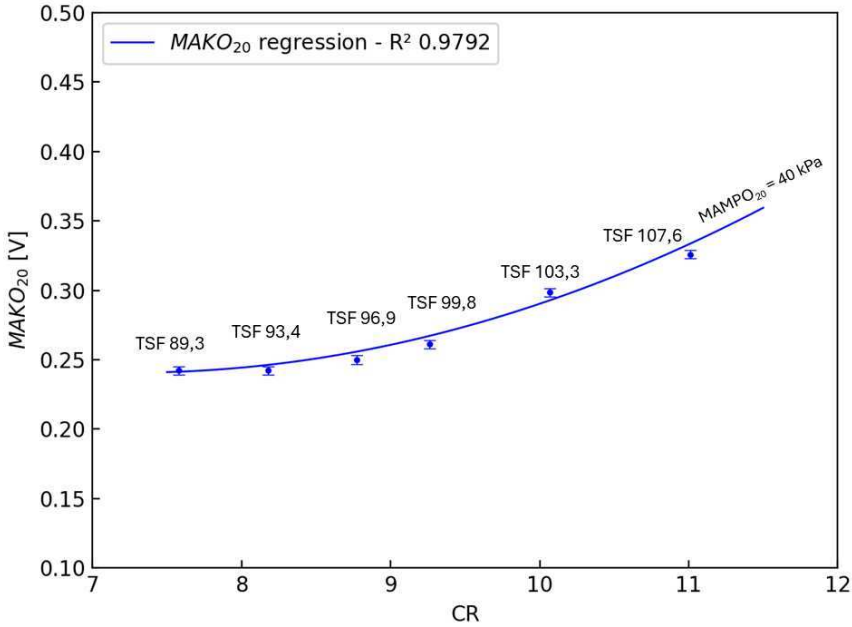


Figure 6.7: Regression curve of  $MAKO_{20}$  as a function of  $CR$ , to obtain a  $MAMPO_{20}$  knocking intensity for TSFs.

The outcome of these experiments is illustrated in Figure 6.7. It is apparent from the graph that the correlation between the  $MAKO_{20}$  value and the compression ratio ( $CR$ ) is accurately represented by a second-order polynomial. As shown in the figure, a remarkably high  $R^2$  value of 0.9792 is achieved, indicating a close fit of the second-order polynomial model to the experimental data. Equation 6.4 presents the second-order polynomial equation defining this relationship.

$$MAKO_{20} = 0.0066 \cdot CR^2 - 0.0958 \cdot CR + 0.5883 \quad (6.4)$$

This suggests that by treating  $MAKO_{20}$  as a function of compression ratio and expressing RON using the equation for  $MAMPO_{20T}$  RON (Equation 5.1), the RON value of an unknown fuel can be inferred without the need for direct pressure measurements within the combustion chamber. Following initial calibration with the  $MAMPO_{20T}$  method and achieving a  $MAMPO_{20}$  knock intensity of 40 kPa, the only sensor required would be a knock sensor installed on the engine.

It is worthwhile mentioning that the amount of peaks  $X$  in the  $MAKO_X$  method does not have a significant influence on the correlation with  $MAMPO_{20}$ . Within the

same experiment, to obtain a  $MAMPO_{20}$  of 40 kPa,  $MAKO_X$  has been calculated for the different TSFs, based on 5 up to 50 oscillation peaks. The result is depicted in Figure 6.8. For any number of oscillation peaks used, the MAKO value obviously decreases with increasing pressure peaks, but the  $R^2$  value remains high. The remainder of this work will therefore be based on  $MAKO_{20}$  calculations.

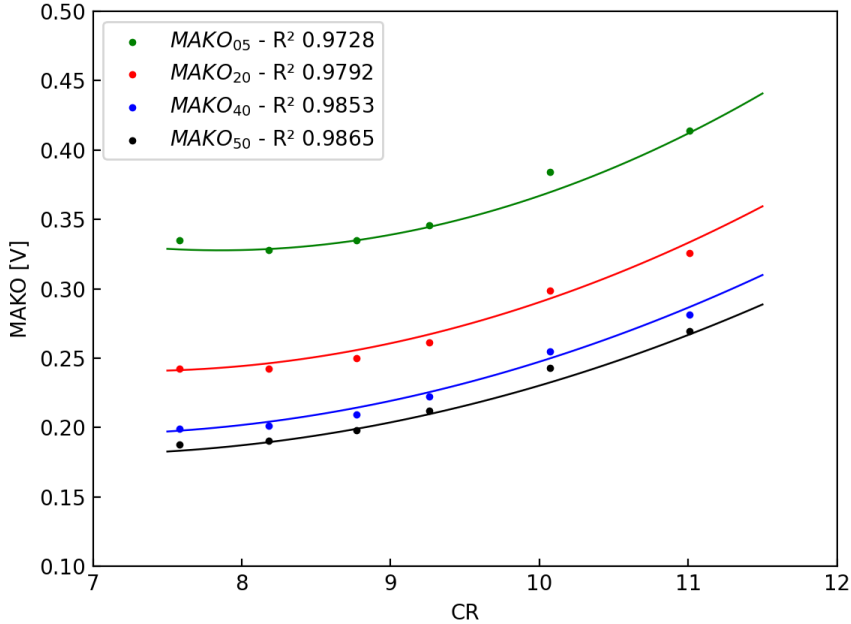


Figure 6.8: Influence of number of AKO peaks on correlation.

In the next section, the method is applied in practice to obtain the  $MAKO_{20T}$  RON of three different fuels.

## 6.6 Obtaining $MAKO_{20T}$ RON of E5, E10 and PRF95

To determine the RON value of E5, E10 and PRF95 using the  $MAKO_{20T}$  method, several experiments were conducted at different compression ratios (CR). Each experiment yielded a  $MAKO_{20}$  value along with the corresponding CR. The points in Figure 6.9 represent these experiments for E5, E10 and PRF95. Initially, experiments were conducted at the lowest CR, with subsequent increments in CR

resulting in higher  $MAKO_{20}$  values. This process continued until the  $MAKO$  value surpassed the threshold defined by the second-order polynomial of Equation 6.4. Based on these experiments, conducted by master thesis students De Rudder and Decuyper, the linear relationship between the  $MAKO_{20}$  value and CR for E5, E10 and PRF is established, resulting in the straight lines on the graph of Figure 6.9. The intersection of each of those lines with the  $MAKO_{20T}$  regression curve then allows to obtain the compression ratio at which the fuel knocks with a  $MAMPO_{20}$  KI of 40 kPa.

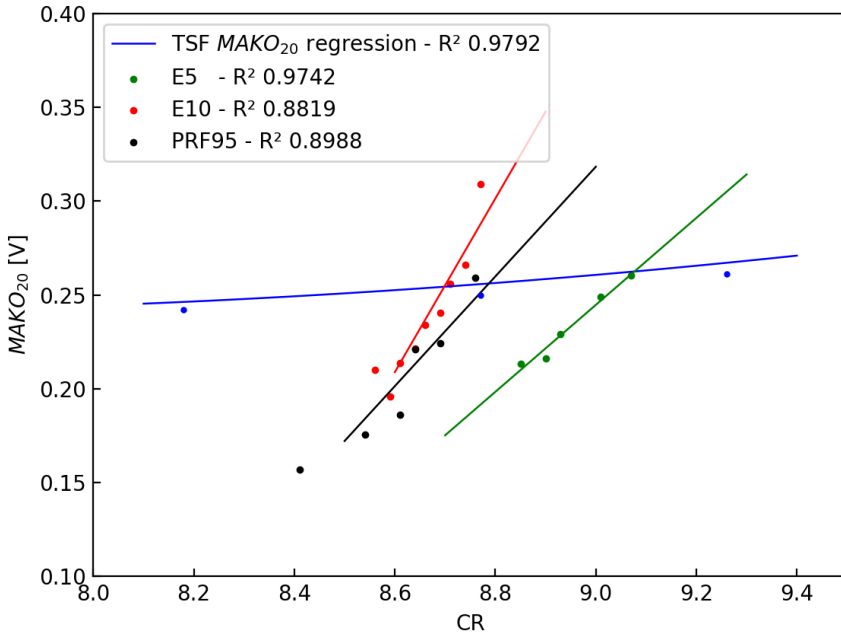


Figure 6.9: Experiments relating  $MAKO_{20}$  and CR for E5, E10 and PRF95

These lines were previously depicted in figure 6.6 and are written out in Equations 6.5, 6.6 and 6.7.

$$MAKO_{20} \text{ E5} = 0.2318 \cdot CR - 1.8415 \quad (6.5)$$

$$MAKO_{20} \text{ E10} = 0.4629 \cdot CR - 3.7721 \quad (6.6)$$

$$MAKO_{20} \text{ PRF95} = 0.2924 \cdot CR - 2.3136 \quad (6.7)$$

To clarify things, let's take E5 as an example. To find the intersection between the TSF second-order regression polynomial and the E5 regression line, as shown in Figure 6.10, a system of two independent equations is made of Equation 6.4 and Equation 6.5, leading to Expression 6.8.

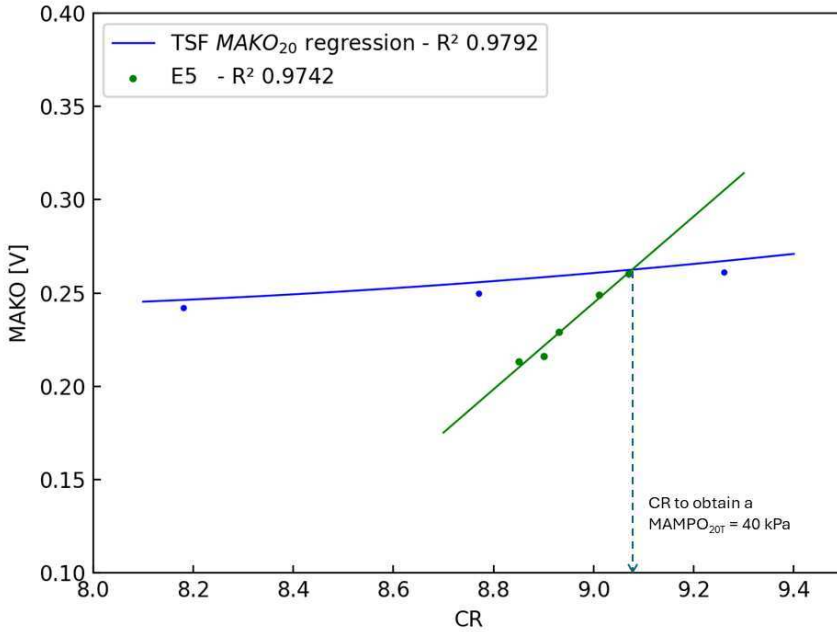


Figure 6.10: Obtaining the intersection of the TSF  $MAKO_{20}$  curve and  $MAKO_{20}$  regression line for E5

$$\begin{cases} MAKO_{20} \text{ E5} = 0.2318 \cdot CR - 1.8415 \\ MAKO_{20} \text{ TSF} = 0.0066 \cdot CR^2 - 0.0958 \cdot CR + 0.5883 \end{cases} \quad (6.8)$$

By solving this set of equations, we can determine the intersection between the derived relation and the second-order polynomial of Expression 6.8. This intersection provides a  $MAKO_{20}$  value and its corresponding CR for E5. The obtained CR can then be substituted into Equation 5.1, the equation for calculating RON based on TSFs ( $MAMPO_{20T} \text{ RON} = 51.78 + 5.12 \cdot CR$ ) to determine the corresponding RON value. For the example with E5, the calculations are detailed below.

From expression 6.8, the discriminant and the roots for the CR can be calculated.

$$0.0066 \cdot CR^2 - 0.0958 \cdot CR + 0.5883 = 0.2318 \cdot CR - 1.8415$$

$$\rightarrow 0.0066 \cdot CR^2 - 0.3276 \cdot CR + 2.4298 = 0$$

$$D = (-0.3276)^2 - 4 \cdot 0.0066 \cdot 2.4298 = 0.0432$$

$$CR_{1,2} = \frac{-(-0.3276) \pm \sqrt{D}}{2 \times 0.0066} \rightarrow \begin{cases} CR_1 = 9.08 \\ CR_2 = 40.56 \end{cases}$$

The second root, with a CR of 40.56, is evidently impossible. This value is largely above the CFR's compression ratio limit, indicating that the appropriate CR value is 9.08. With this CR established, we can proceed to compute the  $MAKO_{20}$  and subsequently determine the RON value using Equation 6.5 and Equation  $MAMPO_{20}$   $RON = 51.78 + 5.12 \cdot CR$ , respectively.

$$MAKO_{20} = 0.0066 \times 9.082 - 0.0958 \times CR + 0.5883 = 0.2625$$

$$MAKO_{20T} RON = 51.78 + 5.12 \times 9.08 = 98.2$$

In the same manner, the compression ratios at the intersection with the  $MAKO_{20T}$  polynomial can be obtained for E10 and PRF95. The obtained results of the calculations for the three fuels are presented in Table 6.2.

Table 6.2:  $MAKO_{20T}$  RON values for E5, E10 and PRF95

|          | <b>E5</b> | <b>E10</b> | <b>PRF95</b> |
|----------|-----------|------------|--------------|
| MAKO (V) | 0.2625    | 0.2537     | 0.2563       |
| CR       | 9.08      | 8.66       | 8.80         |
| RON      | 98.2      | 96.2       | 96.8         |

It can be concluded that  $MAKO_{20T}$  RON method provides a proof-of-concept that RON estimations can be made without directly using a pressure sensor. The method seems to be correct for E5 and E10, but the result with PRF95 is too far off. Again, this can be explained by the different oscillation behavior of PRFs, confirming the non-suitability of PRFs for oscillation-based RON measurements. In the next section, an error analysis is performed.

## 6.7 Error analysis

### 6.7.1 Confidence interval with E5

The unknown accuracy specifications of the knock sensor posed limitations to performing a theoretical error analysis like the one that was performed with the MAMPO method. However, similar to the  $MAMPO_{20T}$  method, experiments are conducted to determine the confidence interval for  $MAKO_{20T}$  RON results for E5. Twelve subsequent runs, spread over several days, were conducted with a CR to obtain a  $MAMPO_{20}$  lower than 40kPa, and the corresponding  $MAKO_{20}$  voltages were recorded. The values are paired with a series of corresponding runs featuring a higher CR, to obtain a  $MAMPO_{20}$  higher than 40 kPa, again with corresponding  $MAKO_{20}$  voltages. This results in a total of  $N^2 = 144$  experiments. The results are listed in Table 6.3.

Table 6.3: Interpolation tests with E5 to obtain a  $MAKO_{20}$  value that corresponds with a  $MAMPO_{20}$  of 40 kPa

| Test | MAKO<br>at CR = 9.01 (V) | MAKO<br>at CR = 9.07 (V) | Test | MAKO<br>at CR = 9.01 (V) | MAKO<br>at CR = 9.07 (V) |
|------|--------------------------|--------------------------|------|--------------------------|--------------------------|
| 1    | 0.2345                   | 0.2603                   | 7    | 0.2287                   | 0.2604                   |
| 2    | 0.2393                   | 0.2671                   | 8    | 0.2395                   | 0.2644                   |
| 3    | 0.2464                   | 0.2680                   | 9    | 0.2389                   | 0.2667                   |
| 4    | 0.2315                   | 0.2621                   | 10   | 0.2166                   | 0.2947                   |
| 5    | 0.2275                   | 0.2667                   | 11   | 0.2432                   | 0.2882                   |
| 6    | 0.2490                   | 0.2669                   | 12   | 0.2362                   | 0.2735                   |

To obtain the RON of the 144 combinations, a simple linear interpolation to obtain the CR for a  $MAMPO_{20}$  of 40 kPa, can no longer be performed. Instead, the intersection between the second-order  $MAKO_{20}$  polynomial and a straight line from the relationship in section 6.4 is now to be defined. A straight line can be obtained by performing two experiments.

The equation for a straight line with two experimental points is shown in Equation 6.9. Here  $MAKO_2$  and  $MAKO_1$  represent respectively the MAKO value at the higher and lower CR, while  $CR_2$  and  $CR_1$  represent the higher and lower CR.

$$MAKO = \frac{MAKO_2 - MAKO_1}{CR_2 - CR_1} \cdot (CR - CR_1) + MAKO_1 \quad (6.9)$$

For each combination, the intersection of this straight line with the  $MAKO_{20T}$  polynomial (defined by Equation 6.4:  $MAKO_{20} = 0.0066 \cdot CR^2 - 0.0958 \cdot CR + 0.5883$ ) can be calculated.

Each thus obtained intersection gives the CR which can be used in the  $MAMPO_{20T}$  RON equation ( $MAMPO_{20T}$  RON =  $51.78 + 5.12 \cdot CR$ ) to calculate the 144 corresponding  $MAKO_{20T}$  RON values.

Similar to the method used in Section 5.3, Equations 5.2 and 5.3 are used to calculate the mean value and the standard deviation of the 144  $MAKO_{20T}$  RON values. The results are shown in Table 6.4.

Table 6.4: Standard deviation for  $MAKO_{20T}$  RON with E5

| Parameter          | $MAKO_{20T}$ RON | CR    | MAKO    |
|--------------------|------------------|-------|---------|
| Mean value         | 98.20            | 9.059 | 0.262   |
| Standard deviation | 0.063            | 0.012 | 0.00029 |

The standard deviation calculated for  $MAKO_{20T}$  and CR does not represent the actual standard deviation on RON for the MAKO method. Since the MAKO method relies on a  $MAMPO_{20}$  value of 40 kPa to establish the relationship between MAKO and CR, the standard deviation for the MAMPO method must also be taken into account. This is achieved by using Equation 6.10.

$$\sigma_{total} = \sqrt{\sigma_{MAMPO}^2 + \sigma_{MAKO}^2} \quad (6.10)$$

With the thus obtained standard deviation, the confidence intervals can be calculated using Equations 5.4 and 5.5. The results are shown in Table 6.5.

Table 6.5: The  $MAKO_{20T}$  RON result for E5 with 95% and 99% confidence intervals

|                         | RON             | CR                | MAKO                |
|-------------------------|-----------------|-------------------|---------------------|
| Mean value              | 98.20           | 9.059             | 0.262               |
| Standard deviation      | 0.103           | 0.02              | 0.00029             |
| 95% confidence interval | $98.20 \pm 0.2$ | $9.059 \pm 0.039$ | $0.262 \pm 0.00057$ |
| 99% confidence interval | $98.20 \pm 0.3$ | $9.059 \pm 0.052$ | $0.262 \pm 0.00075$ |

With the standard deviations of MAMPO and MAKO combined, this method proves to be capable of determining the RON of a fuel within an experimental uncertainty of  $\pm 0.3$  RON, which is within ASTM standards.

## 6.7.2 Confidence interval with TSF 107.6

To verify the experimental uncertainty of fuels beyond RON 100, the same type of test runs are performed, this time with TSF 107.6.

Table 6.6: Interpolation tests with TSF 107.6 to obtain a  $MAKO_{20}$  value that corresponds with a  $MAMPO_{20}$  of 40 kPa

| Test | MAKO<br>at CR = 10.97 (V) | MAKO<br>at CR = 11.05 (V) | Test | MAKO<br>at CR = 10.97 (V) | MAKO<br>at CR = 11.05 (V) |
|------|---------------------------|---------------------------|------|---------------------------|---------------------------|
| 1    | 0.3013                    | 0.3733                    | 9    | 0.3060                    | 0.3692                    |
| 2    | 0.3015                    | 0.3498                    | 10   | 0.3032                    | 0.3620                    |
| 3    | 0.3049                    | 0.3588                    | 11   | 0.3058                    | 0.3462                    |
| 4    | 0.3246                    | 0.3439                    | 12   | 0.2889                    | 0.3665                    |
| 5    | 0.2885                    | 0.3851                    | 13   | 0.2918                    | 0.3648                    |
| 6    | 0.3071                    | 0.3975                    | 14   | 0.3153                    | 0.3628                    |
| 7    | 0.3161                    | 0.3827                    | 15   | 0.2944                    | 0.3794                    |
| 8    | 0.3018                    | 0.3881                    |      |                           |                           |

Calculating the standard deviation of the  $15^2 = 225$  intersection points with the TSF's straight lines and the polynomial leads to the result of table 6.7.

Table 6.7: Standard deviation on MAKO-derived RON for TSF 107.6

| Parameter          | MAKO <sub>20T</sub> RON | CR    | MAKO    |
|--------------------|-------------------------|-------|---------|
| Mean value         | 107.6                   | 11.01 | 0.333   |
| Standard deviation | 0.066                   | 0.013 | 0.00064 |

When the standard deviation intervals for MAKO and MAMPO are combined, we get the results from Table 6.8.

Table 6.8: Confidence interval for MAKO-based RON with TSF 107.6

|                         | RON          | CR            | MAKO            |
|-------------------------|--------------|---------------|-----------------|
| Mean value              | 107.6        | 11.01         | 0.333           |
| Standard deviation      | 0.128        | 0.025         | 0.00064         |
| 95% confidence interval | 107.6 ± 0.25 | 11.01 ± 0.048 | 0.333 ± 0.00125 |
| 99% confidence interval | 107.6 ± 0.33 | 11.01 ± 0.064 | 0.333 ± 0.00165 |

### 6.7.3 Discussion of the results

Although the specifications of the knock sensor are unknown, the results obtained with it appear to be consistent. Specifically, the MAKO-MAMPO combined confidence interval for both E5 and TSF 107.6 is approximately ±0.3 RON. This level of precision is on par with the ASTM specifications for fuels below RON 100. Notably, the result with TSF 107.6 shows significant improvement with the MAKO method compared to the ASTM method, which yields a larger confidence interval of ±1.4 with the same reference fuel [40].

## 6.8 Chapter conclusions

In this chapter, a correlation was found between the MAMPO<sub>20</sub> knock intensity and the signal of a stock knock sensor. Similar to the MAMPO<sub>20</sub> method, the peak-to-peak knock sensor signal is averaged out over twenty voltage peaks, and the average voltage over 500 combustion cycles is taken. This method is called MAKO<sub>20</sub>, representing the mean average knock sensor oscillations.

It was found that there is a strong linear correlation between  $MAMPO_{20}$  and  $MAKO_{20}$ , but this correlation is dependent on the fuel's Research Octane Number (RON). Varying compression ratios are required to obtain similar  $MAMPO_{20}$  knock intensities between different fuels, leading to a difference in knock sensor oscillation behavior.

Consequently, there is a strong correlation between compression ratio and RON when toluene standardization fuels are used as reference fuels. This correlation can be described with a second-order polynomial relationship instead of a linear one, as was the case with the MAMPO method.

Using the second-order polynomial relationship between  $MAKO_{20T}$  and compression ratio, the RON of a sample fuel can be obtained by calculating the intersection point between the polynomial with TSFs and the linear CR- $MAKO_{20}$  relationship of the sample fuel.

The method was evaluated with E5, E10, and PRF 95, providing acceptable RON results for E10 and E5, although the exact RON value of both fuels was not verified with an ASTM RON test. The result with PRF 95 fell outside of acceptable boundaries, as expected due to the mismatch in oscillation behavior between PRFs and TSFs, yielding incorrect results.

The  $MAKO_{20T}$  method underwent an error analysis based on the standard deviation of multiple test results. Combining it with the confidence interval of the MAMPO method, the uncertainty interval proves to be within the range of  $\pm 0.3$  RON, similar to ASTM specifications, for E5. Although unverified with other fuels at this point, it can be suspected that this uncertainty interval applies for all fuels with a RON below 100.

The  $MAKO_{20T}$  method excels with fuels beyond RON 100, with an unchanged  $\pm 0.3$  RON confidence interval, promising more accurate results compared to the ASTM method.

These results serve as a proof-of-concept that octane quantification can be achieved without the need for combustion chamber pressure sensors, provided that calibration with pressure sensors is conducted and the relationship with the knock sensor is established. Possibly, the employment of the MAMPO or MAKO method could provide a pathway towards improved harmonization of knock-resistant metrics in gas engines. Although this subject is not discussed in this work, it has proven to be challenging with the metrics currently in use.

It is conceivable that the MAMPO and MAKO methods, or a derivative thereof, could be employed to perform octane measurements in engines that are more

representative of production engines under different load conditions. This would enable better estimation of a fuel's performance. The knock-resistive metric obtained would thus align with real-life knock measurement situations, facilitating the more efficient development of novel sustainable fuels.



# 7

## Conclusions and outlook

## 7.1 Conclusions

This work presented a comprehensive exploration of octane quantification methods and the development of a second-generation spark ignition biofuel, Ad-Libio.

In Chapter 2, the focus was on understanding the underlying principles of spark ignition (SI) engines, which form the backbone of modern automotive propulsion. The chapter began by elucidating the four-stroke cycle, explaining each phase of intake, compression, power, and exhaust. Understanding these fundamental principles laid the groundwork for comprehending how fuels interact with the engine during combustion.

Moving on, the chapter explored the composition of gasoline, the primary fuel for SI engines. Essential properties such as octane rating, volatility, energy density, and chemical composition were dissected to elucidate their impact on engine performance. Additionally, the chapter discussed the methods used to measure these properties, comparing them to regulatory standards such as EN228 for gasoline fuels. This thorough exploration set the stage for subsequent discussions on fuel development and assessment.

Chapter 3 shifted focus to the development of Ad-Libio, a second-generation biofuel engineered for use in SI engines. Through the use of a fuel blend property calculator, predictions of the production process outcome could be made swiftly. Initial outcomes fell short of on-road suitability, prompting further modifications based on insights gleaned from a comprehensive fuel database and the blend property calculator. These modifications led to the creation of naphthenic fuel blends that show potential as gasoline replacements. The chapter culminated in the confirmation of the suitability of the most promising blend through ASTM-compliant tests for Research Octane Number (RON) and Motor Octane Number (MON), as well as Reid Vapor Pressure (RVP). The work presented in this chapter significantly contributes to the development of a promising sustainable alternative to gasoline, which could help reduce the carbon footprint of the existing gasoline fleet.

Chapter 4 introduced the MAMPO (Mean Average of Maximum Pressure Oscillations) method, a novel approach for assessing the RON of fuels. The method hinges on measuring pressure oscillations during knock events, marking a departure from traditional methods that instead rely on a type of combustion chamber pressure sensor not used in current engine technology, unable to detect oscillations in higher frequency ranges.

Historically, correlating the Research Octane Number (RON) with high-frequency

pressure oscillations during knock has proven challenging due to the stochastic nature of knock and its intensity, as measured by the Maximum Amplitude of Pressure Oscillations (MAPO) method. However, the introduction of the MAMPO<sub>20</sub> methodology addresses this randomness by providing a more consistent basis for correlation. This new approach has established a highly correlated relationship between RON and MAMPO<sub>20</sub> knock intensity, representing an important advancement in this field.

Despite the high correlation observed, discrepancies arose in the knocking oscillation behavior of Primary Reference Fuels (PRFs) compared to fuels containing compounds other than paraffinic ones. This discrepancy led to an offset in MAMPO<sub>20</sub>-derived RON values compared to ASTM RON values. The chapter concluded with the recognition of the need for a revision of the method concerning reference fuels, paving the way for further exploration in the subsequent chapters.

Chapter 5 delved deeper into the MAMPO<sub>20T</sub> method, improving the MAMPO method's effectiveness by utilizing Toluene Standardization Fuels (TSFs) as reference fuels, resulting in a demonstrated reliability with octane quantification for contemporary gasolines, with error margins in line with the traditional ASTM method. The MAMPO<sub>20T</sub> does not disrupt the established RON scale, although differences in RON emerge with fuels exceeding RON 100.

The MAMPO<sub>20T</sub> method is not only more straightforward to use than the ASTM method, but it also maintains high precision for RON 100+ fuels. Additionally, the the MAMPO<sub>20T</sub> method can distinguish between two fuels with nearly identical ASTM RON values based on variations in oscillation behaviour, a capability that the ASTM RON method lacks. The inadequacy of the ASTM RON test to capture the behaviour of fuels during knock confirms the possible added value of the MAMPO<sub>20T</sub> method as a 'real life' octane classification method for fuels below and above RON 100 and might even pave the way towards an update in the traditional octane quantification methods in use today.

In the 6th chapter, the potential applications of the MAKO method, which utilizes knock sensor signals for octane quantification, were explored. The MAKO<sub>20T</sub> method excels with fuels both below and above RON 100, maintaining an unchanged  $\pm 0.3$  RON confidence interval. This promises results that are as accurate as, or better than, those of the ASTM method. The MAKO method not only confirms the correlation between RON and oscillation behavior during knock but also provides a proof-of-concept that a knock sensor setup can be used for octane quantification, rather than solely for knock detection.

Given that the historical lack of correlation between RON and pressure oscillations during knock has been addressed by the MAMPO and MAKO methods, a new

opportunity arises for employing this knowledge in a revamped RON classification system. This system would be based on an engine setup that not only better represents modern spark-ignition (SI) engines but also utilizes the same or similar knock detection technology employed in these engines. Such an advancement would allow us to move away from the classical RON classification method, which is now almost a century old, to provide a more accurate ranking system that better suits today's engine technology.

## 7.2 Outlook

Despite the promising results obtained in this work, some aspects require further exploration. Firstly, the MAMPO method has provided new insights into the differences in pressure oscillations during knock with various fuels. While these differences may be associated with variations in laminar flame speed, the underlying science of this oscillation behavior warrants further investigation. A deeper understanding of this behavior could prove beneficial for knock prevention in future engine and fuel designs.

Additionally, it would be interesting to develop an octane quantification method based on the MAMPO or MAKO method, or a combination of both, using a modern production SI engine. Since achieving variable compression ratios is challenging with production engines, alternative strategies should be devised to induce knocking combustion in the applied fuels. By validating the method with a real-life engine, a tailored octane quantification method could be developed, enabling further steps toward updating traditional test methods.

A final reflection is reserved for the Ad-Libio fuel itself. All tests have been performed on fuels that were synthesized in the laboratory. I sincerely hope that the efforts invested in this work will lead to the mature production of a replacement for today's fossil fuels, thereby contributing to a sustainable solution for future generations.

# References

- [1] J. Morgan. *Paris COP 21: Power that speaks the truth?* Globalizations, 13(6):943–951, 2016.
- [2] M. T. McCulloch, A. Winter, C. E. Sherman, J. A. Trotter. *300 years of sclerosponge thermometry shows global warming has exceeded 1.5° C*. Nature Climate Change, pages 1–7, 2024.
- [3] C. Parmesan, M. D. Morecroft, Y. Trisurat. *Climate change 2022: Impacts, adaptation and vulnerability*. PhD thesis, GIEC, 2022.
- [4] B. Bayeh, M. Alemayehu. *Scientific community debates on causes and consequences of global warming*. Journal of Agriculture and Environmental Sciences, 4(1):1–14, 2019.
- [5] P. Friedlingstein, M. O’sullivan, M. W. Jones, R. M. Andrew, D. C. Bakker, J. Hauck, P. Landschützer, C. Le Quéré, I. T. Luijkx, G. P. Peters, et al. *Global carbon budget 2023*. Earth System Science Data, 15(12):5301–5369, 2023.
- [6] Hannah Ritchie. *Sector by sector: where do global greenhouse gas emissions come from?* <https://ourworldindata.org/ghg-emissions-by-sector>, 2020. Accessed: 2023-07-25.
- [7] European Environment Agency. *High Time to Shift Gear*. <https://www.eea.europa.eu/signals-archived/signals-2022/articles/high-time-to-shift-gear>, 2023. Accessed: 2024-2-10.
- [8] Fuels Europe. *FuelsEurope Statistics*. <https://www.fuelseurope.eu/statistics>, 2023. Accessed: 2024-3-01.
- [9] V. Viswanathan, A. H. Epstein, Y.-M. Chiang, E. Takeuchi, M. Bradley, J. Langford, M. Winter. *The challenges and opportunities of battery-powered flight*. Nature, 601(7894):519–525, 2022.

- [10] L. Zhang, T. L. Butler, B. Yang\*. *Recent trends, opportunities and challenges of sustainable aviation fuel*. Green energy to sustainability: strategies for global industries, pages 85–110, 2020.
- [11] M. Z. Jacobson. *Short-term effects of controlling fossil-fuel soot, biofuel soot and gases, and methane on climate, Arctic ice, and air pollution health*. Journal of Geophysical Research: Atmospheres, 115(D14), 2010.
- [12] W. Shi, Y. Xiao, Z. Chen, H. McLaughlin, K. X. Li. *Evolution of green shipping research: themes and methods*. Maritime Policy & Management, 45(7):863–876, 2018.
- [13] A. Joshi. *Review of vehicle engine efficiency and emissions*. SAE International Journal of Advances and Current Practices in Mobility, 2(2020-01-0352):2479–2507, 2020.
- [14] C. M. Costa, J. Barbosa, H. Castro, R. Gonçalves, S. Lanceros-Méndez. *Electric vehicles: To what extent are environmentally friendly and cost effective?—Comparative study by european countries*. Renewable and Sustainable Energy Reviews, 151:111548, 2021.
- [15] D. S. Sethu, H. K. Sheng, K. Marican. *Impact of EVs on global warming*. 2022.
- [16] N. D. S. A. Santos, V. R. Roso, A. C. T. Malaquias, J. G. C. Baeta. *Internal combustion engines and biofuels: Examining why this robust combination should not be ignored for future sustainable transportation*. Renewable and Sustainable Energy Reviews, 148:111292, 2021.
- [17] Ö. Andersson, P. Börjesson. *The greenhouse gas emissions of an electrified vehicle combined with renewable fuels: Life cycle assessment and policy implications*. Applied Energy, 289:116621, 2021.
- [18] M. Dwyer. *EIA Projects Global Conventional Vehicle Fleet will peak in 2038*. EIA projects global conventional vehicle fleet will peak in 2038.
- [19] European Commission. *The European Green Deal*. [https://ec.europa.eu/info/strategy/priorities-2019-2024/european-green-deal\\_en](https://ec.europa.eu/info/strategy/priorities-2019-2024/european-green-deal_en), 2019. Accessed: 2024-3-01.
- [20] European Commission. *Directive 2009/28/EC of the European Parliament and of the Council of 23 April 2009 on the promotion of the use of energy from renewable sources*. <https://eur-lex.europa.eu/legal-content/EN/TXT/?uri=CELEX%3A32009L0028>, 2009. Accessed: 2024-3-02.

- [21] European Commission. *Directive (EU) 2018/2001 of the European Parliament and of the Council of 11 December 2018 on the promotion of the use of energy from renewable sources*. <https://eur-lex.europa.eu/legal-content/EN/TXT/?uri=CELEX%3A32018L2001>, 2018. Accessed: 2024-3-04.
- [22] European Union. *Regulation of the European Parliament and of the council amending Regulation (EU) 2019/631 as regards strengthening the CO2 emission performance standards for new passenger cars and new light commercial vehicles in line with the Union's increased climate ambition*. 2023.
- [23] European Council. *'Fit for 55': Council adopts regulation on CO2 emissions for new cars and vans*. <https://www.consilium.europa.eu/en/press/press-releases/2023/03/28/fit-for-55-council-adopts-regulation-on-co2-emissions-for-new-cars-and-vans/>, 2023. Accessed: 2023-07-25.
- [24] European Council. *Draft regulation of the European Parliament and of the council amending Regulation (EU) 2019/631 as regards strengthening the CO2 emission performance standards for new passenger cars and new light commercial vehicles in line with the Union's increased climate ambition (first reading) - Adoption of the legislative act*. 2023.
- [25] *EN 590:2013 Automotive fuels - Diesel - Requirements and test methods*. European Committee for Standardization, 2013. EN 590:2013.
- [26] European Committee for Standardization. *EN 228: Automotive fuels - Unleaded petrol - Requirements and test methods*. European Committee for Standardization, 2012.
- [27] A. Soler. *Sustainable biomass availability in the EU towards 2050 (RED II Annex IX, Parts A and B)*. Review, page 4, 2022.
- [28] P. Leistner, K. P. Sedlbauer. *Biodiversity Impact Assessment of future biomass provision for biofuel production Phase*. Concawe Final Report, 2022.
- [29] M. T. Nazari, J. Mazutti, L. G. Basso, L. M. Colla, L. Brandli. *Biofuels and their connections with the sustainable development goals: a bibliometric and systematic review*. Environment, Development and Sustainability, 23(8):11139–11156, 2021.
- [30] Research Association for Combustion Engines. *FVV Future Fuels Study IV: Final report*. Technical report, 2021.

- [31] B. O. de Beeck, M. Dusselier, J. Geboers, J. Holsbeek, E. Morr e, S. Oswald, L. Giebeler, B. F. Sels. *Direct catalytic conversion of cellulose to liquid straight-chain alkanes*. *Energy & Environmental Science*, 8(1):230–240, 2015.
- [32] E. Staff, R. Patel, V. G. *Stages of Combustion in SI Engine in Detail*. <http://www.enggstudy.com/stages-of-combustion-in-si-engine/>, 2020. Accessed: February 1, 2024.
- [33] J. P. Szybist, S. Busch, R. L. McCormick, J. A. Pihl, D. A. Splitter, M. A. Ratcliff, C. P. Kolodziej, J. M. Storey, M. Moses-DeBusk, D. Vuilleumier, et al. *What fuel properties enable higher thermal efficiency in spark-ignited engines?* *Progress in Energy and Combustion Science*, 82:100876, 2021.
- [34] L. V. Amaral, N. D. S. A. Santos, V. R. Roso, R. d. C. de Oliveira Sebastião, F. J. P. Pujatti. *Effects of gasoline composition on engine performance, exhaust gases and operational costs*. *Renewable and Sustainable Energy Reviews*, 135:110196, 2021.
- [35] W. G. Lovell. *Knocking characteristics of hydrocarbons*. *Industrial & engineering chemistry*, 40(12):2388–2438, 1948.
- [36] M. Mulligan, W. G. Lovell, T. Boyd. *Determination of gum in gasoline*. *Industrial & Engineering Chemistry Analytical Edition*, 4(4):351–356, 1932.
- [37] R. C. Pereira, V. M. Pasa. *Effect of mono-olefins and diolefins on the stability of automotive gasoline*. *Fuel*, 85(12-13):1860–1865, 2006.
- [38] Z. Wang, H. Liu, R. D. Reitz. *Knocking combustion in spark-ignition engines*. *Progress in Energy and Combustion Science*, 61:78–112, 2017.
- [39] E. Marshall. *Early Liquid Fuels and the Controversial Octane Number Tests*. *The Piston Engine Revolution*, page 222, 2011.
- [40] ASTM International. *Standard Test Method for Research Octane Number of Spark-Ignition Engine Fuel*. <https://www.astm.org/d2699-23b.html>, 2023.
- [41] ASTM International. *Standard Test Method for Motor Octane Number of Spark-Ignition Engine Fuel*. <https://www.astm.org/d2700-23b.html>, 2023.
- [42] T. M. Foong, K. J. Morganti, M. J. Brear, G. da Silva, Y. Yang, F. L. Dryer. *The effect of charge cooling on the RON of ethanol/gasoline blends*. *SAE International Journal of Fuels and Lubricants*, 6(1):34–43, 2013.

- [43] E. Kasseris, J. Heywood. *Charge cooling effects on knock limits in SIDI engines using gasoline/ethanol blends: part 2-effective octane numbers*. SAE International Journal of Fuels and Lubricants, 5(2):844–854, 2012.
- [44] V. Mittal, J. B. Heywood. *The shift in relevance of fuel RON and MON to knock onset in modern SI engines over the last 70 years*. SAE International Journal of Engines, 2(2):1–10, 2010.
- [45] C. Pera, V. Knop. *Methodology to define gasoline surrogates dedicated to auto-ignition in engines*. Fuel, 96:59–69, 2012.
- [46] ASTM International. *Standard Test Method for Vapor Pressure of Petroleum Products (Reid Method)*. <https://www.astm.org/Standards/D323.htm>, 2019.
- [47] European Renewable Ethanol Association (ePURE). *Statistics & Infographics*. <https://www.epure.org/resources-statistics/statistics-infographics/>. Accessed: 2024-1-15.
- [48] J. Yang, P. Roth, H. Zhu, T. D. Durbin, G. Karavalakis. *Impacts of gasoline aromatic and ethanol levels on the emissions from GDI vehicles: Part 2. Influence on particulate matter, black carbon, and nanoparticle emissions*. Fuel, 252:812–820, 2019.
- [49] Z. He, W. Zhao, G. Liu, Y. Qian, X. Lu. *Effects of short chain aromatics in gasoline on GDI engine combustion and emissions*. Fuel, 297:120725, 2021.
- [50] M. K. Mohammed, H. H. Balla, Z. M. H. Al-Dulaimi, Z. S. Kareem, M. S. Al-Zuhairy. *Effect of ethanol-gasoline blends on SI engine performance and emissions*. Case Studies in Thermal Engineering, 25:100891, 2021.
- [51] G. Karavalakis, D. Short, D. Vu, R. Russell, M. Hajbabaei, A. Asa-Awuku, T. D. Durbin. *Evaluating the Effects of Aromatics Content in Gasoline on Gaseous and Particulate Matter Emissions from SI-PFI and SIDI Vehicles*. Environmental Science & Technology, 49:7021–7031, 2015.
- [52] P. Iodice, M. Cardone. *Ethanol/gasoline blends as alternative fuel in last generation spark-ignition engines: a review on CO and HC engine out emissions*. Energies, 14(13):4034, 2021.
- [53] O. I. Awad, R. Mamat, T. K. Ibrahim, A. T. Hammid, I. Yusri, M. A. Hamidi, A. M. Humada, A. Yusop. *Overview of the oxygenated fuels in spark ignition engine: Environmental and performance*. Renewable and Sustainable Energy Reviews, 91:394–408, 2018.

- [54] J. M. Bergthorson, M. J. Thomson. *A review of the combustion and emissions properties of advanced transportation biofuels and their impact on existing and future engines*. Renewable and sustainable energy reviews, 42:1393–1417, 2015.
- [55] P. Iodice, A. Amoresano, G. Langella. *A review on the effects of ethanol/gasoline fuel blends on NOX emissions in spark-ignition engines*. Biofuel Research Journal, 8(4):1465–1480, 2021.
- [56] C. Wang, S. Zeraati-Rezaei, L. Xiang, H. Xu. *Ethanol blends in spark ignition engines: RON, octane-added value, cooling effect, compression ratio, and potential engine efficiency gain*. Applied energy, 191:603–619, 2017.
- [57] M. Mourad, K. Mahmoud. *Investigation into SI engine performance characteristics and emissions fuelled with ethanol/butanol-gasoline blends*. Renewable Energy, 143:762–771, 2019.
- [58] P. Sakthivel, K. Subramanian, R. Mathai. *Experimental study on unregulated emission characteristics of a two-wheeler with ethanol-gasoline blends (E0 to E50)*. Fuel, 262:116504, 2020.
- [59] S. K. Hoekman, A. Broch, C. Robbins, E. Cenicerros, M. Natarajan. *Review of biodiesel composition, properties, and specifications*. Renewable and sustainable energy reviews, 16(1):143–169, 2012.
- [60] P. B. Thompson. *The agricultural ethics of biofuels: the food vs. fuel debate*. Agriculture, 2(4):339–358, 2012.
- [61] D. Pimentel. *Biomass utilization, limits of*. Encyclopedia of physical science and technology, 2:159–171, 2001.
- [62] A. Mohr, S. Raman. *Lessons from first generation biofuels and implications for the sustainability appraisal of second generation biofuels*. Energy policy, 63:114–122, 2013.
- [63] I. Vinke. *Development of a Fuel Mixture Properties Calculator with Preparation for Web-Based Implementation*. MRes Summer Project, Bath University, 2020.
- [64] F. vom Lehn, L. Cai, R. Tripathi, R. Broda, H. Pitsch. *A property database of fuel compounds with emphasis on spark-ignition engine applications*. Applications in Energy and Combustion Science, 5:100018, 2021.
- [65] H. Jørgensen, J. B. Kristensen, C. Felby. *Enzymatic conversion of lignocellulose into fermentable sugars: challenges and opportunities*. Biofuels, Bioproducts and Biorefining, 1(2):119–134, 2007.

- [66] F. vom Lehn. *Fuel Database, Fuel Property Modeling, and Fuel Selection*. RWTH Aachen University, 2021. <https://www.itv.rwth-aachen.de/en/research/ongoing-research/sustainable-energy-carriers/fuel-database/>.
- [67] A. T. Hoang, S. Nižetić, A. T. Le, V. G. Bui, et al. *Combustion and emission characteristics of spark and compression ignition engine fueled with 2, 5-dimethylfuran (DMF): A comprehensive review*. *Fuel*, 288:119757, 2021.
- [68] F. Hoppe, U. Burke, M. Thewes, A. Heufer, F. Kremer, S. Pischinger. *Tailor-Made Fuels from Biomass: Potentials of 2-butanone and 2-methylfuran in direct injection spark ignition engines*. *Fuel*, 167:106–117, 2016.
- [69] S. Çelebi, C. Haşımoğlu, A. Uyumaz, S. Halis, A. Calam, H. Solmaz, E. Yılmaz. *Operating range, combustion, performance and emissions of an HCCI engine fueled with naphtha*. *Fuel*, 283:118828, 2021.
- [70] A. Landera, N. Mac Dowell, A. George. *Development of robust models for the prediction of Reid vapor pressure (RVP) in fuel blends and their application to oxygenated biofuels using the SAFT- $\gamma$  approach*. *Fuel*, 283:118624, 2021.
- [71] V. F. Andersen, J. Anderson, T. Wallington, S. Mueller, O. Nielsen. *Vapor pressures of alcohol- gasoline blends*. *Energy & Fuels*, 24(6):3647–3654, 2010.
- [72] D. S. Rosangela. *Effect of additives on the antiknock properties and Reid vapor pressure of gasoline*. *Fuel*, 84:951–959, 2005.
- [73] E. Christensen, J. Yanowitz, M. Ratcliff, R. L. McCormick. *Renewable oxygenate blending effects on gasoline properties*. *Energy & Fuels*, 25(10):4723–4733, 2011.
- [74] Z. Mužíková, M. Pospíšil, G. Šebor. *Volatility and phase stability of petrol blends with ethanol*. *Fuel*, 88(8):1351–1356, 2009.
- [75] S. Velasco, F. Román, J. White. *On the Clausius–Clapeyron vapor pressure equation*. *Journal of Chemical Education*, 86(1):106, 2009.
- [76] R. L. Furey. *Volatility characteristics of gasoline-alcohol and gasoline-ether fuel blends*. *SAE transactions*, pages 777–788, 1985.
- [77] ASTM International. *Standard Test Method for Vapor Pressure of Petroleum Products (Reid Method)*. <https://www.astm.org/Standards/D323.htm>, 2020.

- [78] A. Swarts, A. Yates, Viljoen, Carl, R. Coetzer. *A further study of inconsistencies between autoignition and knock intensity in the cfr octane rating engine*. SAE transactions, pages 702–720, 2005.
- [79] EngineBuzz. *Detonation Pickup Basics*. <https://enginebuzz.com/2019/12/05/detonation-pickup-basics/>, 2019. Accessed: April 1, 2024.
- [80] K. Huber, J. Hauber, A. Raba, R. Nell. *New Test Procedure to Determine Fuel's Knock Resistance*. MTZ worldwide, 74(7):62–69, 2013.
- [81] Waukesh. *Waukesh Gas Engines: CFR F1/F2 XCP Digital Octane Panel, and Octane Analyzer Operation, Maintenance Parts Catalog*, 2 edition, 2011. Form 947-2.
- [82] CFR Engines. *XCP Technology*. <https://cfrengines.com/xcp-technology/>, 2024.
- [83] V. Arrigoni, G. Cornetti, G. Spallanzani, F. Calvi, A. Tontodonati. *High speed knock in SI engines*. Technical report, SAE Technical Paper, 1974.
- [84] A. Hoth, C. P. Kolodziej. *Effects of knock intensity measurement technique and fuel chemical composition on the research octane number (RON) of FACE gasolines: Part 1–Lambda and knock characterization*. Fuel, 304:120722, 2021.
- [85] A. D. Yates, A. Swarts, C. L. Viljoen. *Correlating auto-ignition delays and knock-limited spark-advance data for different types of fuel*. SAE transactions, pages 735–747, 2005.
- [86] A. J. Shahlari, J. B. Ghandhi. *A comparison of engine knock metrics*. Technical report, SAE Technical Paper, 2012.
- [87] M. F. Brunt, C. R. Pond, J. Biundo. *Gasoline engine knock analysis using cylinder pressure data*. SAE transactions, pages 1399–1412, 1998.
- [88] T. Rockstroh, C. P. Kolodziej, S. S. Goldsborough, T. Wallner, M. C. Jespersen. *Insights into Engine Knock*. SAE International Journal of Fuels and Lubricants, 11(4):545–562, 2018.
- [89] A. Hoth, C. P. Kolodziej. *Effects of knock intensity measurement technique and fuel chemical composition on the research octane number (RON) of FACE gasolines: Part 2–Effects of spark timing*. Fuel, 342:127694, 2023.
- [90] A. Swarts, V. Kalaskar. *Bridging the Knock Severity Gap to CFR Octane Rating Engines*. SAE International Journal of Advances and Current Practices in Mobility, 3(2020-01-2050):240–249, 2020.

- [91] K. M. Chun, J. B. Heywood. *Characterization of knock in a spark-ignition engine*. Technical report, SAE technical paper, 1989.
- [92] G. Konig, C. Sheppard. *End gas autoignition and knock in a spark ignition engine*. SAE transactions, pages 820–839, 1990.
- [93] K. Kim, M. Szedlmayer, K. Kruger, C. Kweon. *Optimization of in-cylinder pressure filter for engine research (No. ARL-TR-8034)*. US Army Research Laboratory Aberdeen Proving Ground United States, 2017.
- [94] J. Van Biesen, J. Demeersseman. *Evaluation of a new second-generation biofuel for drop-in fuel blends serving SI engine applications*. UGent Master thesis, 2022.
- [95] W. R. Leppard. *The chemical origin of fuel octane sensitivity. 1990*. SAE Paper, 902137.
- [96] G. T. Kalghatgi. *Fuel anti-knock quality-Part II. Vehicle Studies-how relevant is Motor Octane Number (MON) in modern engines?* SAE Transactions, pages 2005–2015, 2001.
- [97] N. Morgan, A. Smallbone, A. Bhave, M. Kraft, R. Cracknell, G. Kalghatgi. *Mapping surrogate gasoline compositions into RON/MON space*. Combustion and Flame, 157(6):1122–1131, 2010.
- [98] D. Kim, C. K. Westbrook, A. Violi. *Two-stage ignition behavior and octane sensitivity of toluene reference fuels as gasoline surrogate*. Combustion and Flame, 210:100–113, 2019.
- [99] G. Kalghatgi, R. Head, J. Chang, Y. Viollet, H. Babiker, A. Amer. *An alternative method based on toluene/n-heptane surrogate fuels for rating the anti-knock quality of practical gasolines*. SAE International Journal of Fuels and Lubricants, 7(3):663–672, 2014.
- [100] A. Hoth, R. Manchiraju, C. Andretti, R. Sinur, C. P. Kolodziej. *Towards Developing an Unleaded High Octane Test Procedure (RON<sub>i</sub> 100) Using Toluene Standardization Fuels (TSF)*. SAE International Journal of Advances and Current Practices in Mobility, 3(2020-01-2040):197–207, 2020.
- [101] ASTM International. *Standard Test Method for Research Octane Number of Spark-Ignition Engine Fuel*. Technical report, ASTM International, West Conshohocken, PA, USA, 2015. Accessed on 10 January 2024.
- [102] D. Han, D. Lyu, Z. Sun, X. Liang, Z. Huang. *On knocking combustion development of oxygenated gasoline fuels in a cooperative fuel research engine*. International Journal of Engine Research, 24(6):2410–2421, 2023.

- [103] G. T. Kalghatgi. *Fuel anti-knock quality-Part I. Engine studies*. SAE Transactions, pages 1993–2004, 2001.
- [104] J. B. Heywood. *Internal Combustion Engine Fundamentals*. McGraw-Hill, New York, 1998.
- [105] K. G. Duleep. *The Benefits of Increasing Fuel Octane Number on Gasoline Engine Efficiency: A Literature Review*. SAE International, 2017.
- [106] ARAL. *Aral Ultimate 102*. <https://www.aral.de/de/global/retail/kraftstoffe-und-preise/unsere-kraftstoffe/kraftstoffuebersicht/ultimate/aral-ultimate-102.html>, 2020. Accessed 4/23/2020.
- [107] Shell. *Shell Clearflex E85*. <https://www.shell.us/motorist/shell-fuels/new-shell-clearflex-e85.html>. Accessed 6/20/2020.
- [108] L. Sileghem, V. Alekseev, J. Vancoillie, E. Nilsson, S. Verhelst, A. Konnov. *Laminar burning velocities of primary reference fuels and simple alcohols*. *Fuel*, 115:32–40, 2014.
- [109] L. Sileghem, V. Alekseev, J. Vancoillie, K. Van Geem, E. J. Nilsson, S. Verhelst, A. Konnov. *Laminar burning velocity of gasoline and the gasoline surrogate components iso-octane, n-heptane and toluene*. *Fuel*, 112:355–365, 2013.
- [110] B. Pla, P. Bares, I. Jimenez, C. Guardiola. *Increasing knock detection sensitivity by combining knock sensor signal with a control oriented combustion model*. *Mechanical Systems and Signal Processing*, 168:108665, 2022.





Rendered image of a V8 spark ignition engine, operating on sustainable fuel.